



HAL
open science

Laser amplification via stimulated Brillouin scattering in the strongly coupled regime : towards control and optimization

Marco Chiaramello

► **To cite this version:**

Marco Chiaramello. Laser amplification via stimulated Brillouin scattering in the strongly coupled regime : towards control and optimization. Physics [physics]. Université Pierre et Marie Curie - Paris VI, 2016. English. NNT : 2016PA066304 . tel-01467094

HAL Id: tel-01467094

<https://theses.hal.science/tel-01467094>

Submitted on 10 Jul 2017

HAL is a multi-disciplinary open access archive for the deposit and dissemination of scientific research documents, whether they are published or not. The documents may come from teaching and research institutions in France or abroad, or from public or private research centers.

L'archive ouverte pluridisciplinaire **HAL**, est destinée au dépôt et à la diffusion de documents scientifiques de niveau recherche, publiés ou non, émanant des établissements d'enseignement et de recherche français ou étrangers, des laboratoires publics ou privés.

THÈSE DE DOCTORAT
DE L'UNIVERSITÉ PIERRE ET MARIE CURIE

Spécialité : Physique

par

Marco CHIARAMELLO

pour obtenir le grade de :

DOCTEUR DE L'UNIVERSITÉ PIERRE ET MARIE CURIE

Laser Amplification via Stimulated Brillouin Scattering
in the Strongly Coupled Regime:
Towards Control and Optimization

devant le jury composé de :

M. Benisti, D.	Rapporteur
M. Jaroszynski, D.	Rapporteur
M. Lehmann, G.	
Mme Riconda, C.	Directeur de thèse
M. Savoini, P.	
M. Tikhonchuk, V.	

A mamma

Abstract

The generation of short and high intensity laser pulses has become important in many technical applications such as in alternative schemes for laser-driven nuclear fusion or high energy particles and radiation sources generation. The energetic, intense and short pulses are difficult to generate due to the damage threshold of solid optics materials. One way to overcome these present day limitations is to use a plasma as an amplifying medium. In a plasma, a long pump and short seed pulses can be coupled in order to amplify the short pulse. The energy of the pump pulse can be delivered to the seed pulse thanks to the third participating wave, an electron plasma wave [Stimulated Raman Scattering, SRS] or an ion-acoustic wave [Stimulated Brillouin Scattering, SBS]. The SRS mechanism is characterized by a relatively fast plasma wave response allowing the shortest output pulses (\approx fs), but it needs a fine tuning between the laser frequency ω_0 and the electron wave frequency ω_e , it is affected by kinetics effects and needs a long and homogeneous plasma to be effective. The Brillouin amplification mechanism in the weak coupling regime is limited to longer output pulses (\approx ps) than SRS. However, in the strong coupling regime, it can amplify sub-ps pulses at higher intensities and has numerous advantages: the energy transfer between the pump and seed pulses is relatively fast, allowing short interaction lengths. It is robust with respect to frequency-mismatch and plasma inhomogeneities and it can operate at higher densities (above 25% of critical density), allowing larger growth rates and no parasitic thermal backscattering in the SRS frequency range.

In the present work we describe we describe analytically and theoretically the different stages of the sc-SBS amplification of the seed, with the objective of improving the coupling and the efficiency of the energy transfer. A detailed analysis of the phases time evolution of the participating waves allows one to clarify several issues in plasma amplification: the energy transfer directionality and the role of the frequency chirp originating from the laser pulse and the plasma density profile. We identify the different time-dependant phase relations that describe the evolution of the amplification at the beginning of the coupling, during the so-called exponential regime of amplification and when the pump depletion sets-in. The phases analysis allows also the estimation

of optimal values of the chirp parameter α to be imposed to the long chirped-pulse-generated pump in order to optimize the coupling, taking into account the natural frequency spread driven by the amplification process and the one associated with the plasma density profile. We show that the seed amplification can be slightly improved (reduced) if the chirp parameter is negative (positive) and small. Large values of α affect in a negative way the amplification reducing sensibly the energy transfer, no matter the sign of α . The phases analysis in presence of an inhomogeneous plasma density profile demonstrates that, contrary to SRS-based amplification, sc-SBS requires a preferential gradient of the plasma profile with respect to the seed propagation. Stimulated Brillouin Backscattering amplification is also investigated with an extensive analysis of one-dimensional particle-in-cell simulations. Parameters relevant to nowadays experimental conditions are investigated. The obtained seed pulse spectra are analyzed as a function of the interaction conditions such as plasma profile, pulses delay, and seed pulse duration. The factors affecting the amount of energy transferred are determined, and the competition between Brillouin-based amplification and parasitic Raman backscattering is analyzed, leading to the optimization of the interaction conditions. The comparison of these results with recent experiments on sc-SBS amplification validates the first experimental observation of the signatures of the transition from linear to self-similar regime. The comparison among the spectra from experiments and PIC simulations shows that the triggering of SBS is responsible for the amplification, strongly limiting the growth of SRS. A presentation of the new particle in cell code SMILEI (together with the results of very large two dimensional simulation of sc-SBS amplification), concludes this work.

Contents

1	Introduction and basic notions of laser-plasma interactions	8
1.1	Laser Plasma Interaction	10
1.2	The Propagation of Light in a Plasma	10
1.3	Plasma waves	11
1.3.1	Electron plasma waves	11
1.3.2	Ion acoustic waves	12
1.4	Stimulated Brillouin and Raman scattering	12
1.4.1	Stimulated Brillouin Backscattering	13
1.4.2	Stimulated Raman Backscattering	21
2	Energy flow directionality and time scale characterization in the strong coupling regime for SBS	23
2.1	Weak coupling regime	24
2.2	Strong coupling regime	26
2.3	Different phases of the amplification in the strong-coupling limit	26
2.3.1	Initial seed growth	30
2.3.2	Exponential growth - 'Linear' phase	35
2.3.3	Pump depletion and growth saturation	36
2.4	Conclusions	38
3	Intrinsic frequency chirp in the strong coupling regime for SBS	40
3.1	Effect of the chirp on the coupling	41
3.2	Influence of the plasma density shape and laser intensity profile on the phase evolution	50
3.2.1	Phase evolution for the propagation of pump and seed lasers without coupling	50
3.2.2	The role of a plasma density shape on the phase evolution	52
3.2.3	Density profile with $n_0(\hat{x} = 0) \neq 0$	54
3.2.4	Density profile with $n_0(\hat{x} = 0) = 0$	56

3.2.5	Intrinsic frequency chirp due to a inhomogeneous plasma density profile	57
3.2.6	Influence of realistic plasma density profile and laser shape on the SBS amplification	64
3.3	Conclusions	71
4	Parametric studies of sc-SBS optimal coupling via one-dimensional PIC simulations	73
4.1	Simulations set-up	74
4.2	Shape of the density profile	74
4.3	Relative delay between the pump and seed laser pulses	80
4.4	Initial seed duration	85
4.5	Energy transfer and final duration of the seed	92
4.6	Conclusions	97
5	Recent experiments on strong coupling SBS amplification and comparison with one dimensional PIC simulations	98
5.1	Experiments and simulations comparison	99
5.1.1	Comparison between spectra of the amplified seed from simulations and experiments	100
5.1.2	Influence of amplification on SRS spectra	103
5.2	Conclusions	110
6	Presentation of the new particle in code SMILEI and results of two dimensional simulations of sc-SBS amplification	112
6.1	The Particle-In-Cell (PIC) method for collisionless plasmas	113
6.1.1	The PIC loop	116
6.2	Two dimensional simulation of sc-SBS amplification of a short laser pulse	120
6.2.1	Simulations set-up	122
6.2.2	Amplification results	122
6.3	Conclusions	123
	Conclusions	128
	Communications related to this thesis	131
	Appendices	133
A	Relation between the chirp parameter α and the duration of a gaussian laser beam	134

B SMILEI's performance and capabilities	138
Bibliography	155

Chapter 1

Introduction and basic notions of laser-plasma interactions

In the last decades the development of high power lasers has become important as it allows to explore new fields of physics, such as nonlinear ionization processes in strong electric fields [1][2][3], the research on inertial confinement fusion [5] or building new light sources such as X-ray lasers [6]. Since the laser invention [4], in the late 1960s, the invention of Q- switching [7] and mode-locking [8] allowed to concentrate the energy into shorter and shorter pulses. Before the invention of the chirped pulse amplification in (CPA) 1985, the averaged pulse duration was limited to hundreds of picoseconds due to the severe damage to the optical components. The revolution of the CPA made possible to develop femtosecond lasers with average intensities of few petawatt [9] [10]. With the CPA, the lasers pulses are stretched by adding a linear chirp thus increasing the duration to several hundred ps: the resulting low intensity pulses are amplified and then recompressed removing the chirp to very short pulses and intensities of the order of tens of PWs. Numerous applications are waiting for laser pulses much more powerful than those available today. The efforts to surpass the nowadays intensity barriers with current laser technology face again serious problems of damage of optical components damage and costs. For example, if we want to compress 100 kJ in a 100 fs laser pulse to reach a peak intensity of 1 EW, with the actual damage thresholds of metallic grating we would need gratings with a very large surface of the order of $\approx 10m^2$, making the size and cost of infrastructures difficult to be managed. It has therefore been proposed to use plasmas as amplifying medium where the damage threshold is much higher. The plasma-based amplification and compression scheme is due to a three-wave coupling [24][25] between a short seed pulse, a longer pump pulse delivering the energy and a plasma wave: the laser pulses are crossing in a plasma chosen in an appropriate way, as it will be discussed later. The plasma wave can an electron plasma wave (Stimulated

Raman Scattering, SRS) or an ion-acoustic wave (Stimulated Brillouin Scattering). The SRS mechanism [13],[14]-[23] requires a fine tuning between the laser frequency ω_0 and the electron wave frequency ω_e . It is also affected by kinetics effects and needs a long and homogeneous plasma to be effective. The Brillouin amplification mechanism in the weak coupling regime is limited to longer output pulses (\approx ps) than SRS. However, in the strong coupling regime (sc-SBS), it can amplify sub-ps pulses at higher intensities and has numerous advantages: the energy transfer between the pump and seed pulses is relatively fast, allowing short interaction lengths. As it will be discussed later, the sc-SBS coupling is enhanced when the interactions happens in inhomogeneous plasma: this made the SBS amplification possibly easier to be controlled in plasmas generated in gas jet [34][35][36]. In addition, sc-SBS does not require any frequency mismatch between the pump and seed. The sc-SBS amplification happens in three main stages: a first interaction of the pump and seed pulses that allows the phases of the pump, seed and density perturbation to adapt in order to start the energy transfer. A second stage where pump depletion can be neglected, known as "linear regime" [24][25][29], during which the seed stretches and it is exponentially amplified. A last stage (the self-similar regime) in which the pump energy is depleted and the seed is compressed [27]. The advantages of plasma based amplifiers are apparent. There is no need for stretching and recompression apart from the laser system delivering the input laser pulses. The pulse shortening mechanism allows rather long input pulses, which are easier to generate. Fig.(1.1) schematically shows these three phases of the seed amplification.

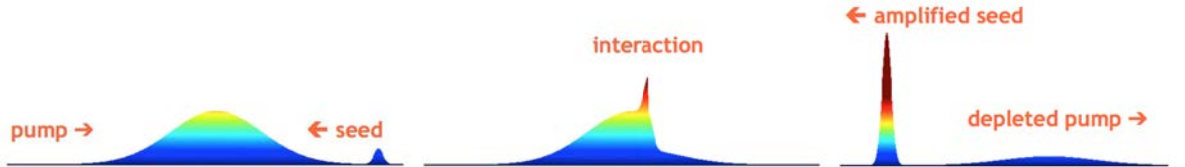


Figure 1.1: Different stages of the seed amplification schematically reproduced.

The goal of this work is to optimize the seed amplification studying the evolution of the coupling along its different stages. The effects of different parameters on laser-plasma coupling will be investigated. In the following of this chapter, we present a short review of laser-plasma physics concepts which are relevant for the understanding of the interaction regime that will be investigated in this work.

In chapter 2 we make a description of the amplification stages in terms of phase temporal evolution. We will show that the time-dependence of the total phase of the three implicated waves explains the energy flow direction during the amplification process

and determines the quality of the amplification.

In chapter 3 we present the effect on the coupling of the presence of frequency chirped pump. The analysis is carried out taking into account the natural frequency spread driven by the amplification process and the one associated with the plasma density profile.

In chapter 4 we investigate the Stimulated Brillouin Scattering amplification with an extensive analysis of one-dimensional PIC simulation that takes into account the parameters relevant to nowadays experiments.

In chapter 5 we make a comparison direct between results from PIC simulations and results from recent experiments on sc-SBS. The simulations help to elucidate and understand the regime explored in the experiments.

In chapter 6 we present the structure of the SMILEI code used to carry out the PIC simulations results showed in this work. We also include the results of two dimensional simulations on sc-SBS amplification.

Finally, in the Conclusions, the different aspects of sc-SBS laser amplification will be resumed and the efficiency of this scheme and its possible applications will be discussed.

1.1 Laser Plasma Interaction

1.2 The Propagation of Light in a Plasma

The electrons quivering in a plasma represent accelerated charges and hence radiate at the laser frequency that is shifted in phase with respect to the laser radiation field. This leads to the dispersion relation of electromagnetic waves of frequency ω and wave number k in a plasma:

$$\omega^2(k) = \omega_{pe}^2 + c^2 k^2 \quad (1.1)$$

where $\omega_{pe} = \sqrt{n_{0e} e^2 / (\epsilon_0 m_e)}$ is the electron plasma frequency. The dispersion relation implies that an electromagnetic wave with a frequency lower than ω_{pe} cannot propagate in a plasma but is reflected at the surface. Seen from a different point of view, a wave of frequency ω_0 can only propagate if the electron density is smaller than the so called critical density

$$n_c = \frac{\epsilon_0 m_e \omega_0^2}{e^2} \quad (1.2)$$

Plasmas with a lower density are called underdense. Since many plasma effects scale with the laser frequency, it is often useful to give the electron density as a fraction of the critical density.

1.3 Plasma waves

In the simplest description of a plasma, collision between the particles are neglected. Instead, the particles interact only via averaged electrostatic fields caused by charge inhomogeneities and the magnetic fields generated by plasma currents. In absence of any imposed large magnetic fields a plasma can support two kind of electrostatic waves, one at high frequency, called electron plasma wave, and a second at a lower frequency, called ion acoustic wave.

1.3.1 Electron plasma waves

The high frequency waves are related to high frequency charge density fluctuations associated with the motion of electrons. Since the ions are much heavier than the electrons, they are considered as immobile. They form a homogeneous, positively charged background distribution of density n_{0i} . The fluids equations for the electrons specie are:

$$\frac{\partial n_e}{\partial t} + \frac{\partial(n_e \vec{u}_e)}{\partial \vec{x}} = 0 \quad (1.3)$$

$$\frac{\partial(n_e u_e)}{\partial t} + \frac{\partial(n_e \vec{u}_e^2)}{\partial \vec{x}} = -\frac{n_e e \vec{E}}{m_e} - \frac{1}{m_e} \frac{\partial p_e}{\partial \vec{x}} \quad (1.4)$$

$$\frac{p_e}{n_e^3} = \text{constant} \quad (1.5)$$

where n_e is the electron plasma density, \vec{u}_e is the electron mean velocity, \vec{E} is the electric field and p_e is the electron pressure. The combination of the fluid equations with the Poisson's equation:

$$\frac{\partial \vec{E}}{\partial \vec{x}} = -4\pi (n_e - Z n_{0i}) \quad (1.6)$$

gives a wave equation describing the small amplitude fluctuations in the electron density:

$$\left(\frac{\partial^2}{\partial t^2} - 3v_e^2 \frac{\partial^2}{\partial \vec{x}^2} + \omega_{pe}^2 \right) \tilde{n}_e = 0 \quad (1.7)$$

where $v_e = \sqrt{k_B T_e / m_e}$ is the electron thermal velocity and k_B is the Boltzmann's constant. From Eq.(1.7) we can derived the dispersion relation for the electron plasma waves:

$$\omega^2(k) = \omega_{pe}^2 + 3v_e^2 k^2 \quad (1.8)$$

1.3.2 Ion acoustic waves

A plasma can also support quasi-neutral density oscillations at a lower frequency determined by ions inertia. To describe this kind of waves we consider the fluid equations for both the electrons and ions species. The ion fluid equations write:

$$\frac{\partial n_i}{\partial t} + \frac{\partial(n_i u_i)}{\partial \vec{x}} = 0 \quad (1.9)$$

$$\frac{\partial(n_i u_i)}{\partial t} + \frac{\partial(n_i u_i^2)}{\partial \vec{x}} = \frac{Z e n_i \vec{E}}{m_i} - \frac{1}{m_i} \frac{\partial p_i}{\partial \vec{x}} \quad (1.10)$$

$$\frac{p_i}{n_i^3} = \text{constant} \quad (1.11)$$

where n_i , u_i , m_i , p_i and Z are the ion density, the mean ion velocity, the ion mass, the ion pressure and the charge state, respectively. In combination with Eqs.(1.3)-(1.4) if we consider the electron as isothermal and neglecting the electron inertia we can find the wave equation describing the ion density fluctuations:

$$\left(\frac{\partial^2}{\partial t^2} - \frac{Z T_e + 3 T_i}{m_i} \frac{\partial^2}{\partial \vec{x}^2} \right) \tilde{n}_i = 0 \quad (1.12)$$

The dispersion relation for the ion acoustic waves is then:

$$\omega(k) = \pm k c_s \quad (1.13)$$

where $c_s = \sqrt{\frac{Z T_e + 3 T_i}{m_i}}$ is the ion acoustic velocity. The condition of existence of this kind of waves is $Z T_e / T_i \ll 1$ otherwise we have a strong Landau damping. Thus often the ion temperature is neglected in the definition of the ion acoustic velocity:

$$c_s = \sqrt{\frac{Z T_e}{m_i}} \quad (1.14)$$

1.4 Stimulated Brillouin and Raman scattering

There are many instabilities and scattering processes that occur in laser-plasma interaction. Two of these instabilities involve the coupling of electromagnetic waves and either an electron plasma wave or an ion acoustic wave. To be precise, the electromagnetic wave decays into a plasma wave and a second electromagnetic wave. If an electron plasma wave is excited the process is called Stimulated Raman Scattering (SRS). In case of an ion plasma wave it is called Stimulated Brillouin Scattering (SBS).

As parametric processes, the secondary waves obey a resonance condition.

$$\begin{aligned}\omega_0 &= \omega_s + \omega_\alpha \\ \vec{k}_0 &= \vec{k}_s + \vec{k}_\alpha\end{aligned}\tag{1.15}$$

where ω_0 (k_0), ω_s (\vec{k}_s), ω_α (\vec{k}_α) are the frequency (wave number) of the incident wave, of the secondary wave and of the plasma wave respectively. For SRS $\omega_\alpha = \omega_{pe}$ ($\vec{k}_\alpha = k_{pe}$) is the frequency (wave number) of a electron plasma wave. For SBS $\omega_\alpha = \omega_{iaw}$ ($\vec{k}_\alpha = k_{iaw}$) is the frequency (wave number) of an ion acoustic wave. The secondary waves are amplified exponentially in the small signal regime. In this regime the depletion of the incident wave is neglected. The two electromagnetic waves drive the plasma wave further by their common ponderomotive force. In a plasma, these instabilities can be used to transfer energy between lasers beams. In particular, in this work we are focusing on a three waves system: in a plasma, a long pump and short seed pulses can be coupled in order to amplify the short pulse. The energy of the pump pulse can be transferred to the seed pulse thanks to the third participating wave. The energy of the long pump pulse being compressed in a short pulse results in field amplification. The SRS mechanism is characterized by a relatively fast plasma wave response allowing the shortest output pulses (\approx fs) and thus the highest intensities, but it needs a fine tuning between the laser frequency ω_0 and the electron wave frequency ω_e in order to satisfy the resonance condition (Eq.(1.15)). However it is affected by kinetics effects [13] and needs a long and homogeneous plasma to be effective. The Brillouin amplification mechanism in the weak coupling regime is limited to longer output pulses (\approx ps) than SRS. However, in the strong coupling regime it can amplify sub-ps pulses at higher intensities and has numerous advantages: the energy transfer between the pump and seed pulses is relatively fast, allowing short interaction lengths. It is robust with respect to frequency-mismatch and plasma inhomogeneities allowing larger growth rates and no parasitic thermal backscattering in the SRS frequency range, as it will be discussed in the following (chapter 4). It can as well operate at higher plasma densities (above 25% of critical density, not discussed here).

1.4.1 Stimulated Brillouin Backscattering

The Brillouin Scattering can be schematically modeled as the coupling of a large amplitude light wave into a scattered light plus an ion acoustic wave. The resonance condition, in terms of frequency and wave number can be written as:

$$\begin{aligned}\omega_0 &= \omega_s + \omega \\ \vec{k}_0 &= \vec{k}_s + \vec{k}\end{aligned}\tag{1.16}$$

where ω_0 and k_0 are the frequency and the wave number vector of the incident light, ω_s and k_s are the frequency and the wave number of the scattered wave and ω and k are the frequency and the wave number of the ion acoustic wave. The coupled equations that describe the Brillouin instability can be derived starting to consider the propagation of a light wave in a plasma. In particular, from the Ampere's equation:

$$\nabla \times \vec{B} = \frac{4\pi}{c} \vec{J} + \frac{1}{c} \frac{\partial \vec{E}}{\partial t} \quad (1.17)$$

we obtain:

$$\left(\frac{1}{c^2} \frac{\partial^2}{\partial t^2} - \nabla^2 \right) \vec{A} = \frac{4\pi}{c} \vec{J} - \frac{1}{c} \frac{\partial \nabla \phi}{\partial t} \quad (1.18)$$

where \vec{A} is the vector potential, ϕ is the electrostatic potential. The electromagnetic field and the electric field are related to the vector potential as $\vec{B} = \nabla \times \vec{A}$ and $\vec{E} = -\frac{1}{c} \frac{\partial \vec{A}}{\partial t} - \nabla \phi$. The current term can be split in a longitudinal term \vec{J}_l and a transverse one \vec{J}_t , so that $\vec{J} = \vec{J}_l + \vec{J}_t$. The longitudinal current, associated with the electrostatic plasma wave, can be related to the electrostatic potential:

$$\frac{\partial}{\partial t} \nabla \phi = 4\pi \vec{J}_l \quad (1.19)$$

so that Eq.(1.18) becomes:

$$\left(\frac{1}{c^2} \frac{\partial^2}{\partial t^2} - \nabla^2 \right) \vec{A} = \frac{4\pi}{c} \vec{J}_t \quad (1.20)$$

As the transverse current \vec{J}_t is associated with the incident light wave, it can expressed as:

$$\vec{J}_t = -\frac{n_e e^2 \vec{A}}{m_e c} \quad (1.21)$$

Substituting Eq.(1.21) in Eq.(1.20) we obtain the equation for the propagation of a light wave in a plasma:

$$\left(\frac{\partial^2}{\partial t^2} - c^2 \nabla^2 \right) \vec{A} = -\frac{4\pi e^2}{m_e} n_e \vec{A} \quad (1.22)$$

The vector potential \vec{A} can be intended now as the sum of two terms, one that is the incident large light wave \vec{A}_p and the other \vec{A}_s that is the scattered wave, so that $\vec{A} = \vec{A}_p + \vec{A}_s$. If now we write the electron density as sum of uniform density background n_{e0} plus a small density fluctuation \tilde{n}_e , $n_e = n_{e0} + \tilde{n}_e$, we obtain:

$$\left(\frac{\partial^2}{\partial t^2} - c^2 \nabla^2 + \omega_{pe}^2 \right) \vec{A}_s = -\frac{4\pi e^2}{m_e} \tilde{n}_e \vec{A}_p \quad (1.23)$$

In Eq.(1.23) the term \tilde{n}_e represents the electron density fluctuations at low frequency associated with an ion acoustic wave. To derive a relation relying the electron density fluctuations and the incident light wave, we write the momentum electron fluid equation, in which the velocity \vec{u}_e is split into a longitudinal component \vec{u}_l and a transverse component $\vec{u}_t = \frac{e\vec{A}}{m_e c}$:

$$\frac{\partial \vec{u}_l}{\partial t} = \frac{e}{m_e} \nabla \phi - \frac{1}{2} \nabla \left(\vec{u}_l + \frac{e\vec{A}}{m_e c} \right)^2 - \frac{\nabla p_e}{n_e m} \quad (1.24)$$

This equation can be simplified considering $\vec{A} = \vec{A}_p + \vec{A}_s$, $n_e = n_{e0} + \tilde{n}_e$ and an isothermal electrons response, obtaining,

$$\frac{e}{m_e} \nabla \phi = \frac{e^2}{m_e^2 c^2} \nabla \left(\vec{A}_p \cdot \vec{A}_s \right) + \frac{v_e^2}{n_{e0}} \nabla \tilde{n}_e \quad (1.25)$$

The ion fluid equations write:

$$\begin{aligned} \frac{\partial n_i}{\partial t} + \nabla \cdot (n_i \vec{u}_i) &= 0 \\ \frac{\partial \vec{u}_i}{\partial t} + \vec{u}_i \cdot \nabla \vec{u}_i &= -\frac{Ze}{m_i} \nabla \phi \end{aligned} \quad (1.26)$$

The linearization of these equations can be done imposing $n_i = n_{i0} + \tilde{n}_i$ and $\vec{u}_i = \vec{u}_i$. The combination of them gives:

$$\frac{\partial^2 \tilde{n}_i}{\partial t^2} - \frac{n_{i0} Ze}{m_i} \nabla^2 \phi \quad (1.27)$$

We can now replace the equation for the electrostatic potential $\tilde{\phi}$ given by Eq.(1.25) and we obtain the equation that describes the excitation of the ion acoustic by the beating of the incident wave \vec{A}_p with the scattered light \vec{A}_s :

$$\frac{\partial^2 \tilde{n}_e}{\partial t^2} - c_s^2 \nabla^2 \tilde{n}_e = \frac{Z n_{e0} e^2}{m_e m_i c^2} \nabla^2 \left(\vec{A}_p \cdot \vec{A}_s \right) \quad (1.28)$$

We have then a system of two equations (Eqs.(1.23)(1.28)) describing the relation among the incident light \vec{A}_l , the scattered light \vec{A}_s and the ion acoustic plasma wave. We consider now the case where we have two counter-propagating lasers beams, one that we call pump beam that is long and energetic and a second short one that is shorter and generally smaller in intensity: these beams are interacting between each other and there are creating the ion acoustic perturbation. The pump is then diffusing of this perturbation and part of its energy is backscattered towards the seed beam. The system of equation is :

$$\left(\frac{\partial^2}{\partial t^2} - c^2 \nabla^2 + \omega_{pe}^2\right) \vec{A}_p = -\omega_{pe}^2 \frac{\tilde{n}_e}{n_{e0}} \vec{A}_s, \quad (1.29)$$

$$\left(\frac{\partial^2}{\partial t^2} - c^2 \nabla^2 + \omega_{pe}^2\right) \vec{A}_s = -\omega_{pe}^2 \frac{\tilde{n}_e}{n_{e0}} \vec{A}_p, \quad (1.30)$$

$$\left(\frac{\partial^2}{\partial t^2} - c_s^2 \nabla^2\right) \tilde{n}_e n_{e0} = \frac{Ze^2}{c^2 m_e m_i} \nabla^2 (\vec{A}_p \cdot \vec{A}_s). \quad (1.31)$$

where A_p is the potential vector of the pump beam, A_s is the potential vector of the seed beam, Z is the ion charge, n_{e0} and n_{e0}/Z are the unperturbed electron and ion densities, $c_s = \sqrt{ZT_e/m_i}$ is the ion acoustic velocity, c is the light speed in vacuum and ω_{pe}^2 is the electron plasma frequency. For the pump and seed lasers counter-propagating along x with the pump in the direction of positive x , the electric fields can be written, in a one-dimensional problem:

$$E_p = \frac{1}{2}(E_p e^{-i(-k_{0p}x + \omega_{0p}t)} + E_p^* e^{i(-k_{0p}x + \omega_{0p}t)}), \quad (1.32)$$

$$E_s = \frac{1}{2}(E_s e^{-i(k_{0s}x + \omega_{0s}t)} + E_s^* e^{i(k_{0s}x + \omega_{0s}t)}). \quad (1.33)$$

where $k_{0p,0s}$ and $\omega_{0p,0s}$ are the wave-vectors and the frequencies of the pump and seed in vacuum, respectively. Considering that $\vec{E} = -\frac{1}{c} \frac{\partial \vec{A}}{\partial t}$ and that the envelopes of the electric fields vary slowly on a period $1/\omega_{0p,0s}$ and on a wavelength $1/k_{0p,0s}$, it is possible to write:

$$(\partial_t + v_g^p \partial_x) E_p = -i \frac{\omega_{pe}^2}{4\omega_{0p}} \frac{n}{n_0} E_s e^{i[(k_s - k_p)x - (\omega_{0s} - \omega_{0p})t]}, \quad (1.34)$$

$$(\partial_t - v_g^s \partial_x) E_s = -i \frac{\omega_{pe}^2}{4\omega_{0s}} \frac{n^*}{n_0} E_p e^{i[(k_p - k_s)x - (\omega_{0p} - \omega_{0s})t]}, \quad (1.35)$$

$$(\partial_t^2 - c_s^2 \partial_x^2) \frac{n}{n_0} = -\frac{Ze^2 (k_p + k_s)^2}{2m_e m_i \omega_{0p} \omega_{0s}} E_p E_s^* e^{i(k_p + k_s)x} e^{-i(\omega_{0p} - \omega_{0s})t}. \quad (1.36)$$

Here $k_{p,s}$ and $\omega_{p,s}$ are the wave-vectors and the frequencies of the pump and seed in the plasma and $v_g^{p,s}$ are the group velocities for the pump and seed laser, respectively.

If we write the density perturbation as:

$$\frac{n}{n_0} = N e^{ikx}, \quad (1.37)$$

where $k = k_p - k_s \approx 2k_p$, Eq.(1.36) becomes:

$$(\partial_t^2 - c_s^2 \partial_x^2 - 4ik_p c_s^2 \partial_x + 4k_p^2 c_s^2)N = -\frac{2Ze^2}{m_e m_i c^2} E_p E_s^* e^{-i(\omega_{0p} - \omega_{0s})t}. \quad (1.38)$$

From Eq.(1.38) we can now distinguish two regime, the so-called weak and the strong coupling regimes.

Weak coupling regime

The so-called weak coupling regime corresponds to the limit where the ion-acoustic wave is resonant, and to lowest order $\partial/\partial t \sim kc_s$. With $\omega \approx kc_s$ is than possible to consider $N = N(t)e^{-i\omega t}$ so that $i\partial/\partial t = \omega + i\partial/\partial t$, where now the time derivative indicates a slow time variation with respect to the acoustic frequency, $\partial/\partial t \ll kc_s$. By using this assumptions, and considering the resonance condition $\omega = \omega_{0p} - \omega_{0s}$ in Eq.(1.34)(1.35)(1.38) we obtain:

$$(\partial_t + v_g^p \partial_x) E_p = -i \frac{\omega_{pe}^2}{4\omega_{0p}} N E_s \quad (1.39)$$

$$(\partial_t - v_g^s \partial_x) E_s = -i \frac{\omega_{pe}^2}{4\omega_{0s}} N^* E_p \quad (1.40)$$

$$(\partial_t + c_s \partial_x) N = -i \frac{Ze^2}{2m_e m_i c^2 k_{0p} c_s} E_p E_s^* \quad (1.41)$$

In the linear regime (i.e. such that $E_p \approx$ constant) it is possible to consider an exponential growth , $N = N e^{\gamma t}$ with $\gamma \ll kc_s$ for a constant profile in space. The seed will have the same form, $E_s = E_s e^{\gamma t}$ with growth rate given by :

$$\gamma = \frac{1}{2\sqrt{2}} \frac{k_p v_{osc} \omega_{pi}}{\sqrt{\omega_{0p} k_p c_s}} \quad (1.42)$$

$$k = 2k_p - \frac{2\omega_{0s} c_s}{c^2} \approx 2k_p \quad (1.43)$$

where $v_{osc} = eE_p/m_e \omega_{0p}$.

Strong coupling regime

In Eq.(1.38), since we are interested in the strong-coupling limit [24], ∂_t^2 is much larger than $4k_{0p}^2 c_s^2$, so we can neglect this term on the left hand side. We still leave the possibility of $\partial_x > k_{0p}$, and thus we can write:

$$(\partial_t^2 - c_s^2 \partial_x^2)N = -\frac{2Ze^2}{m_e m_i c^2} E_p E_s^* e^{-i(\omega_{0p} - \omega_{0s})t}. \quad (1.44)$$

The above condition for strong coupling regime ($\partial_t^2 \gg 4k_{0p}^2 c_s^2$) is satisfied when:

$$\left(\frac{v_{osc}}{v_e}\right)^2 > 4k_0 c_s \frac{\omega_{0p}}{\omega_{pe}^2}. \quad (1.45)$$

where $v_{osc} = eE_0/\omega_{0p}m_e$ and $v_e = \sqrt{T_e/m_e}$.

In more practical units, it is possible to write Eq.(1.45):

$$I_{14} \lambda_{0p}^2 > 1.1 \times 10^{-1} T_e^{3/2} (n_c/n_0) (1 - n_0/n_c)^{1/2}. \quad (1.46)$$

In Eq.(1.46) I_{14} is the pump laser intensity in units of 10^{14}W/cm^2 , λ_{0p} is the laser wavelength expressed in μm , T_e is the electron temperature in keV and $n_c = \frac{\epsilon_0 m_e \omega_{0p}^2}{e^2}$ is the critical density.

Making the hypothesis that $\omega_{0p} \approx \omega_{0s}$, Eqs.(1.34)(1.35)(1.44) can be written as:

$$(\partial_t + v_g^p \partial_x) E_p = -i \frac{\omega_{pe}^2}{4\omega_{0p}} N E_s, \quad (1.47)$$

$$(\partial_t - v_g^s \partial_x) E_s = -i \frac{\omega_{pe}^2}{4\omega_{0s}} N^* E_p, \quad (1.48)$$

$$(\partial_t^2 - c_s^2 \partial_x^2) N = -\frac{2Ze^2}{m_e m_i c^2 k_p c_s} E_p E_s^*. \quad (1.49)$$

In Eqs.(1.47)(1.48)(1.49) we have already taken into account the condition $k \approx 2k_p$, so that the spatial variations is for the envelope. If we take $N = N e^{-i\omega t}$, $E_s = E_s e^{i\omega^* t}$ and E_p as a constant, we obtain the so-called linear sc-SBS solution, that is exponential growth, with:

$$\omega = \omega_{sc} \equiv \bar{\omega}_{sc} + i\gamma_{sc}, \quad (1.50)$$

$$\omega_{sc} = \left(\frac{k_p^2 v_{osc}^2 \omega_{pi}^2}{2\omega_{0p}}\right)^{1/3} \left(\frac{1}{2} + i\frac{\sqrt{3}}{2}\right). \quad (1.51)$$

Hence, in the strong coupling regime the frequency of the electrostatic wave is mostly determined by the amplitude of the pump light wave (v_{osc}), and $|\omega_{sc}| \gg 2k_p c_s$, that corresponds to Eq.(1.45).

The growth rate of the SBS instability is the imaginary part of Eq.(1.51):

$$\gamma_{sc} = \left(\frac{k_p^2 v_{osc}^2 \omega_{pi}^2}{2\omega_{0p}} \right)^{1/3} \left(\frac{\sqrt{3}}{2} \right). \quad (1.52)$$

Eq (1.52) can be normalized to ω_{0p} and expressed in more practical units:

$$\frac{\gamma_{sc}}{\omega_{0p}} = 5.04 \times 10^{-8} (I_p [W/cm^2] \lambda^2 [\mu m])^{1/3} \left(1 - \frac{n_e}{n_c} \right)^{1/3} \left(\frac{n_e}{n_c} \right)^{1/3} \left(\frac{Z}{A} \right)^{1/3} \quad (1.53)$$

From Eq.(1.47)(1.48)(1.49) it is possible to obtain a self-similar solution [27] in which the seed evolution is described in correspondence with the pump depletion. In most of the simulations presented in this paper we enter the self-similar regime where there is efficient energy transfer from the pump to the seed. In order to study the pump to seed energy transfer in the strong coupling regime and with relatively short pumps (typically few ps) and seed (typically some 100 fs), we recall that such pulses are compressed by the chirped pulse amplification (CPA) technique. In particular, motivated by current day experimental conditions, we can include the effect of a chirp in the pump. Thus we consider a pump laser with the electric field expressed as:

$$E_p \propto e^{i(k_0 x - \omega_0 t + \phi(x,t))} \quad (1.54)$$

where the phase variation due to the chirp is:

$$\phi(x, t) = \alpha(k_0(x - x_0) - \omega_0(t - t_0))^2 \quad (1.55)$$

This corresponds to the propagation of a laser pulse with a time dependent frequency:

$$\omega(x, t) = \omega_0 - \frac{\partial \phi(x, t)}{\partial t} = \omega_0 + 2\alpha(k_0(x - x_0) - \omega_0(t - t_0)) \quad (1.56)$$

On a given point x_0 the frequency is evolving linearly with time. x_0 and t_0 indicate the centering of the chirp, where the nominal frequency ω_0 of the laser pulse is located. With this convention for the phase of the chirp, at x_0 , the frequency is varying as:

$$\omega(t) = \omega_0 - 2\alpha\omega_0^2(t - t_0) \quad (1.57)$$

The corresponding wavelength evolution is:

$$\lambda(t) \approx \lambda_0 + 4\pi c\alpha(t - t_0) \quad (1.58)$$

The results of Eq.(1.57)(1.58) are shown in Fig.(1.2) in function of $t - t_0$, at $x = x_0$

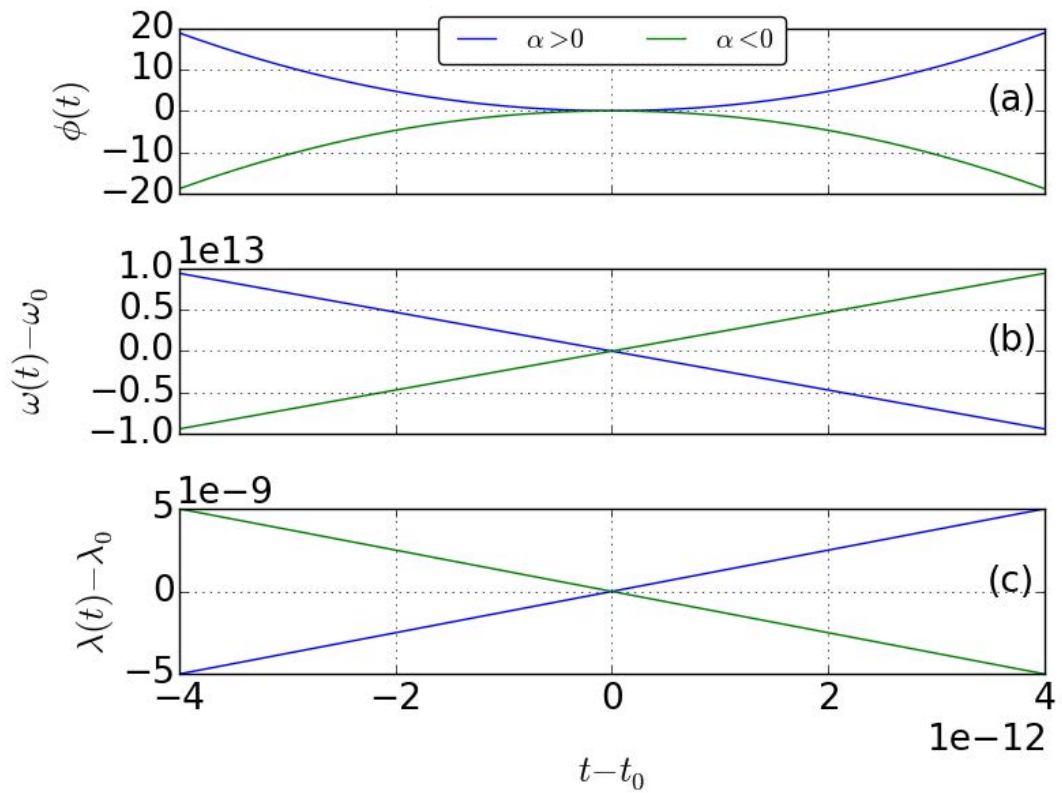


Figure 1.2: Chirp phase $\phi_s(t)$ (a), frequency $\omega(t) - \omega_0$ (b) and wavelength $\lambda - \lambda_0$ (c) values in function of time and for $\alpha = 3.3 \times 10^{-7}$ (blue line) and $\alpha = -3.3 \times 10^{-7}$ (green line)

and for $|\alpha| = 3.3 \times 10^{-17}$: when $\alpha = 3.3 \times 10^{-7} > 0$, the chirp phase shape has a positive concavity (Fig.(1.2(a)), blue line) and the laser pulse pulse frequency is varying from high values to lower ones (Fig.(1.2(b)), blue line). On the opposite, when $\alpha = -3.3 \times 10^{-7} < 0$, the laser frequency is varying from lower values to higher ones (Fig.(1.2(b)), green line).

In the presence of chirp, Eq.(1.47)-(1.49) become:

$$(\partial_t + v_g^p \partial_x) E_p = -i \frac{\omega_{pe}^2}{4\omega_{0p}} N E_s e^{-i\phi} \quad (1.59)$$

$$(\partial_t - v_g^s \partial_x) E_s = -i \frac{\omega_{pe}^2}{4\omega_{0s}} N^* E_p e^{i\phi} \quad (1.60)$$

$$(\partial_t^2 - c_s^2 \partial_x^2) N = -\frac{2Ze^2}{m_e m_i c^2} E_p E_s^* e^{i\phi} \quad (1.61)$$

1.4.2 Stimulated Raman Backscattering

A similar approach can be followed to derive the dispersion relation of the Stimulated Raman Backscattering. In this case the pump and seed beams are coupling each other and creating an high frequency electron density fluctuation. The resonance conditions are now:

$$\begin{aligned} \omega_0 &= \omega_s + \omega_{pe} \\ \vec{k}_0 &= \vec{k}_s + \vec{k}_{pe} \end{aligned} \quad (1.62)$$

where ω_0 and k_0 are, as before, the frequency and the wave number vector of the incident light, ω_s and k_s are the frequency and the wave number of the scattered wave and ω_{pe} and k_{pe} are the frequency and the wave number vector of the electron plasma wave. As the minimum allowed frequency of a beam traveling in a plasma is dictated by ω_{pe} , the Raman instability can exist only for density lower of $n_{cr}/4$. Following the same procedure than before, we can then couple Eq.(1.24) with the electron fluid linearized equations for mass and momentum conservation, obtaining:

$$\left(\frac{\partial^2}{\partial t^2} + \omega_{pe} - 3v_e^2 \nabla^2 \right) \tilde{n}_e = \frac{n_{e0} e^2}{m_e c^2} \nabla \cdot (\vec{A}_l + \vec{A}_s) \quad (1.63)$$

If now we consider a three waves coupling between the pump laser, the seed beam and the density perturbation excited, we can write:

$$\left(\frac{\partial^2}{\partial t^2} - c^2 \nabla^2 + \omega_{pe}^2\right) \vec{A}_p = -\omega_{pe}^2 \frac{n}{n_0} \vec{A}_s, \quad (1.64)$$

$$\left(\frac{\partial^2}{\partial t^2} - c^2 \nabla^2 + \omega_{pe}^2\right) \vec{A}_s = -\omega_{pe}^2 \frac{n}{n_0} \vec{A}_p, \quad (1.65)$$

$$\left(\frac{\partial^2}{\partial t^2} + \omega_{pe} - 3v_e^2 \nabla^2\right) \frac{n}{n_0} = \frac{e^2}{c^2 m_e^2} \nabla^2 (\vec{A}_p \cdot \vec{A}_s). \quad (1.66)$$

The exponential growth rate of the instability γ_{SRS} , in the case of direct backscatter, is, in practical units:

$$\gamma_{SRS} = 4.27 \times 10^{-3} \left(\frac{n}{n_c}\right)^{1/4} (I_{14} \lambda_{0p}^2)^{1/2} \omega_{0p} \quad (1.67)$$

where the density is expressed in units of critical density, I_{14} is the pump intensity in units of $10^{14} W/cm^2$, and λ_{0p} and ω_{0p} are the pump wavelength and frequency in vacuum. For typical parameters that we use in this work ($n/n_c = 0.05 - 0.1$, $I_p = 10^{15} W/cm^2$) we have $\gamma_{SRS}^{-1} \approx 78 - 66 fs$. Notice that the strong coupling regime may exists also for SRS, however it requires relativistic intensities not studied in this work.

Chapter 2

Energy flow directionality and time scale characterization in the strong coupling regime for SBS

In this chapter we explore the energy directionality and the characteristic time scales of the SBS amplification. To do so, we rewrite the system of equation describing the SBS amplification in the strong coupling regime (Eq.(1.59)-(1.61)) explicitly in terms of amplitudes and phases of the pump and seed beams and plasma density perturbation. As will be discussed in detail, in contrast to the weak-coupling regime of Brillouin backscattering and standard optical parametric amplification (OPA) techniques [46], the phase relation among pump, seed and plasma density perturbation is continuously time-dependent. The description of the evolution in time of the phases of the three waves allows one to give an explanation concerning the energy flow direction during the amplification process and determines the quality of the amplification. The chapter is organized as follows: in Sec. 2.1 we briefly remind the results in the weak coupling regime. In this regime the total phase (defined as the combination of the phases of the pump, seed and plasma density perturbation) is locked at $\vartheta = \pi/2$ and that the transfer direction of the energy is determined by this value of phase. In Sec. 2.3 we describe the total phase evolution in terms of the maximum growth rate γ_{sc} for the different stages of the amplification: we show that, during the very first moments of the coupling, the total phase is determined by the seed and that it is evolving in time to reach the value of $\vartheta = -4\pi/3$. When this particular value is reached ($t\gamma_{sc} \approx 2$), the seed enters the linear regime (exponential growth) of amplification and the total phase is almost constant until the pump starts to be depleted and the seed enters in the self-similar regime ($t\gamma_{sc} \approx 4.67$ for $I_{p0}/I_{s0} = 100$). At that point the total phase starts to oscillate around $-\pi$ continuously inverting the energy flow direction, leading to the

oscillations behind the first peak that are the analogous of the π -pulse for the weak coupling regime. The results of the numerical simulations have been obtained solving numerically the SBS coupling equations (1.59)-(1.61) in one dimension: this allows one to study the evolution of the seed amplification in the pure Brillouin regime without having to take into account the other instabilities, such as SRS, that can affect the amplification.

2.1 Weak coupling regime

In this section we briefly study the energy flow direction in the weak coupling regime and how this flow is determined by the sign of the phase matching between pump and seed beams and density perturbation. To do so, we consider the evolution of the phase from the beginning of the process in an homogeneous system, in which the pump, the seed and the initial plasma density shape are constant. In Sec. 1.4.1 of the introduction we showed that the system of coupled equations describing the amplification in the weak coupling regime writes:

$$(\partial_t + v_g^p \partial_x) E_p = -i\mu_p N E_s \quad (2.1)$$

$$(\partial_t - v_g^s \partial_x) E_s = -i\mu_s N^* E_p \quad (2.2)$$

$$(\partial_t + c_s \partial_x) N = -i\zeta E_p E_s^* \quad (2.3)$$

where E_p , E_s and N are the wave function for the pump, the seed and the density perturbation and μ_s , μ_p and ζ are the coupling factors defined as:

$$\mu_p = \frac{\omega_{pe}^2}{4\omega_{0p}} \quad (2.4)$$

$$\mu_s = \frac{\omega_{pe}^2}{4\omega_{0s}} \quad (2.5)$$

$$\zeta = \frac{Ze^2}{2m_e m_i c^2 k_{0p} c_s} \quad (2.6)$$

Let us decompose the waves functions in their amplitude (defined as a positive quantity) and a phase, so that $A \rightarrow Ae^{i\varphi}$. We can define a total phase that takes into account this combination:

$$\vartheta = \varphi_p - \varphi_s - \varphi \quad (2.7)$$

where φ_p , φ_s , φ are the phases of the pump, of the seed and of the density perturbation respectively. We already assumed phase matching by imposing the resonant condition, and now we can, with no loss of generality, consider that initial pump and seed phases are unperturbed and equal to zero, $\varphi_p = \varphi_s = 0$, and the density perturbation is zero.

According to the system of equations above the density perturbation growth is:

$$N(t) = -i\zeta E_p E_s^* t \quad (2.8)$$

From Eq.(2.8), with the assumptions above, we find that the phase of the density perturbation is given by $\varphi = -\frac{\pi}{2}$ and the global phase is $\vartheta = \frac{\pi}{2}$. If we consider the growth of the ion acoustic wave at a fixed location in the plasma and neglect the convective term, we can simplify the system of equations above and explicit the subsequent evolution of the amplitude and the phase of the waves:

$$\partial_t E_p = -\mu_p N E_s \sin \vartheta \quad (2.9)$$

$$\partial_t \varphi_p = -\mu_p \frac{N E_s}{E_p} \cos \vartheta \quad (2.10)$$

$$\partial_t E_s = \mu_s N E_p \sin \vartheta \quad (2.11)$$

$$\partial_t \varphi_s = -\mu_s \frac{N E_p}{E_s} \cos \vartheta \quad (2.12)$$

$$\partial_t N = \zeta E_p E_s \sin \vartheta \quad (2.13)$$

$$\partial_t \varphi = -\zeta \frac{E_p E_s}{N} \cos \vartheta \quad (2.14)$$

It is clear from the equations above that the phases of the different waves will appear in the same combination. The global phase ϑ is the relevant quantity that determines the efficiency of the coupling. Since initially we have that the global phase is $\vartheta = \frac{\pi}{2}$, the density perturbation, pump and seed phases φ , φ_p and φ_s are constant during the whole process, as the coupling term on the right of Eqs.(2.10)(2.12)(2.14) is zero. This means that the global phase stays constant at $\vartheta = \frac{\pi}{2}$. From Eqs.(2.9)(2.11) we have then:

$$\begin{aligned} \partial_t E_s &> 0 \\ \partial_t E_p &< 0 \end{aligned} \quad (2.15)$$

The energy flows from the pump to the seed. However, as the pump electric field amplitude decreases and eventually goes to zero, the global phase flips, and we have $\vartheta = -\frac{\pi}{2}$. At this new value of the global phase, the phases are constant again, but now the energy transfer goes in the opposite direction, from the seed to the pump. This is the so-called pi-pulse. In the following section we show that, for the strong coupling

regime, the phases are not locked anymore but in continuous evolution with the time.

2.2 Strong coupling regime

As done in Sec. 2.1, it is useful to explicit the time evolution of the amplitude and the phase of the fields from Eqs.(1.59)-(1.61), $A_\alpha \rightarrow A_\alpha e^{i\varphi_\alpha}$, for $\alpha = p, s$ and $N = N e^{i\varphi}$:

$$(\partial_t + v_g^p \partial_x) E_p = -\mu N E_s \sin \vartheta \quad (2.16)$$

$$(\partial_t + v_g^p \partial_x) \varphi_p = -\mu \frac{N E_s}{E_p} \cos \vartheta \quad (2.17)$$

$$(\partial_t - v_g^s \partial_x) E_s = \mu N E_p \sin \vartheta \quad (2.18)$$

$$(\partial_t - v_g^s \partial_x) \varphi_s = -\mu \frac{N E_p}{E_s} \cos \vartheta \quad (2.19)$$

$$\partial_t^2 N - N(\partial_t \varphi^2) - c_s^2(\partial_x^2 N - N(\partial_x \varphi^2)) = -\Lambda E_p E_s \cos \vartheta \quad (2.20)$$

$$N \partial_t^2 \varphi - c_s^2 N \partial_x^2 \varphi + 2 \partial_t N \partial_t \varphi - 2 c_s^2 \partial_x N \partial_x \varphi = -\Lambda E_p E_s \sin \vartheta \quad (2.21)$$

where μ and Λ are the coupling factor for the fields and the density perturbation respectively:

$$\mu = \frac{\omega_{pe}^2}{4\omega_0} \quad (2.22)$$

$$\Lambda = \frac{2Z e^2}{m_e m_i c^2} \quad (2.23)$$

In Eq.(2.16)-(2.21) that quantity that appears on the right hand side ϑ is the global phase:

$$\vartheta = \varphi_p - \varphi_s - \varphi + \phi \quad (2.24)$$

2.3 Different phases of the amplification in the strong-coupling limit

In these section we examine in detail the amplification process in the simplest case where the chirp is zero and the plasma density profile, pump and seed are constants. We will examine in the next chapter the effect of finite pulse duration, and inhomogenous

density profiles. In order to support our theoretical analysis and estimates we solve numerically Eq.(1.59)(1.60)(1.61) with $\alpha = 0$, for plasma and laser conditions such that SBS develops in the strong-coupling regime for the case of a plasma of constant density, and the pump and seed laser beams such that the intensity ramps up in a short time up to a constant value, and then stays constant. We examine in detail the results of a simulation with the following parameters motivated by recent experiments [34]. The pump and seed lasers have an intensity of $I_{pump} = 10^{15} \text{W/cm}^2$ and $I_{seed} = 10^{13} \text{W/cm}^2$, respectively. The same wavelength $\Lambda_0 = 1 \mu\text{m}$ has been used for both laser beams, corresponding to a frequency $\omega_0 = 1.9 \times 10^{15} \text{rad/s}$.

The plasma has a length of $L_p = 600 \mu\text{m}$ and a constant density of $n/n_c = 0.1$; $50 \mu\text{m}$ of vacuum are left on both side of plasma. For these values of pump intensity and plasma density, from Eq.(1.53), $\gamma_{sc} \approx 4.29 \times 10^{12} \text{ s}^{-1}$ corresponding to 233 fs. The simulation starts with the laser beams in the simulation box, crossing at $x_{cross} = 350 \mu\text{m}$; the time ramp for the lasers is $t_{slope} = 30 \text{ fs}$. This case correspond to an efficient amplification and allows to study in detail and define the different stages of the amplification process. The results of the amplification are shown in Figs.(2.1)(2.2). In Fig. (2.1) we show the amplification as function fo space ($t = 0$) at the beginning (Fig.(2.1)(a)) and at the end of the interaction ($t_{end} = 1.5 \text{ ps}$, time necessary for the seed laser to propagate inside half of the simulation box) (Fig.(2.1)(b)). In Fig.(2.2) we show the pump and seed electric field amplitudes (Fig.(2.2)(c)) and the phases evolution (Fig.(2.2)(a)(b)) as a function of time by recording the informations about electric fields, density perturbation amplitudes and phase evolution in the middle of the simulation box, at $x = 350 \mu\text{m}$ (dashed vertical line in Fig.(2.1)). The initial simulations set-up with both the laser already in the middle of the plasma allows one to start with a condition in which the plasma is not perturbed yet and the seed and pump amplitude are constant.

We can deduce analytically form the equations presented in the previous chapter the time evolution of the pump, seed and density perturbation amplitudes, in order to define the directionality of the energy flow and compare with Fig.(2.2). In the green shadowed regions of Fig.(2.2(b)) the energy flows from the pump to seed and the blue regions viceversa. Various characteristic times can be identified for each step of the amplification, i) the initial seed growth time ($t\gamma_{sc} \approx 2$ in Fig.(2.2)), ii) the saturation of the growth at a given position (line shadowed region for $2 < t\gamma_{sc} < 4.3$ in Fig.(2.2)), and finally iii) the time when the energy flow flips, from seed to pump, and the growth saturates (dashed-dotted line for $t\gamma_{sc} \approx 4.67$ in Fig.(2.2)). At this time the seed reaches the maximum value of the electric field at a given position. At later time the situation reverses and a second pulse in the seed grows again but at much smaller amplitude. In the following we will analyze in detail all the different phases of the amplification.

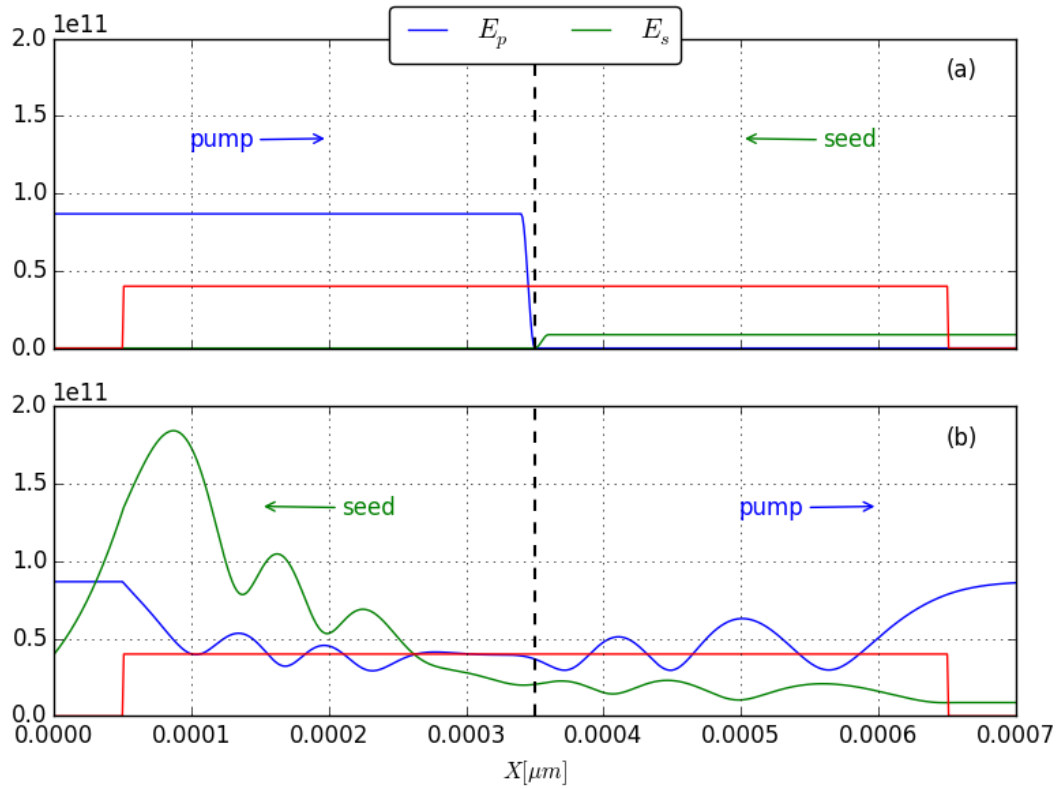


Figure 2.1: Electric fields amplitudes, in V/m , of the pump (blue line) and of the seed (green line) at the beginning (a) and after $t_{end} = 1.5$ ps (b). The unperturbed density profile is in red, in arbitrary units.

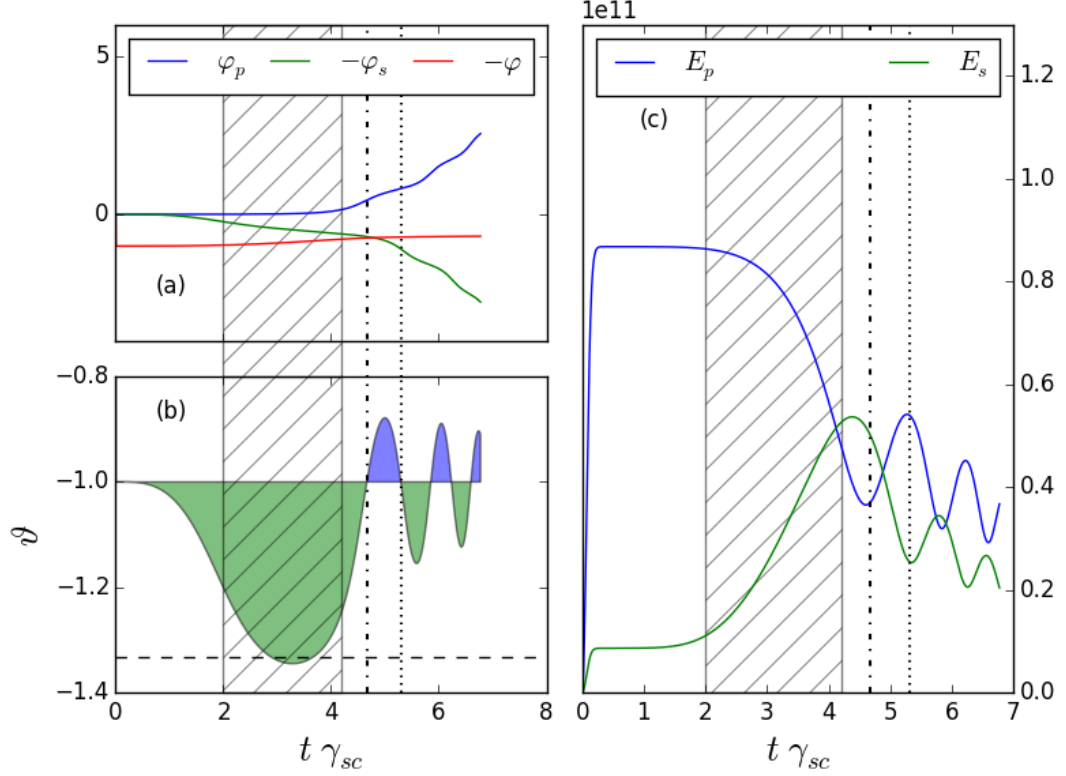


Figure 2.2: a) Evolution in time of the phases of the pump (φ_p , blue line), of the seed ($-\varphi_s$, green line) and density perturbation ($-\varphi$, red line) in function of time and in units of π . b) Time evolution of the total phase ϑ as defined in Eq.(2.24), in units of π . The green shadowed regions indicate the values of ϑ for which the pump amplifies the seed; the blue ones corresponds to a reversed flow energy direction (the seed amplifies the pump). c) Electric fields amplitudes, in V/m , of the pump (blue line) and of the seed (green line) in function of time. All these results are evaluated at the initial crossing point of the lasers, $\hat{x} = 0$ ($x = 350\mu m$)

2.3.1 Initial seed growth

To perform our analysis, and compare with the numerical results we will study Eq.(2.16)-(2.21) at the initial crossing point $x_{cross} = 350\mu m$. In particular, we make our analysis in a new space frame in which Eq.(2.16)-(2.21) are related to $\hat{x} = x - x_{cross}$ and in a way that the pump and seed lasers are overlapping on the domain:

$$-v_g t \leq \hat{x} \leq v_g t \quad (2.25)$$

Let us consider without loss of generality that at $t = 0$ the density perturbation is zero, and the pump and seed fields phases are the same ($\varphi_p = \varphi_s = 0$). At a given point \hat{x} , the lasers crossing starts at a time given by:

$$t_0 = \frac{|\hat{x}|}{v_g} \quad (2.26)$$

Making these hypothesis it is possible to solve for the density from Eq. (2.20), in which we neglect the terms multiplied by c_s^2 and, since $N \approx 0$ at the beginning we neglect the second terms in Eq. (2.20):

$$\partial_t^2 N \approx -\Lambda E_p E_s \cos \vartheta \quad (2.27)$$

If we integrate Eq.(2.27), we find that the plasma perturbation N is :

$$N(\hat{x}, t) = -\Lambda E_p E_s \frac{(t - t_0)^2}{2} \cos \vartheta = -\Lambda E_p E_s \frac{\left(t - \frac{|\hat{x}|}{v_g}\right)^2}{2} \cos \vartheta \quad (2.28)$$

Since N has to be positive, and the fields amplitudes are now defined as positive, we deduce from Eq.(2.28) that $\cos \vartheta = -1$, $\vartheta = -\pi$ and $\varphi = \pi$. Making the hypothesis that, at the beginning of the interaction the derivative in space is zero, Eq. (2.17) and Eq. (2.19) can be written as:

$$\partial_t \varphi_p = \mu N E_s / E_p$$

$$\partial_t \varphi_s = \mu N E_p / E_s$$

These equations describe the evolution of the pump and seed phases. At the beginning, the pump laser has an higher intensity compared to the seed one, $E_p \gg E_s$, and as a consequence

$$\partial_t \varphi_s \gg \partial_t \varphi_p \approx 0$$

This means that φ_p that was taken initially zero will stay so, and φ_s will growth

$$\vartheta \approx -\pi + \varphi_p - \varphi_s < -\pi$$

From Eq.(2.16) and (2.18) we deduce that the energy flows from the pump to the seed since:

$$\begin{aligned} \partial_t E_s &> 0 \\ \partial_t E_p &< 0 \end{aligned} \quad (2.29)$$

In a first stage as long as the pump locally is more intense than the seed $E_p > E_s$ the pump laser gives energy to the seed and the phase of the ion-acoustic wave imposes that the pump amplifies the seed. In Fig.(2.2(b)), this corresponds to the green shadowed region. The values of the total phase dictate the direction of the energy transfer: if $-2\pi < \vartheta < -\pi$ it means that $\sin \vartheta > 0$ and the energy direction is dictated by Eq.(2.29) (green regions in Fig.(2.2(b))). Otherwise, if $-\pi < \vartheta < 0$, $\sin \vartheta < 0$ the energy flow direction flips and the pump is amplified by the seed (blue regions in Fig.(2.2(b))). From the Eq.(2.19) for the phase of the seed φ_s , it is possible to obtain the frequency shift at the beginning of the coupling when $N > 0$ and $\vartheta = -\pi$:

$$\Delta\omega_s = \partial_t \varphi_s = \Lambda E_{p0}^2 \frac{\left(t - \frac{|x|}{v_g}\right)^2}{2} > 0 \quad (2.30)$$

where E_{p0} is the initial value of the electric field amplitude of the pump. The seed is then downshifted with respect its initial value as a function of time. ***During this transient regime, almost only the seed phase φ_s is varying and the total phase variation ϑ is determined by $-\varphi_s$.*** Fig.(2.2(a)) To study the behavior of the seed phase given by Eq.(2.19) and its evolution we make a second change of frame of reference:

$$\begin{aligned} y &= \hat{x} + |v_g| t \\ \tau &= t \end{aligned}$$

This allows one to follow a particular point on the seed pulse along the entire amplification process. In this new reference, Eq.(2.19) become:

$$\partial_\tau \varphi_s(y, \tau) = -\mu \frac{N E_{p0}}{E_{s0}} \cos \vartheta \quad (2.31)$$

where E_{s0} is the initial value of the electric field amplitude of the pump. Using the same change of variables, Eq.(2.28) can be written as:

$$N(y, \tau) = \begin{cases} -\Lambda E_{p0} E_{s0} \frac{\left(2\tau - \frac{y}{v_g}\right)^2}{2} & \text{if } x > 0 \rightarrow v_g \tau \leq y \leq 2v_g \tau \\ -\Lambda E_{p0} E_{s0} \frac{\left(\frac{y}{v_g}\right)^2}{2} & \text{if } x < 0 \rightarrow 0 \leq y \leq v_g \tau \end{cases} \quad (2.32)$$

If we consider a point on the seed pulse for which $\hat{x} > 0$ at a given time τ , it means that the point is at the right of the crossing point $\hat{x} = 0$. In this case the seed phase is varying as:

$$\varphi_s(y, \tau) = \mu \frac{E_p}{E_s} \int_{y/2v_g}^{\tau} \left(-\Lambda E_p E_s \frac{\left(2\tau - \frac{y}{v_g}\right)^2}{2} \right) d\tau = \frac{1}{12} \mu \Lambda E_p^2 \left(2\tau - \frac{y}{v_g}\right)^3 = \frac{2}{9\sqrt{3}} \gamma_{sc}^3 \left(2\tau - \frac{y}{v_g}\right)^3 \quad (2.33)$$

Otherwise if a point on the seed is at $\hat{x} < 0$ at a given time τ , it means that the point travelled from $\hat{x} > 0$ to $\hat{x} < 0$; thus the seed phase can be expressed as:

$$\varphi_s(y, \tau) = \mu \frac{E_p}{E_s} \left(\int_{y/2v_g}^{y/v_g} \left(-\Lambda E_p E_s \frac{\left(2\tau - \frac{y}{v_g}\right)^2}{2} \right) d\tau + \int_{y/v_g}^{\tau} \left(-\Lambda E_p E_s \frac{\left(\frac{y}{v_g}\right)^2}{2} \right) d\tau \right) = \frac{1}{12} \mu \Lambda E_p^2 \left(\frac{y}{v_g}\right)^2 \left(6\tau - 5\frac{y}{v_g}\right) = \frac{2}{9\sqrt{3}} \gamma_{sc}^3 \left(\frac{y}{v_g}\right)^2 \left(6\tau - 5\frac{y}{v_g}\right) \quad (2.34)$$

The results on the evolution of the seed phase can be resumed, in units of x and t , as following:

$$\varphi_s(\hat{x}, t) = \begin{cases} \frac{2}{9\sqrt{3}} \gamma_{sc}^3 \left(t - \frac{\hat{x}}{v_g}\right)^3 & \text{if } \hat{x} > 0 \\ \frac{2}{9\sqrt{3}} \gamma_{sc}^3 t^3 & \text{if } \hat{x} = 0 \\ \frac{2}{9\sqrt{3}} \gamma_{sc}^3 \left(t + \frac{\hat{x}}{v_g}\right)^2 \left(t - 5\frac{\hat{x}}{v_g}\right) & \text{if } \hat{x} < 0 \end{cases} \quad (2.35)$$

In Fig.(2.3) we show the comparison between the theoretical estimation of the phase of the seed (φ_s^{th} , red line) and the results from simulation (φ_s , green line), for $0 < t\gamma_{sc} < 2$: the estimation of Eq.(2.35) is reproducing quite well the results from simulations. Notice that in Fig.(2.3) the theoretical estimation of the phase of the seed (φ_s^{th} , red line) has been shifted in time of $t\gamma_{sc} \approx 0.11$ corresponding to the time ramp of the seed. For $\hat{x} = 0$ the total phase ϑ is:

$$\vartheta(\hat{x} = 0, t) = -\pi - \frac{2}{9\sqrt{3}}\gamma_{sc}^3 t^3 \quad (2.36)$$

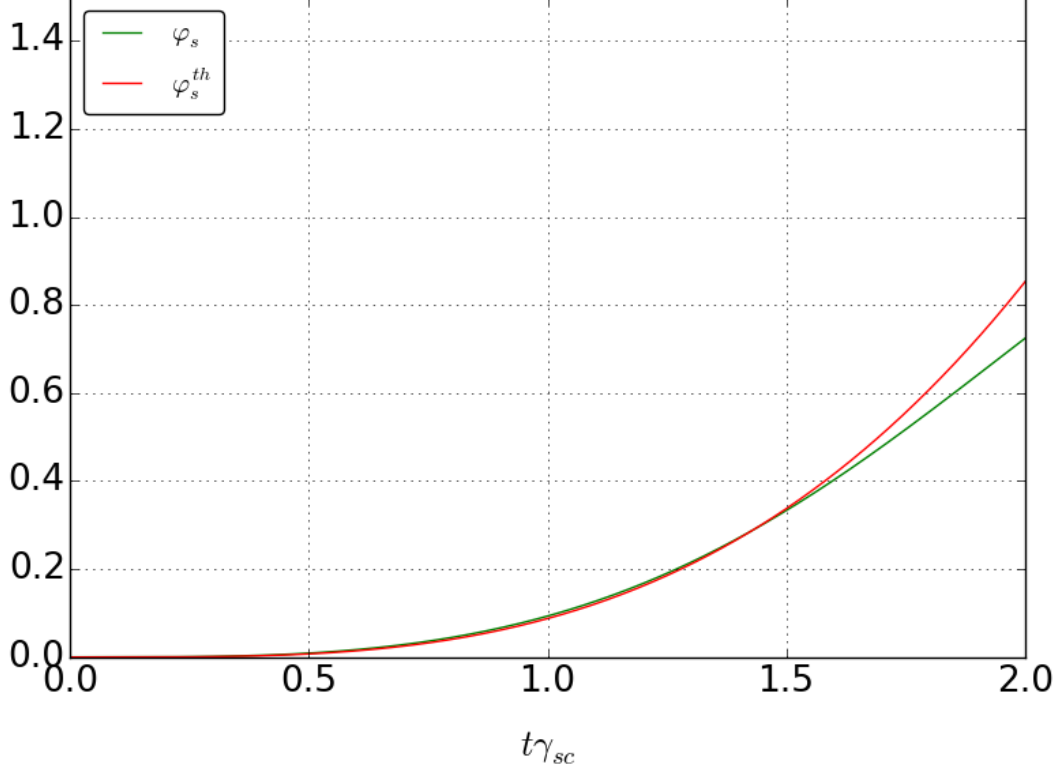


Figure 2.3: Seed phase at the lasers crossing point $\hat{x} = 0$ and in function of time ($0 < t\gamma_{sc} < 2$: comparison between the results of φ_s from simulations (green line) and from the expression given in Eq.(2.35) (red line).

The evolution of the density perturbation phase φ for this initial interaction stage can be calculated . We consider Eq.(2.21) neglecting the terms multiplied by c_s :

$$\partial_t \varphi = -\frac{\Lambda E_p E_s \sin \vartheta}{2\partial_t N} \quad (2.37)$$

If $\vartheta \approx \pi - \varphi_s$ and $\partial_t N = -\Lambda E_p E_s (\cos \vartheta)t$, we obtain:

$$\partial_t \varphi = \frac{1}{2} \frac{\tan \vartheta}{t} = -\frac{1}{2} \frac{\tan \varphi_s}{t} \quad (2.38)$$

and, making the hypothesis that $\tan \varphi_s \approx \varphi_s$, we can write:

$$\partial_t \varphi \approx -\frac{1}{2} \frac{\varphi_s}{t} \quad (2.39)$$

As, from Eq.(2.35), φ_s has a different expression if $\hat{x} > 0$ or $\hat{x} < 0$, we can obtain:

$$\varphi(\hat{x}, t) = \begin{cases} \frac{\sqrt{3}}{27}\gamma_{sc}^3 \left[\frac{t^3}{3} - \frac{3}{2}\frac{\hat{x}}{v_g}t^2 - 3\left(\frac{\hat{x}}{v_g}\right)^2 t + \frac{25}{6}\left(\frac{\hat{x}}{v_g}\right)^3 - \left(\frac{\hat{x}}{v_g}\right)^3 \ln t \right] & \text{if } \hat{x} > 0 \\ \frac{1}{6}\varphi_s(0, t) & \text{if } \hat{x} = 0 \\ \frac{\sqrt{3}}{27}\gamma_{sc}^3 \left[\frac{t^3}{3} - \frac{3}{2}\frac{\hat{x}}{v_g}t^2 - 9\left(\frac{\hat{x}}{v_g}\right)^2 t + \frac{43}{6}\left(\frac{\hat{x}}{v_g}\right)^3 - 5\left(\frac{\hat{x}}{v_g}\right)^3 \ln t \right] & \text{if } \hat{x} < 0 \end{cases} \quad (2.40)$$

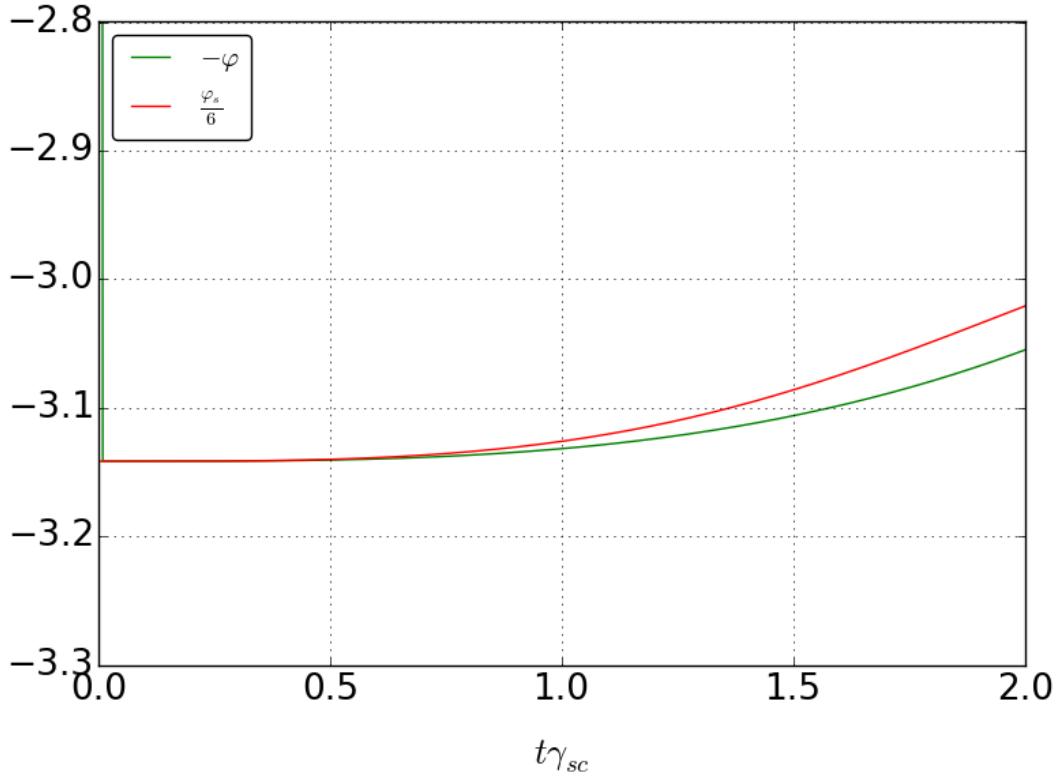


Figure 2.4: Comparison between the simulation results for the evolution of the plasma density perturbation phase (green line, $-\varphi$) and the estimation given by Eq.(2.40) (red line, $\varphi_s/6$), at $\hat{x} = 0$ and for $0 < t\gamma_{sc} < 2$.

In Fig.(2.4) we show the agreement between the simulation results for the evolution of the plasma density φ (green line, $-\varphi$) and the estimation given by Eq.(2.40) (red line, $\varphi_s/6$), at $\hat{x} = 0$ and for $0 < t\gamma_{sc} < 2$. This result confirms that before the exponential regime φ is negligible.

Eq.(2.28) and (2.35) are valid up to when the exponential growth regime [24] will take place for the seed and the density perturbation as derived in Eq.(1.53). Comparing with Fig.(2.2), the discussion confirms that on value and evolution of the seed phase

φ_s given by Eq.(2.35) is valid for $0 < t\gamma_{sc} < 2$. For later time, $2 < t\gamma_{sc} < 4.3$ (dashed region in Fig.(2.2)), the seed enters the so-called "linear regime" (where pump depletion is neglected but both seed and plasma density perturbations grow exponentially) that will be discussed in detail in the next section. In this limit, that has been largely studied in the past, the downshift of the seed is a constant, given by the real part of Eq.(1.53), while the density fluctuations oscillate at the same frequency. Thus in this part the phases of the seed and density fluctuations are of the same order and compensating each other, still with $\phi_p \approx 0$. As the intensity of the seed grows and becomes larger than the pump one, the energy transfer changes direction (blue regions in Fig.(2.2), for $t\gamma_{sc} > 4.67$). This doesn't happen instantly and the temporal spread of the seed is determined by the time needed by the phases to adapt as will be detailed in the following. To resume, in this section we showed that the energy transfer direction is dictated by the evolution of the phases: in particular, as long the electric field amplitude of the pump is more important than the seed one, the phase of the ion-acoustic wave imposes that the pump amplify the seed. We also showed that the phases need a certain time to adapt before entering the linear regime of amplification: during this transient regime (of the order of $t\gamma_{sc} \approx 2$, Fig.(2.2)(a)) the variation of the total phase ϑ is determined by the seed phase φ_s . In the following section we show the phases behavior during the so-called linear regime of amplification.

2.3.2 Exponential growth - 'Linear' phase

After the transient growth and while the pump amplitude (and the corresponding phase) can be considered roughly constant, as mentioned above the seed amplitude and density perturbation enter the standard exponential phase [24][29]. Consistent with recent literature on the subject [24][27][30] we call this phase the linear phase, that is thus defined by the fact that pump depletion is negligible, and the pump and seed exhibit exponential growth. Then we have $\phi_p \approx 0$, $N \propto e^{-i\omega_{sc}t}$ et $E_s \propto e^{i\omega_{sc}t}$.

The seed phase φ_s evolves as:

$$\varphi_s = \gamma_{sc}/\sqrt{3} \cdot t + \varphi_{s0} \quad (2.41)$$

and the density perturbation phase:

$$\varphi = -\gamma_{sc}/\sqrt{3} \cdot t + \varphi_0. \quad (2.42)$$

and the total phase ϑ is roughly constant. From Eq.(2.18) and Eq.(2.19), making the hypothesis that the seed amplitude E_s and the density perturbation N are evolving with $e^{\gamma_{sc}t}$, and using Eq. (2.41) it is possible to evaluate the constant value of the total

phase, $\tan(\vartheta) = -\sqrt{3}$ and:

$$\vartheta = -\frac{4}{3}\pi \quad (2.43)$$

This is confirmed by simulations as can be seen in seen in Fig.(2.2)(a) (where $\vartheta \approx$ constant) and Fig.(2.2)(c) where the electric field amplitude of the seed is growing exponentially for $2 < t\gamma_{sc} < 4.3$. We are now in a position to estimate the necessary time t_i since the beginning of the coupling to reach the exponential amplification phase. This is the time for ϑ as given by Eq. (2.35) to be of the order of $-4\pi/3$, that is for $\varphi_s = \frac{2}{9\sqrt{3}}\gamma_{sc}^3 t^3 \sim \pi/3$:

$$t_i = \left(\frac{4\pi}{\mu\Lambda E_{p0}^2} \right)^{1/3} \approx \frac{2}{\gamma_{sc}}. \quad (2.44)$$

The estimation of t_i is confirmed by numerical simulations: in Fig.(2.2)(c) we can see that the seed electric field amplitude start to grow at $t\gamma_{sc} \approx 2$. The value of density perturbation at $t = t_i$ is obtained by considering (from Eq.(2.28) $N(x = 0, t) = \Lambda E_{p0} E_{s0} t_i^2 / 2$:

$$N(x = 0, t_i) = \Lambda E_{p0} E_{s0} \left(\frac{4\pi}{\mu\Lambda E_{p0}^2} \right)^{2/3} \approx 3.8 \frac{\gamma_{sc}}{\mu} \sqrt{\frac{I_{s0}}{I_{p0}}}, \quad (2.45)$$

where I_{s0} and I_{p0} are the initial intensities of the seed and pump respectively.

To summarize, in this section we showed that during the exponential regime of amplification of the seed, the global phase is almost constant and $\vartheta = -\frac{4}{3}\pi$. The necessary time to reach the exponential regime ($t\gamma_{sc} \approx 2$ for our values of pump intensity and plasma density) has been estimated considering that, during the initial transient regime, only the seed phase is varying. The time during which the exponential regime holds until pump depletion starts and the solution enters the self-similar will be calculated in the following section.

2.3.3 Pump depletion and growth saturation

The duration of the exponential regime is limited by the pump depletion that starts to play a role when the seed amplitude is comparable with the pump one. This time can be evaluated making the hypothesis that $E_s \approx E_{p0}$ at the end of the exponential regime, with E_{s0} indicating the initial value of the seed amplitude:

$$t_{depl} = \frac{1}{\gamma_{sc}} \log \frac{E_{p0}}{E_{s0}} = \frac{1}{2} \frac{1}{\gamma_{sc}} \log \frac{I_{p0}}{I_{s0}} = \frac{1.15}{\gamma_{sc}} \log_{10} \frac{I_{p0}}{I_{s0}}. \quad (2.46)$$

The total time, since the beginning of the coupling to reach the pump depletion

can be now calculated

$$t_{tot} = \frac{1}{\gamma_{sc}} (2 + 1.15 \log_{10} \frac{I_{p0}}{I_{s0}}) \quad (2.47)$$

With the intensities and plasma density values considered, $t_{tot} \approx \frac{4.3}{\gamma_{sc}}$. Comparing with Fig.(2.2)(c), we can see that the estimation made for t_{tot} (right side of the shadowed region) is quite accurate, even if the total phase ϑ shown in Fig.(2.2)(b) has not reached yet $-\pi$, value at which the energy transfer direction flips. To have a better estimation of the time at which $\vartheta = -\pi$ we study the evolution of the electric field amplitude and phase of the pump, since in this stage the phase of the pump is affected (Fig.(2.2)(a)). During the exponential regime, the total phase ϑ is given by Eq.(2.43). From Eq.(2.16), if $\vartheta = -4/3\pi$, supposing $N \propto e^{\gamma_{sc}t}$ and $E_s \propto e^{\gamma_{sc}t}$ and using the value of $N(\hat{x} = 0, t = t_i)$ calculated at the beginning of the exponential regime Eq.(2.45), we obtain:

$$E_p(t) = E_{p0} \left[1 - \frac{\sqrt{3}}{2} \frac{I_{s0}}{I_{p0}} e^{2\gamma_{sc}t} \right] \quad (2.48)$$

where E_{p0} , I_{s0} and I_{p0} are the initial values of amplitude of the pump, intensity of the seed and of the pump, respectively. Notice that, in Eq.(2.48) we didn't include the space derivative $\frac{\partial E_p}{\partial x}$ of Eq.(2.16) as it is negligible in the limit of the approximation used in the estimation.

From Eq.2.17, with the same hypothesis, we obtain the equation for the evolution of the pump phase φ_p :

$$\partial\varphi_p = \partial \left(\varphi_p - \frac{4\pi}{3} \right) = -\frac{NE_{s0}e^{2\gamma_{sc}t}}{E_{p0}} \cos \left(\varphi_p - \frac{4\pi}{3} \right). \quad (2.49)$$

Integrating the previous equation leads to :

$$\sin \left(\varphi_p - \frac{4\pi}{3} \right) = \frac{-1 + Ae^{-\beta(e^{2\gamma_{sc}t}-1)}}{1 + Ae^{-\beta(e^{2\gamma_{sc}t}-1)}}, \quad (2.50)$$

where $A = (1 - \sin 4\pi/3)/(1 + \sin 4\pi/3) = 7 + 4\sqrt{3} \approx 14$ and $\beta = NE_{s0}/(E_{p0}\gamma_{sc})$.

We can develop Eq. 2.50 making the hypothesis that the term $\beta(e^{2\gamma_{sc}t} - 1) \ll 1$ and we obtain $\sin(\varphi_p - \frac{4\pi}{3}) = \frac{\sqrt{3}}{2} - \frac{1}{8}\beta(e^{2\gamma_{sc}t} - 1)$.

For $\varphi_p < 1$ we obtain:

$$\varphi_p = \frac{\beta}{4} (e^{2\gamma_{sc}t} - 1) = \frac{1}{4} \cdot \frac{NE_{s0}}{E_{p0}\gamma_{sc}} (e^{2\gamma_{sc}t} - 1). \quad (2.51)$$

Consistent with Fig.(2.2)(a) we find that the phase of the pump starts to grow when depletion starts to set in, at $t > t_{tot}$. If we substitute the value of density perturbation

at the beginning of the exponential regime, as given by Eq.2.45, we find a simpler expression:

$$\varphi_p \approx \frac{1}{2} \frac{I_{s0}}{I_{p0}} (e^{2\gamma_{sc}t} - 1) \quad (2.52)$$

We are now in a position to estimate at which time the pump will stop to transferring energy to the seed. The characteristic time necessary to let the global phase ϑ to vary from $-4\pi/3$ to $-\pi$ (value at which the coupling is zero) is given by the variation of φ_p (as expressed in the equation above) of $\pi/3$. As we can see in the simulations (Fig.(2.2)) and as expected $|\vartheta|$ keeps diminishing and when $\vartheta = -\pi + \epsilon$ the direction of the flow reverses from the pump to the seed, leading to the oscillation behind the first peak, that are the analogous of the π -pulse for the weak coupling regime. Imposing $\varphi_p \approx \pi/3$ in Eq.(2.52) we find:

$$t_{\varphi_p} \approx \frac{1}{2\gamma_{sc}} \log \left(\frac{2\pi}{3} \frac{I_p}{I_s} \right) \quad (2.53)$$

This allows one to evaluate the total time (since the begin of the coupling) at which the electric field reach its maximum: at that time the pump stops to give energy to seed.

$$t_{E_{smax}} \gamma_{sc} \approx t_i + t_{\varphi_p} = 2 + 2.67 = 4.67 \quad (2.54)$$

In Fig.(2.2) $t_{E_{smax}}$ is indicated by the black dashed-dotted vertical line. As we can see the estimation given by Eq.(2.54) is very accurate: at $t\gamma_{sc} = 4.67$ the total phase is $\vartheta = -\pi/2$ (Fig.(2.2)(b)) and the first peak of the amplified seed reaches its maximum (Fig.(2.2)(c)). For $t\gamma_{sc} > t_{E_{smax}}$ the seed amplitude starts to decrease and the pump is amplified. At later time, the process is inverted again (dotted black line) and a new small peak of the seed starts to be amplified.

2.4 Conclusions

In this chapter we showed the importance of the time evolution of the phases of pump, seed lasers and density perturbation in the determination of the directionality of the energy transfer. In particular, developing the system of equations describing the SBS amplification in terms of amplitudes and the phases, we can make a complete description of the different stages of amplification. In the case of the amplification of a laser beam in the weak coupling regime, we found that the total phase (expressed as combination of the phases of the pump, seed and density perturbation) stays constant: when $\vartheta = \pi/2$ the seed is amplified by the pump. As the pump amplitude decreases and eventually goes to zero, the global phase flips to $\vartheta = -\pi/2$ and the energy transfer

change direction, from the seed to the pump.

In the strong-coupling regime the situation is more complicated as the total phase is continuously time-dependant. The energy transfer direction is dictated by the evolution of the phases: as long as the electric field amplitude of the pump is more important than the seed one, the pump gives energy to the seed. During the very first moments of the coupling (of the order of $\approx 2\gamma_{sc}$ for the values of pump intensity and plasma density considered in this chapter), almost only the seed phase φ_s is varying and the total phase variation is determined by the seed. When later in time the seed enters the exponential regime of amplification, known as "linear regime", the seed and density perturbation phases start to compensate each other (letting the pump phase unchanged and equal to zero), resulting in a constant value of the total phase, $\vartheta = -\frac{4}{3}\pi$. As soon as the amplified seed intensity is comparable with the pump one (at $t\gamma_{sc} \approx 4.3$ in our simulations and estimations), the total phase starts to evolve again from $\vartheta = -\frac{4}{3}\pi$ to $\vartheta = -\pi$. This transient is driven by the pump phase φ_p that is varying with time: when $\varphi_p = \frac{\pi}{3}$ (at $t\gamma_{sc} \approx 4.67$) the total phase reaches $\vartheta = -\pi$, value at which the energy transfer is inverted. At this moment, the first peak of the amplified seed is formed and the seed starts to give energy to the pump. The total phase is then oscillating around $\vartheta = -\pi + \epsilon$, leading to the oscillation behind the first peak of the seed that are analogous of the π -pulse for the weak coupling regime. To conclude, we showed that the global phase ϑ is the relevant quantity that determines the efficiency of the coupling and of the amplification.

Chapter 3

Intrinsic frequency chirp in the strong coupling regime for SBS

In Sec 2.3 we analyzed the different phases of amplification of a constant seed laser by a constant pump. As already mentioned in many experimental situations of interest the pump will be chirped, where the effect of the chirp can be considered as a time varying phase ϕ , as in Eq. (1.55) or analogously as a varying frequency, where the global frequency is given by $\omega(t) = \omega_0 - \partial\phi/\partial t$. From the previous analysis it is clear that time dependent variations in the phase can affect the coupling. In particular if the de-phasing is too large the coupling will be quenched, while an optimal condition can be found if the chirp can be used to maintain a favorable coupling in the maximum seed growth, and pump depletion phase. In order to fulfill this condition, the parameter that needs to be taken into account is the sign of the chirp parameter α . We will perform the study still in the framework of a local analysis, at a given point in space, as it allows useful estimations of the optimal value of α . However, with very large values of the chirp parameter, we can indeed quench the amplification. Once identified the criterion of optimal coupling, we can calculate the value of chirp and delay for the optimal amplification, as well as the order of magnitude of the α parameter in the definition of the chirp for which amplification still happens. We point out however that as long as α is not too large, amplification is still efficient even if we do not consider the optimal case. This is because in the strong coupling regime there is an intrinsic width in the coupling, and the phase evolves with time over a relatively large range. The chapter is organized as following: in Sec.3.1 we identify two values of the chirp parameter α that compensate the seed phase evolution at two different stages of the amplification. We show that the efficiency of the seed amplification is slightly improved when α is negative and of the order of $\alpha \approx -10^{-7}$ for the parameters considered in this work. When $\alpha > 0$ or is too large ($|\alpha| > 10^{-6}$) the amplification process is quenched and

the seed phase does not manage to evolve and adapt to allow the coupling. In section 3.2 we investigate the role played by an inhomogeneous plasma density profile on the evolution of the amplification of the seed. In particular, we show that a linear plasma density profile with the maximum shifted towards right is more favorable comparable to a case with a linear plasma density profile with the maximum shifted towards left for a pump propagating to the right and a seed to the left. This case is still more favorable when the comparison is made with a case in which we consider a constant plasma density profile with a density equal to the average value of the inhomogeneous cases. Contrary to SRS-based amplification, sc-SBS requires a preferential gradient of the plasma profile with respect to the pump propagation direction. To have an order of magnitude of the effect a density gradient, we define an effective pump chirp associated with the density gradient.

3.1 Effect of the chirp on the coupling

In this section we make an estimation of the possible values of the chirp parameter α that can enhance or quench the seed amplification. The equation that we consider and solve are unchanged, apart from the presence of a chirp in the definition of the total phase $\vartheta = \varphi_p + \phi - \varphi_s - \varphi$. The effect of this chirp is such that an optimal value can improve the efficiency of the coupling, while a large chirp compensating the initial value of the seed phase will quench the seed amplification. For a first analysis and a first set of simulations, we make the hypothesis that the chirp function is centered at $x_0 = 350 \mu m$, where the pump and seed crosses, and $t_0 = 0$ (chapter 1). The values of pump and seed intensity and plasma density are the same than the ones in Sec 2.3, namely $I_p = 10^{15} W/cm^2$, $I_s = 10^{13} W/cm^2$ and $n/n_c = 0.1$. In Fig.(3.1(a)) we show the evolution of the seed phase φ_s as a function of time up to the time when the seed reaches its maximum and pump depletion sets in. As shown in the figure and discussed in Sec 2.3, at the beginning of the interaction, for $t < t_i$, almost only the seed phase φ_s is varying.

In order to find an optimal value of the chirp parameter, we consider the phases evolution in the exponential stage. When the coupling enters in this stage, the phase of the seed and the density are of the same order, while the the phase of the pump is still negligible until pump depletion starts ($t = t_{tot}$). In these conditions the seed becomes downshifted with respect to the pump. In this stage we can consider mainly how the presence of the chirp affects the total phase by compensating the seed phase. If the chirp is such that the pump phase time derivative for $t_i < t < t_{tot}$ ($2 < t\gamma_{sc} < 4.3$ in our simulations) corresponds to a frequency upshift and it is almost exactly equal to the seed phase derivative when pump depletion starts, the seed phase will stay close to its

value in the exponential regime, and an optimal coupling is achieved. Notice that since the time evolution of the phase associated to the chirp and associated to the coupling are not the same, it is not evident a priori at what time the chirp has to compensate for the seed and the choice we made is based on analysis of the simulations.

The expression of the seed phase evolution for $t_i < t < t_{tot}$ for $t_i \approx 2/\gamma_{sc}$ and $t = t_{tot} \approx 4.3/\gamma_{sc}$ is:

$$\varphi_s(t) = \frac{\gamma_{sc}(t - t_i)}{\sqrt{3}} + \varphi_s(t = t_i) = \frac{\gamma_{sc}(t - t_i)}{\sqrt{3}} + \frac{\pi}{3} \quad (3.1)$$

As we pointed out before, a criteria to obtain an optimal coupling can be to impose that the seed phase time derivative is equal to the chirp one at $t = t_{tot}$, so that $\partial_t \varphi_s(t_{tot}) = \partial_t \phi(t_{tot})$:

$$\gamma_{sc}/\sqrt{3} = 2|\alpha|\omega_0^2 t_{tot} \quad (3.2)$$

If α is negative, with our choice of x_0 and t_0 this corresponds to a negative phase for the pump, and a frequency upshift. From Eq.(3.2), this gives a condition for the optimal α , with $\alpha < 0$:

$$\alpha_{tot} \approx -\frac{1}{2\sqrt{3}} \frac{\gamma_{sc}^2}{\omega_{0p}^2} \frac{1}{2 + 1.15 \log_{10} \frac{I_{p0}}{I_{s0}}}. \quad (3.3)$$

If we consider the parameter of the simulations $n/n_c = 0.1$ and a pump $I_p = 10^{15} W/cm^2$, we find $\gamma_{sc}^2/\omega_{0p}^2 \approx 5 \cdot 10^{-6}$ and the optimal coupling is given by $\alpha_{tot} \approx -3.3 \times 10^{-7}$. This approach is shown in Fig.(3.1(c)): the green line indicates the evolution of the phase of the seed $-\varphi_s$ for $t_i \gamma_{sc} = 2 < t \gamma_{sc} < t_{tot} \gamma_{sc} = 4.3$, the black line $-\varphi_s^{th}$ is the approximation of the seed phase considered in Eq.(3.1) and the blue line is the phase of the chirp calculated with α_{tot} . Fig.(3.1(d)) shows the evolution of the time derivative of the seed phase $\partial_t(-\varphi_s)$ (green dashed line), of the theoretical value $\partial_t(-\varphi_s^{th}) = \gamma_{sc}/3$ (black dashed line) and the time derivative of the chirp phase $\partial_t \phi(\alpha_{tot})$ (blue dashed line), for $t_i \gamma_{sc} = 2 < t \gamma_{sc} < t_{tot} \gamma_{sc}$; Eq.(3.2) dictates that $\partial_t \phi(\alpha_{tot})$ and $\partial_t(-\varphi_s)$ are crossing at $t \gamma_{sc} = 4.3$.

As we will show in the following (Table 3.1), the amplification is generally improved if the chirp parameter is small, $\alpha \approx -10^{-7}$, but in terms of energy exchange the choice of α_{tot} allows a slightly better energy exchange between the pump and the seed.

A comparison of the amplification process in simulations for a non-chirped case $\alpha = 0$ and for the optimal case $\alpha = \alpha_{tot}$ is reproduced in Fig.(3.2) as function of time and Fig.(3.3) as function of space. Notice that with the optimal value of chirp the global phase (Fig.(3.2)(d),dashed black line) corresponding to the first peak is very close to $-3\pi/2$, and when there is reverse of energy flow, it almost suddenly jumps to $\pi/2$, with a behavior that is much closer to pi-pulse for weak coupling than without chirp (Fig.(3.2)(d), black solid line). Similarly for this case with optimal chirp, the

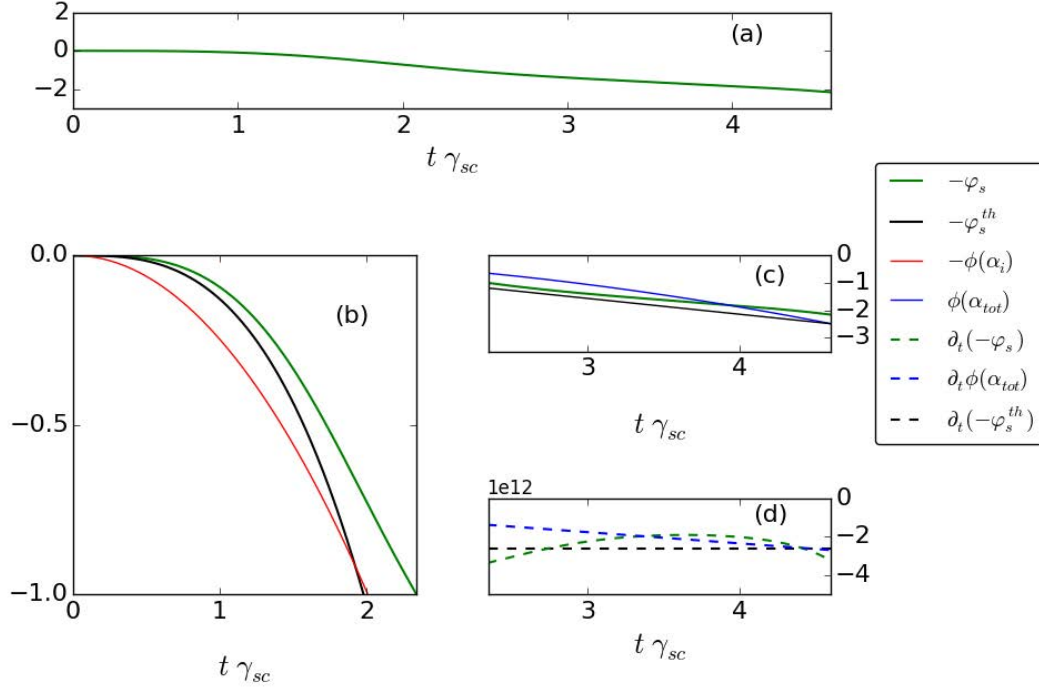


Figure 3.1: a) Evolution of seed phase $-\varphi_s$ for $0 < t\gamma_{sc} < t_{tot}\gamma_{sc}$, with $t_i\gamma_{sc} = 2$ and $t_{tot}\gamma_{sc} = 4.3$. b) Comparison among $-\varphi_s$ (green line), $-\varphi_s^{th} = \frac{2}{9\sqrt{3}}\gamma_{sc}^3 t^3$ as calculated in Eq.(2.35) (black line) and the chirp phase $-\phi(\alpha_i)$ calculated in Eq.(3.5) $\alpha_i = 1.28 \times 10^{-6}$ (red line), for $0 < t\gamma_{sc} < t_i\gamma_{sc}$. c) Comparison among $-\varphi_s$ (green line), $-\varphi_s^{th}$ as given by Eq.(3.1) (black line) and the chirp phase $\phi(\alpha_{tot})$ calculated in $\alpha_{tot} = -3.3 \times 10^{-7}$ (blue line), for $t_i\gamma_{sc} < t\gamma_{sc} < t_{tot}\gamma_{sc}$. d) Evolution of the seed frequency $\partial_t(-\varphi_s)$ (green dashed line) compared to the theoretical value $\partial_t^{th}(-\varphi_s) = \gamma_{sc}/\sqrt{3}$ (black dashed line) and the frequency variation due to the chirp $\partial_t\phi(\alpha_{tot})$ (blue dashed line). All the results shown here are calculated at the initial laser crossing point ($x = 350\mu m$).

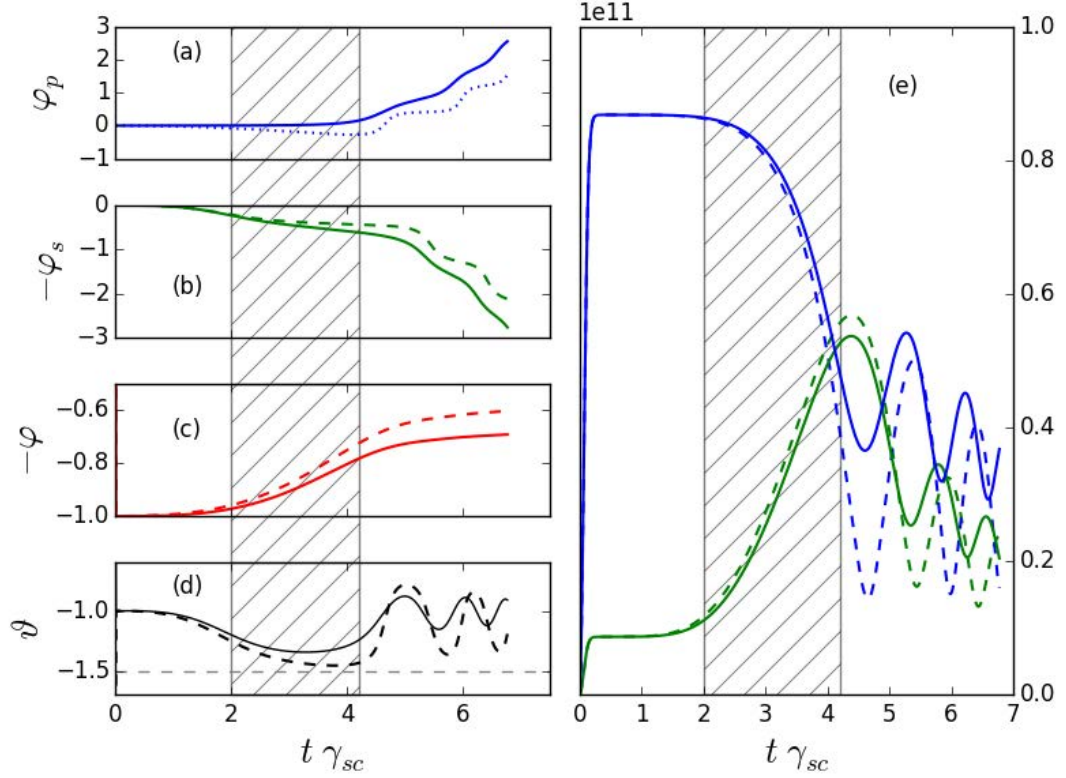


Figure 3.2: Evolution in time of the phases of the pump (a) (φ_p), of the seed (b) ($-\varphi_s$), of the density perturbation (c) ($-\varphi$) and of the total phase (d) ϑ in function of time and in units of π , at $x = 350\mu m$. e) Electric fields amplitudes, in V/m , of the pump (blue lines) and of the seed (green lines) in function of time. The solid lines indicate the simulation results for $\alpha = 0$, the dashed ones are for $\alpha = \alpha_{tot}$. The shadowed region indicates the time interval in which the seed is exponentially amplified.

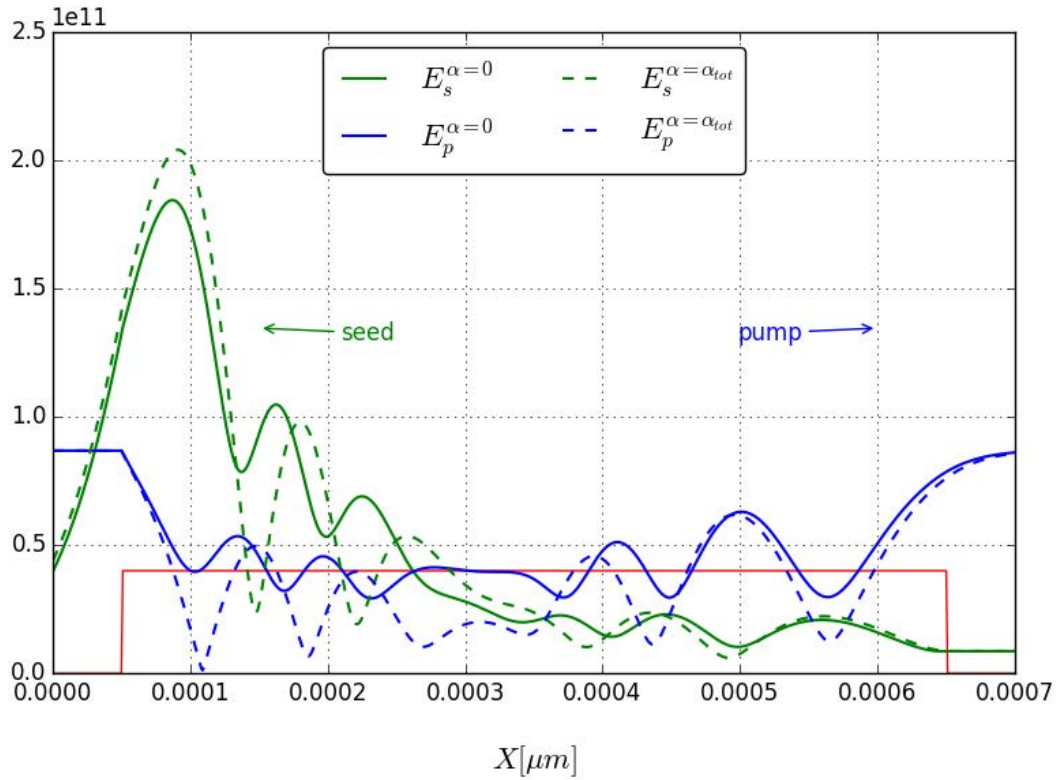


Figure 3.3: Electric fields amplitudes, in V/m , of the pump (blue lines) and of the seed (green lines) in function space, at $t = 1.5$ ps. The solid lines indicate the simulation results for $\alpha = 0$, the dashed ones are for $\alpha = \alpha_{tot}$

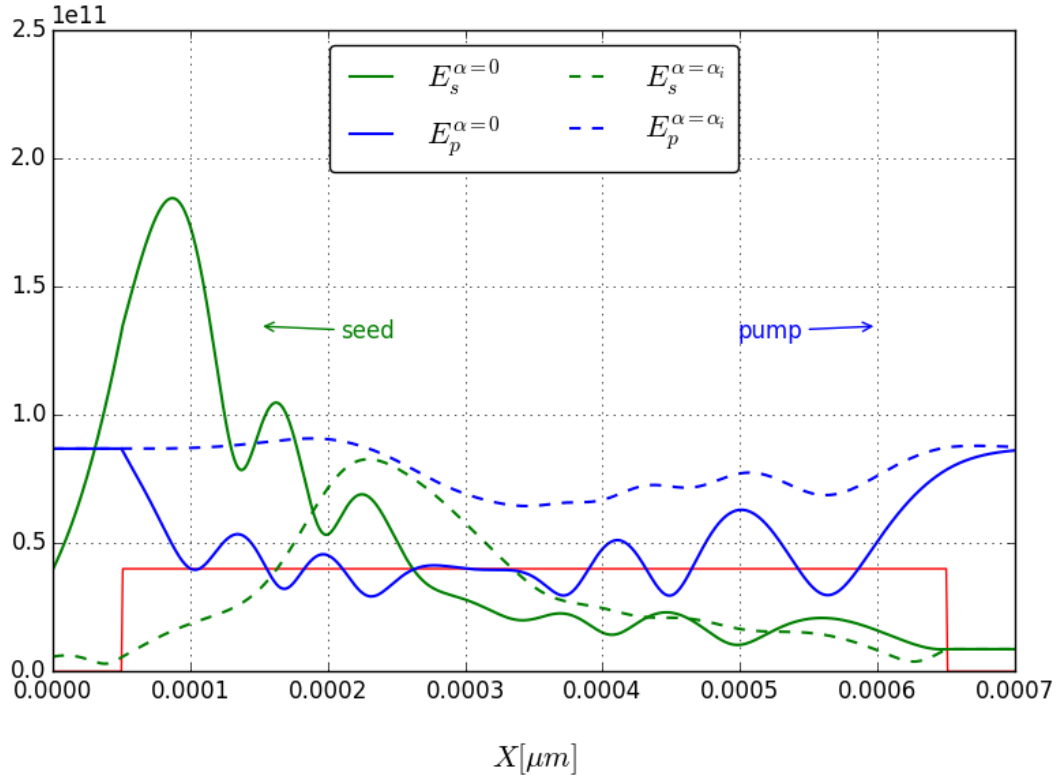


Figure 3.4: Electric fields amplitudes, in V/m , of the pump (blue lines) and of the seed (green lines) in function space, at $t = 1.5$ ps.

The solid lines indicate the simulation results for $\alpha = 0$, the dashed ones are for $\alpha = \alpha_i$: in this case the amplification of the seed with a chirped pump laser is strongly quenched.

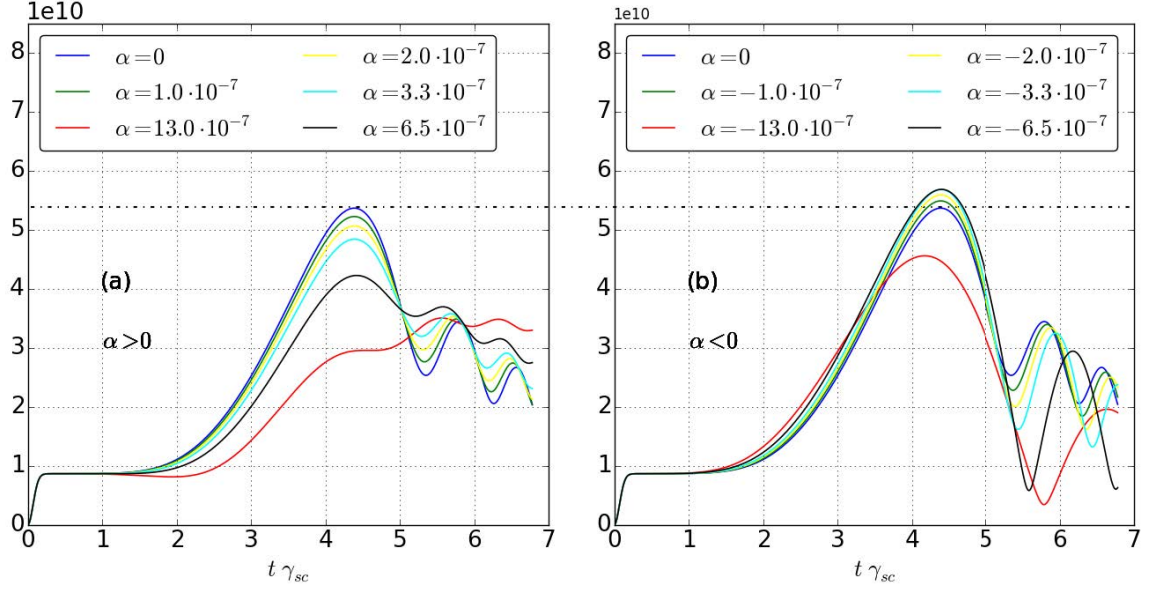


Figure 3.5: Evolution of the electric field amplitude of the seed in function of time at the initial crossing point of the lasers ($x = 350 \mu\text{m}$) and for positive (a) and negative (b) values of α . The dashed black line indicates the maximum electric field amplitude for $\alpha = 0$.

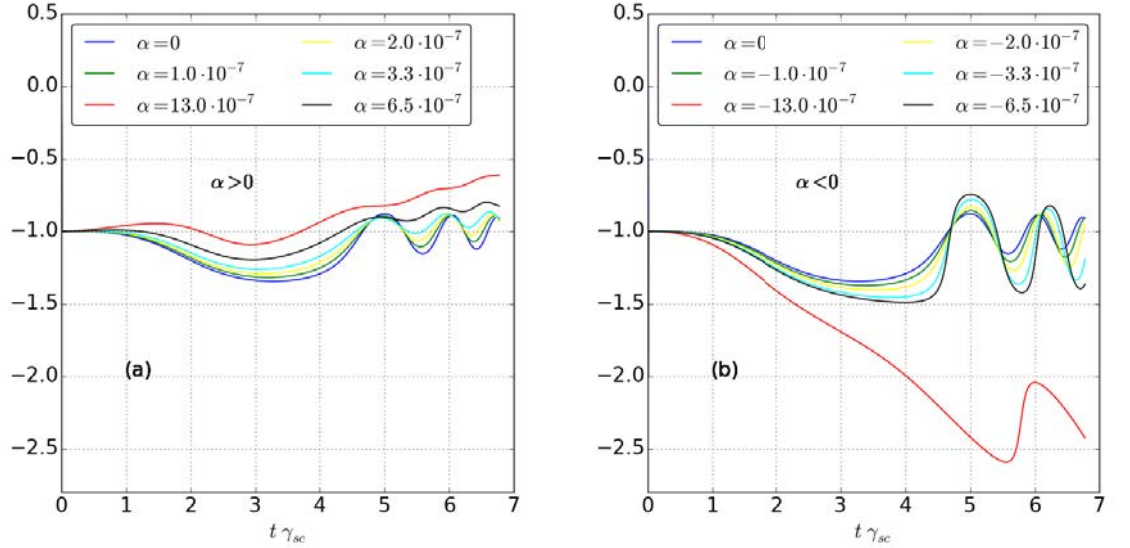


Figure 3.6: Evolution of the total phase ϑ (in units of π) as function of time at the initial crossing point of the lasers ($x = 350 \mu\text{m}$) and for positive (a) and negative (b) values of α .

first peak is the one with highest intensity and the field goes almost to zero before growing again and forming the next peak (Fig.(3.2)(e),green solid line). The differences between a simulation with $\alpha = 0$ and $\alpha = \alpha_{tot}$ are more important at the end of the amplification, at $t = 1.5$ ps, Fig.(3.5): the final electric field amplitude of the seed for the case of a chirped pump (green and blue dashed line in Fig.(3.3), respectively) is $E_s^{\alpha_{tot}} \approx 2.05 \times 10^{11}$ V/m and the pump amplitude is reaching almost zero when the energy flow direction flips. In Table 3.1 we show the simulation results in terms of final electric field amplitude, final duration and energy exchange as function of different values of the chirp parameter α . FWHM_{out} is the final duration of the higher peak of the amplified seed, Q_{gain} is the energy gain of the amplified seed evaluated on the entire simulation box at the net of the initial seed energy, $Q_{in}^{seed} = 23 \text{ J/cm}^2$. The initial available pump energy and seed electric field amplitude are $Q_{in}^{pump} = 2333 \text{ J/cm}^2$ and $E_{in}^{seed} = 8.67 \times 10^9$ V/m. The seed energy has been evaluated on the entire simulation box; the available pump energy Q_{in}^{pump} has been calculated as two times the energy of the electric field for $0 < x < 350 \text{ } \mu\text{m}$. This is because the pump and seed pulses are counter-propagating and the seed. The most efficient amplification is reached for $\alpha = \alpha_{tot} = -3.3 \times 10^{-7}$, for which the pump transfers almost %67 of its energy to the seed.

If instead the pump laser is chirped in such a way that the variation of phase due to the chirp at the beginning of the interaction is of the same order of φ_s , and α is positive (that is the pump is downshifted with our choice of t_0, x_0) the coupling it's quenched, and the seed phase does not manage to evolve and adapt to allow the coupling. As found in the previous section, without chirp, the initial time evolution of φ_s is $\varphi_s = \frac{2}{9\sqrt{3}}\gamma_{sc}^3 t^3$, for all the initial time, up to $t = t_i \approx 2/\gamma_{sc}$.

On the other hand the chirp as function of time, at given point, can be written (from Eq.(23)) as:

$$\phi = \alpha \omega_0^2 t^2 \quad (3.4)$$

If we now set $\phi \sim \varphi_s$ at t_i we obtain the value of α for which the process is quenched :

$$\alpha_i \approx 0.26 \frac{\gamma_{sc}^2}{\omega_{0p}^2} \quad (3.5)$$

For the parameters of the simulations this corresponds to $\alpha_i = 1.28 \times 10^{-6}$. In Fig.(3.1)(b) we show the evolution of the seed phase $-\varphi_s$ from the simulation results in comparison with the theoretical values $-\varphi_s^{th}$ from Eq.(2.35) and with the chirp phase $-\phi(\alpha_i)$. The determination of α_i (Eq.(3.5)) corresponds to $-\phi(\alpha_i)$ and $-\varphi_s^{th}$ crossing at $t = t_i$. In Fig.(3.4) we show the simulation results for a non-chirped case $\alpha = 0$ (solid lines) and for the case in which the amplification is quenched (dashed lines) $\alpha = \alpha_i$

as function of space: when the pump is chirped with $\alpha = \alpha_i$, the resulting amplified seed is an order of magnitude smaller than the case with $\alpha = 0$. A similar behavior is reproduced also if $\alpha < 0$ and very large, $|\alpha| > 10^{-6}$. In Fig.(3.5) we summarize the results of the evolution of the seed electric field amplitude at $x = 350 \mu\text{m}$ as function of time and for different values of α : in particular, for $\alpha < 0$ (Fig.(3.5)(b)) and $\alpha \approx -10^{-7}$ the values of the electric field amplitude of the first peak are comparable, even if slightly higher, to the simulation with $\alpha = 0$. For values of $\alpha \leq -\alpha_i$ the amplification is mostly quenched, since the phase variation now is too fast. On the other hand, for small positive values of α (Fig.(3.5)(a)) the amplification is a bit smaller compared to the case with $\alpha = 0$, even if still effective; for $\alpha \geq \alpha_i$ the amplification is strongly quenched. These results are confirmed in Table 3.1: for $-1 \cdot 10^{-7} < \alpha < -3.3 \cdot 10^{-7}$ the pump energy transfer is of the same order of magnitude ($\approx 63 - 67\%$ of the available pump energy). For positive values of α the energy transfer diminishes; for large values of α the sign of the chirp parameter does not play a role any more and the amplification is anyway strongly quenched.

In Fig.(3.6) we show the time evolution of the total phase ϑ as function of time and for different values of α : notice that for negative values of the chirp parameter α (Fig.(3.6(b))), the total phase reaches larger negative values during the linear regime of amplification ($2 < t\gamma_{sc} < 4.3$) compared to the case with $\alpha = 0$ ($\vartheta = -4\pi/3$ for $\alpha = 0$ in the linear regime). In particular if $\alpha < 0$ and of the order of the optimal value calculated above $\alpha \approx -10^{-7}$, the total phase approaches a value of the order of $\vartheta \approx -3\pi/2$. On the opposite, if $\alpha > 0$ (Fig.(3.6(a))) the total phase we have always that $\vartheta > -4\pi/3$. For large values of the chirp parameter, $|\alpha| \approx 10^{-6}$, the evolution of ϑ is strongly affected.

In this section we showed how the sc-SBS coupling is affected by the choice of the chirp parameter α . We estimated two values of α that compensate the seed phase evolution at two different stages of the amplification process. ***When α is negative and small*** (of the order $\approx -10^{-7}$), the chirp is such way that the chirp phase compensates the seed phase (corresponding to an upshift of the pump) when pump depletion sets in. In this case ***the coupling is slightly improved compared to the case with $\alpha = 0$*** . If instead the pump is chirped in a way that the chirp phase is equal to the seed phase at the beginning of the coupling, α is positive and large (of the order $\approx 10^{-6}$) and the amplification is strongly quenched. ***For smaller positive values of α , the amplification is slightly quenched compared to the case with $\alpha = 0$*** . ***In a general way, the amplification is slightly affected for small values the chirp parameter α*** . ***On the opposite, for large values of $|\alpha| > 10^{-6}$ the amplification is quenched, even if α is negative***. This is consistent with what found in [31] where they observe that the seed evolution is not symmetric with respect to the sign of the

chirp.

Table 3.1: Overview of the results of the numerical simulations in function of the chirp parameter α . The initial values of electric field for the seed is $E_{in}^{seed} = 8.67 \times 10^9$ V/m; the available pump energy is $Q_{in}^{pump} = 2333$ J/cm². E_{out}^{seed} is expressed in V/m, $FWHM_{out}$ in unit of fs and Q_{gain} in J/cm²

α	E_{out}^{seed}	$FWHM_{out}$	Q_{gain}	%pump
0.0	$1.8 \cdot 10^{11}$	333	1405	60
$-1.0 \cdot 10^{-7}$	$1.95 \cdot 10^{11}$	340	1469	63
$-2.0 \cdot 10^{-7}$	$2.0 \cdot 10^{11}$	338	1525	65
$-3.3 \cdot 10^{-7}$	$2.1 \cdot 10^{11}$	335	1572	67
$-6.5 \cdot 10^{-7}$	$1.8 \cdot 10^{11}$	400	1458	62
$-13.0 \cdot 10^{-7}$	$8.8 \cdot 10^{10}$	600	580	25
$1.0 \cdot 10^{-7}$	$1.78 \cdot 10^{11}$	350	1340	57
$2.0 \cdot 10^{-7}$	$1.6 \cdot 10^{11}$	600	1269	54
$3.3 \cdot 10^{-7}$	$1.4 \cdot 10^{11}$	630	1172	50
$6.5 \cdot 10^{-7}$	$1.1 \cdot 10^{11}$	700	914	39
$13.0 \cdot 10^{-7}$	$8.5 \cdot 10^{10}$	870	396	17

3.2 Influence of the plasma density shape and laser intensity profile on the phase evolution

In this section we investigate the role played by an inhomogeneous plasma density profile on the evolution of the amplification of the seed. This section is organized as following: in subsection 3.2.1 we show that the modification of the pump and seed phases as they are propagating throughout a plasma with a not constant density profile is negligible if there is no coupling. In subsections 3.2.3 and 3.2.4 we study the phase evolution when the amplification happens in presence of triangular density profile and we show how a decreasing triangular plasma density (in the direction of propagation of the seed) improves the amplification. In subsection 3.2.5 we associate the intrinsic frequency chirp for the amplification in an inhomogeneous density profile to a value of the chirp parameter α .

3.2.1 Phase evolution for the propagation of pump and seed lasers without coupling

In this section we explore the phase evolution of the pump and seed in the case they are freely propagating in a linear plasma to asses the importance of the phase velocity variation due to the density gradient. In a general way, the pump and seed electric fields are defined as:

$$\begin{aligned} E_p &\propto \cos(k_p x - \omega_p t) \\ E_s &\propto \cos(-k_s x - \omega_s t) \end{aligned} \quad (3.6)$$

In the case of a constant plasma profile the phases of the pump and seed are respectively:

$$\begin{aligned} \varphi_p &= k_p x - \omega_p t \\ \varphi_s &= -k_s x - \omega_s t \end{aligned} \quad (3.7)$$

At given point x and time t we have:

$$\varphi_p - \varphi_s = (k_p + k_s)x - (\omega_p - \omega_s)t \quad (3.8)$$

If we have $k_p = k_s$, $\omega_p = \omega_s$ and the total phase is:

$$\varphi_p - \varphi_s = 2k_p x = 2\frac{\omega_p}{c} \sqrt{1 - \frac{n}{n_c}} x \quad (3.9)$$

We consider now a plasma with a density that is varying linearly as:

$$\frac{n(x)}{n_c} = \frac{n_{max}}{n_c} \frac{x}{L} \quad (3.10)$$

where n_{max} is the maximum value of plasma density and L is the plasma length; we make the hypothesis that the plasma is limited between the coordinates x_0 and x_1 . At a given point x in the plasma the pump and seed phases read now:

$$\varphi_p = \int_{x_0}^x k_p(x') dx' - \omega_p t \quad (3.11)$$

$$\varphi_s = - \int_{x_1}^x k_s(x') dx' - \omega_s t \quad (3.12)$$

The total phase is then:

$$\varphi_p - \varphi_s = \int_{x_0}^x k_p(x') dx' + \int_{x_1}^x k_s(x') dx' - (\omega_p - \omega_s)t \quad (3.13)$$

If we make the hypothesis that $k_p = k_s$ and $\omega_p = \omega_s$, the total phase is:

$$\varphi_p - \varphi_s = \int_{x_0}^x k_p(x') dx' + \int_{x_1}^x k_p(x') dx' = \int_{x_0}^{x_1} k_p(x') dx' + 2 \int_{x_1}^x k_p(x') dx' \quad (3.14)$$

Eq.(3.14) can now be written:

$$\varphi_p - \varphi_s = 2 \frac{\omega_0}{c} \int_{x_1}^x \sqrt{1 - \frac{n_e(x')}{n_c}} dx' = 2 \frac{\omega_0}{c} \int_{x_1}^x \sqrt{1 - \frac{n_{max}}{n_c} \frac{x}{L}} dx' \quad (3.15)$$

The integration of the previous equations gives:

$$\varphi_p - \varphi_s = -\frac{4}{3} \frac{\omega_0}{c} L \frac{n_c}{n_{max}} \left(1 - \frac{n_{max}}{n_c} \frac{x}{L}\right)^{(3/2)} \quad (3.16)$$

This means that, at a first order and for small values of $\frac{n_{max}}{n_c}$, the space dependence of the total phase $\varphi_p - \varphi_s$ is similar to the one given by Eq.(3.9) for a constant plasma. The effect on the phase evolution due to the propagation of the laser in an inhomogeneous plasma and without coupling is negligible.

3.2.2 The role of a plasma density shape on the phase evolution

The comparison is made between two constant density profile, one with a maximum of the plasma density of $n_{max}/n_c = 0.1$ (Fig.(3.7(a)), in the following we refer to this case as *const1*) and one with $n_{max}/n_c = 0.05$ (Fig.(3.7(b)), case *const2* in the following), a triangular one with the maximum shifted towards left (Fig.(3.7(c)), case *trl*) and $n_{max}/n_c = 0.1$ and a triangular one with the maximum shifted towards right (Fig.(3.7(d)), case *trr*) and $n_{max}/n_c = 0.1$. The choice of $n_{max}/n_c = 0.05$ for the case *const2* is dictated by the fact that for a linear ramp with $0 \leq n_{max}/n_c \leq 0.1$ the average density is 0.05 and thus it seems reasonable to make a comparison with a constant density of this value. The laser are now crossing on the right boundary of the plasma, at $x = 650 \mu m$, in order to let the seed to explore the entire length of the plasma. In the following we make the hypothesis that the space coordinate is centered at $x_{cross} = 650 \mu m$, in a way that the position in the plasma is defined as $\hat{x} = x - x_{cross}$: the seed laser is travelling towards $\hat{x} < 0$. In Fig.(3.8)(a) we show the amplified seed in function of space at $t = 2.2 ps$ for all the case of interest: the final value of the seed electric field amplitude is strongly influenced by the shape of the plasma density profile. As expected the seed is better amplified in the case *const1* compared to *const2* one. The cases *const1* (black line) and *trr* (green line) are comparable in terms of final electric field amplitude and a bigger difference can be see if we compare the *trr* case with the *const2* one. This means that the direction of the plasma density ramp compensates for the fact that the coupling can be locally weaker. In Fig.(3.8)(b) we present the seed amplification at $x = 550 \mu$ in function of time we see that the seed is growing faster for the case *const1*. To justify all these results, in the following we explore the evolution of the seed phase in function of the plasma density shape; we will show that the density profile acts on the coupling in a similar way to a chirp.

To study the evolution of the phase of the seed pulse, we rewrite Eq.(30)-(32) making

appearing explicitly the dependance on the electron density in the plasma frequency.

$$(\partial_t + v_g^p \partial_x) E_p = -i \frac{\omega_{pe}^2(x)}{4\omega_0} N E_s = -i \mu(x) n_e E_s \quad (3.17)$$

$$(\partial_t - v_g^s \partial_x) E_s = -i \frac{\omega_{pe}^2(x)}{4\omega_0} N^* E_p = -i \mu(x) n_e^* E_p \quad (3.18)$$

$$(\partial_t^2 - c_s^2 \partial_x^2) N = -\frac{2Ze^2}{m_e m_i c^2} E_p E_s^* = -\Lambda E_p E_s^* \quad (3.19)$$

Notice that the coupling coefficient for the seed and the pump $\mu(x) = \frac{\omega_{pe}^2(x)}{4\omega_0}$ is now space dependent. As we have done in the previous section, we explicit Eq.(3.17)-(3.19) in terms of phase and amplitude and we neglect the terms multiplied by c_s^2 :

$$(\partial_t + v_g \partial_x) E_p = -\mu(x) N E_s \sin \vartheta \quad (3.20)$$

$$(\partial_t + v_g \partial_x) \varphi_p = -\mu(x) \frac{N E_s}{E_p} \cos \vartheta \quad (3.21)$$

$$(\partial_t - v_g \partial_x) E_s = \mu(x) N E_p \sin \vartheta \quad (3.22)$$

$$(\partial_t - v_g \partial_x) \varphi_s = -\mu(x) \frac{N E_p}{E_s} \cos \vartheta \quad (3.23)$$

$$\partial_t^2 N - N(\partial_t \varphi^2) = -\Lambda E_p E_s \cos \vartheta \quad (3.24)$$

$$\partial_t N \partial_t \varphi = -\frac{\Lambda}{2} E_p E_s \sin \vartheta \quad (3.25)$$

In Eq.(3.20)-(3.25) we neglected the dependence of the group speed on the local value of density. To evaluate the density perturbation evolution $N(\hat{x}, t)$ we follow the same procedure than Sec.2.3 but applied at the local density value. We find:

$$N(x, t) = -\Lambda E_p E_s \frac{1}{2} \left(t - \frac{|\hat{x}|}{v_g} \right)^2 \quad (3.26)$$

that is valid for $\hat{x} < 0$ and $t > |\hat{x}|/v_g$ since the coupling at a given point starts only when the seed has reached that point. To find the solution of the phase of the seed, we make a change a variable in order to follow the seed pulse along its propagation.

$$y = \hat{x} + v_g t \quad (3.27)$$

$$\tau = t \quad (3.28)$$

As before, the initial value of the global phase will be $\vartheta = -\pi$, then Eq.(3.23) becomes:

$$\partial_\tau \varphi_s(y, \tau) = \mu(y) \frac{E_p}{E_s} |N(y, \tau)| = \frac{1}{2} \mu(y) \Lambda E_p^2 \left(\frac{y}{v_g} \right)^2 \quad (3.29)$$

From Eq.(3.29), it is now possible to find a solution of φ_s for the cases of Fig.(3.7) with respect to the different plasma shapes.

3.2.3 Density profile with $n_0(\hat{x} = 0) \neq 0$

For the cases with a constant density profile (*const₁* and *const₂*) or with a triangular profile with the maximum of the density shifted towards rights (*trr*), we can write:

$$n_0(\hat{x}) = n_{max} \left(1 + \frac{\hat{x}}{L} \right) \quad (3.30)$$

where, for $L > 0$ and $-L < \hat{x} < 0$, Eq.(3.30) describes a density profile for which the density is linearly decreasing along the plasma length L (case *trr*) or a constant profile if $L = \infty$. In Eq.(3.30), n_{max} is the plasma density value at $\hat{x} = 0$. In the space frame of the propagating seed we obtain:

$$n_0(y, \tau) = n_{max} \left(1 + \frac{y - v_g \tau}{L} \right) \quad (3.31)$$

Replacing in Eq.(3.29) we find:

$$\partial_\tau \varphi_s(y, \tau) = \frac{1}{2} \mu^{max} \Lambda E_p^2 \left(1 + \frac{y - v_g \tau}{L} \right) \left(\frac{y}{v_g} \right)^2 \quad (3.32)$$

where μ^{max} is the pump and seed coupling parameter evaluated at $n_0(\hat{x} = 0) = n_{max}$. Integrating, we can find the expression of the seed phase φ_s :

$$\varphi_s(y, \tau) = \int_{y/v_g}^{\tau} \partial_\tau \varphi_s(y, \tau) = \frac{1}{4} \mu^{max} \Lambda E_p^2 \frac{L}{v_g} \left(\frac{y}{v_g} \right)^2 \left[1 - \left(1 + \frac{y - v_g \tau}{L} \right)^2 \right] \quad (3.33)$$

or in units of \hat{x} :

$$\varphi_s(\hat{x}, t) = \frac{1}{4} \mu^{max} \Lambda E_p^2 \frac{|\hat{x}|}{v_g} \left(t - \frac{|\hat{x}|}{v_g} \right)^2 \left(2 - \frac{|\hat{x}|}{v_g} \right) \quad (3.34)$$

that is valid for $\hat{x} \leq 0$ and $t > |\hat{x}|/v_g$. The term $\frac{1}{4} \mu^{max} \Lambda E_p^2$ of Eq.(3.34) can be written in terms of γ_{sc} :

$$\frac{1}{4}\mu^{max}\Lambda E_p^2 = \frac{1}{4}\frac{\omega_{pe}^2(\hat{x}=0)}{4\omega_0}\frac{2Ze^2}{m_em_ic^2}E_p^2 = \frac{2}{3\sqrt{3}}\gamma_{scmax}^3 \quad (3.35)$$

where γ_{scmax} is the value of growth rate at $\hat{x} = 0$. Eq.(3.34) writes now:

$$\varphi_s(\hat{x}, t) = \frac{4}{3\sqrt{3}}\gamma_{scmax}^3\frac{|\hat{x}|}{v_g}\left(t - \frac{|\hat{x}|}{v_g}\right)^2\left(1 - \frac{1}{2}\frac{|\hat{x}|}{L}\right) \quad (3.36)$$

If now we consider the case of a constant plasma density profile (3.7)(a)(b)), $L = \infty$, Eq.(3.36) becomes:

$$\varphi_s(\hat{x}, t) \approx \frac{4}{3\sqrt{3}}\gamma_{sc}^3\frac{|\hat{x}|}{v_g}\left(t - \frac{|\hat{x}|}{v_g}\right)^2 \quad (3.37)$$

For an homogeneous density profile we can estimate the time needed for the phase of the seed to reach $\pi/3$, value at which the exponential regime of amplification starts:

$$t_i^{const}(x) \approx \frac{|\hat{x}|}{v_g} + \left(\frac{\frac{\sqrt{3}\pi}{4}}{\gamma_{sc}^3\frac{|\hat{x}|}{v_g}}\right)^{1/2} \quad (3.38)$$

The closest position at which $\varphi_s = \pi/3$ for a constant density profile is then:

$$\frac{d(t_i^{const}(\hat{x}))}{d(\hat{x})} = 0 \rightarrow |\hat{x}|^{const} = \left(\frac{\sqrt{3}\pi}{16}\right)^{1/3}\frac{v_g}{\gamma_{sc}} \approx 0.7\frac{v_g}{\gamma_{sc}} \quad (3.39)$$

and the corresponding time is:

$$t_{min}^{const} = 3\left(\frac{\sqrt{3}\pi}{16}\right)^{1/3}\frac{1}{\gamma_{sc}} \approx 2.1\frac{1}{\gamma_{sc}} \quad (3.40)$$

On the other hand, the time needed for the seed phase to be equal to $\pi/3$ for a triangular density profile with the maximum shifted towards right (Fig.(3.7(d))) is:

$$t_i^{trr}(\hat{x}) = \frac{|\hat{x}|}{v_g} + \left(\frac{\frac{\sqrt{3}\pi}{4}}{\gamma_{scmax}^3\frac{|\hat{x}|}{v_g}\left(1 - \frac{1}{2}\frac{|\hat{x}|}{L}\right)}\right)^{1/2} \quad (3.41)$$

For $|\hat{x}| \ll L$, this can be written as:

$$t_i^{trr}(\hat{x}) \approx \frac{|\hat{x}|}{v_g} + \left(\frac{\frac{\sqrt{3}\pi}{4}}{\gamma_{scmax}^3\frac{|\hat{x}|}{v_g}}\right)^{1/2}\left(1 + \frac{1}{4}\frac{|\hat{x}|}{L}\right) \quad (3.42)$$

Making the assumption that $v_g/(L\gamma_{sc}) \ll 1$, the closest position at which $\varphi_s = \pi/3$ for a triangular density profile is :

$$|\hat{x}|^{trr} \approx \left(\frac{\sqrt{3}\pi}{16}\right)^{1/3} \frac{v_g}{\gamma_{scmax}} \left[1 - \frac{1}{6} \left(\frac{\sqrt{3}\pi}{16}\right)^{1/3} \frac{v_g}{L\gamma_{scmax}} \right] \approx \frac{0.7v_g}{\gamma_{scmax}} \left(1 - 0.12 \frac{v_g}{L\gamma_{scmax}} \right) \quad (3.43)$$

that corresponds to a time of the order of:

$$t_{min}^{trr} \approx 3 \left(\frac{\sqrt{3}\pi}{16}\right)^{1/3} \frac{1}{\gamma_{scmax}} \left[1 + \frac{1}{18} \frac{1}{6} \left(\frac{\sqrt{3}\pi}{16}\right)^{1/3} \frac{v_g}{L\gamma_{scmax}} \right] \approx \frac{2.1}{\gamma_{scmax}} \left(1 + 0.04 \frac{v_g}{L\gamma_{scmax}} \right) \quad (3.44)$$

If we compare the expression of $|\hat{x}|^{trr}$ for a triangular profile with a linear density spanning between 0 and n_{max} with $|\hat{x}|^{const}$ for a constant density profile with a density equal to the average density, it follows that the case *trr* is most favorable as the seed enters earlier the exponential regime and the self-similar regime. This is confirmed by the simulation results shown in Fig.(3.8). If we look at the evolution of the electric field amplitude of the seed as function of time at $\hat{x} = -100 \mu m$ ($x = 550 \mu m$) in Fig.(3.8)(b) we can see that the seed is growing faster for the case *const*₁ (with density $n/n_c = 0.1$, black line) compared to the simulation *trr* (green line). On the hand, the case *trr* clearly is growing faster than the simulation *const*₂ with density $n/n_c = 0.05$ (pink line). The same behavior is visible in Fig.(3.8)(a) in which we show the final seed amplitude as function of space for the cases considered in this section: the *trr* attains higher field amplitudes compared to the case *const*₂. The simulation for the case *trl* is discussed in the following section.

3.2.4 Density profile with $n_0(\hat{x} = 0) = 0$

The same procedure can be adopted if we consider the following density profile shape:

$$n_0(\hat{x}) = -n_{max} \frac{\hat{x}}{L} \quad (3.45)$$

In this case, for $L > 0$ the local value of plasma density is increasing along $\hat{x} < 0$, as in the case *trl* (Fig.3.7(c)). n_{max} is the maximum plasma density evaluated at $\hat{x} = -L$. In the space frame of the seed, Eq.(3.45) reads:

$$n_0(y, \tau) = -n_{max} \frac{y - v_g \tau}{L} \quad (3.46)$$

The evolution of the seed phase is now:

$$\varphi_s(\hat{x}, t) = \frac{1}{4} \mu^{max} \Lambda E_p^2 \frac{1}{L v_g} \hat{x}^2 \left(t - \frac{|\hat{x}|}{v_g} \right)^2 = \frac{2}{3\sqrt{3}} \gamma_{scmax}^3 \frac{v_g}{L} \frac{\hat{x}^2}{v_g^2} \left(t - \frac{|\hat{x}|}{v_g} \right)^2 \quad (3.47)$$

where μ^{max} is now the pump and seed coupling parameter evaluated at $n_0(\hat{x} = -L) = n_{max}$.

The value of $\varphi_s = \pi/3$ is reached at a time of the order of:

$$t_i^{trl}(\hat{x}) = \frac{|\hat{x}|}{v_g} + \frac{v_g}{|\hat{x}|} \left(\frac{\sqrt{3}\pi}{2} \frac{L}{v_g \gamma_{scmax}^3} \right)^{1/2} \quad (3.48)$$

The closest point with respect to the initial interaction point at which the seed phase is equal to $\pi/3$ is:

$$|\hat{x}|^{trl} = \frac{v_g}{\gamma_{scmax}} \left(\frac{\sqrt{3}\pi}{2} \frac{L}{v_g \gamma_{scmax}^3} \right)^{1/4} \approx 1.3 \frac{v_g}{\gamma_{scmax}} \left(\frac{\gamma_{scmax} L}{v_g} \right)^{1/4} \quad (3.49)$$

and the correspond time is:

$$t_{min}^{trl} = 2 \left(\frac{\sqrt{3}\pi}{2} \frac{L}{v_g \gamma_{scmax}^3} \right)^{1/4} \approx \frac{2.6}{\gamma_{scmax}} \left(\frac{\gamma_{scmax} L}{v_g} \right)^{1/4} \quad (3.50)$$

The time necessary for the seed to reach $\pi/3$ for the case *trl* is longer compared to the cases *const*_{1,2} and *trr* and the position where the exponential growth starts is further away in the density ramp. This confirmed by the simulations shown in Fig(3.8): the case *trl* is always the worst one in terms of seed electric field amplification, even compared to a simulation with a constant plasma density profile and $n/n_c = 0.05$ (case *const*₂, pink line).

3.2.5 Intrinsic frequency chirp due to a inhomogeneous plasma density profile

In the previous subsections we showed how the evolution of the phase of the seed is influenced by the shape of the density profile. In terms of final value of the amplitude of the electric field of the amplified seed at the end of the simulations, we showed that the cases *const*₁ and *trr* are comparable, even if in the triangular case the seed is exploring a lower value of averaged density and, indeed, *trr* shows a better amplification than the case *const*₂, a constant profile with $n/n_c = 0.05$. The averaged density value of the entire plasma explored by the seed is $n_{av}/n_c = 0.05$. Motivated by these results and by the improvement in the coupling when the right chirp is chosen for the pump, in

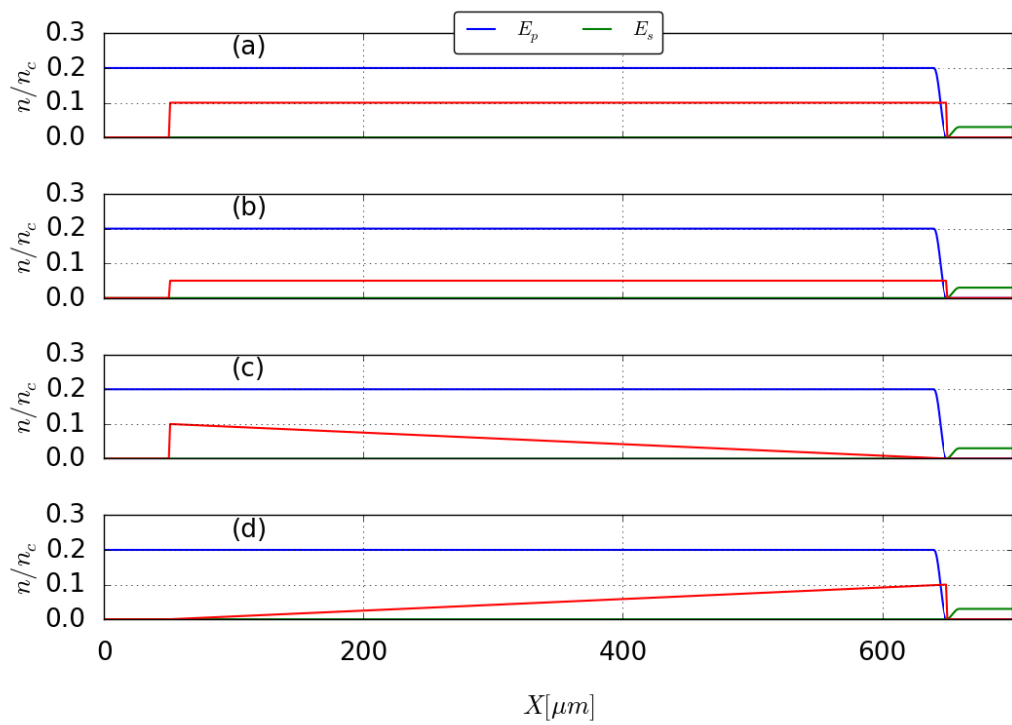


Figure 3.7: Initial configuration of the lasers in function of space for the case $const_1$ (a), $const_2$ (b), trl (c) and trr (d)

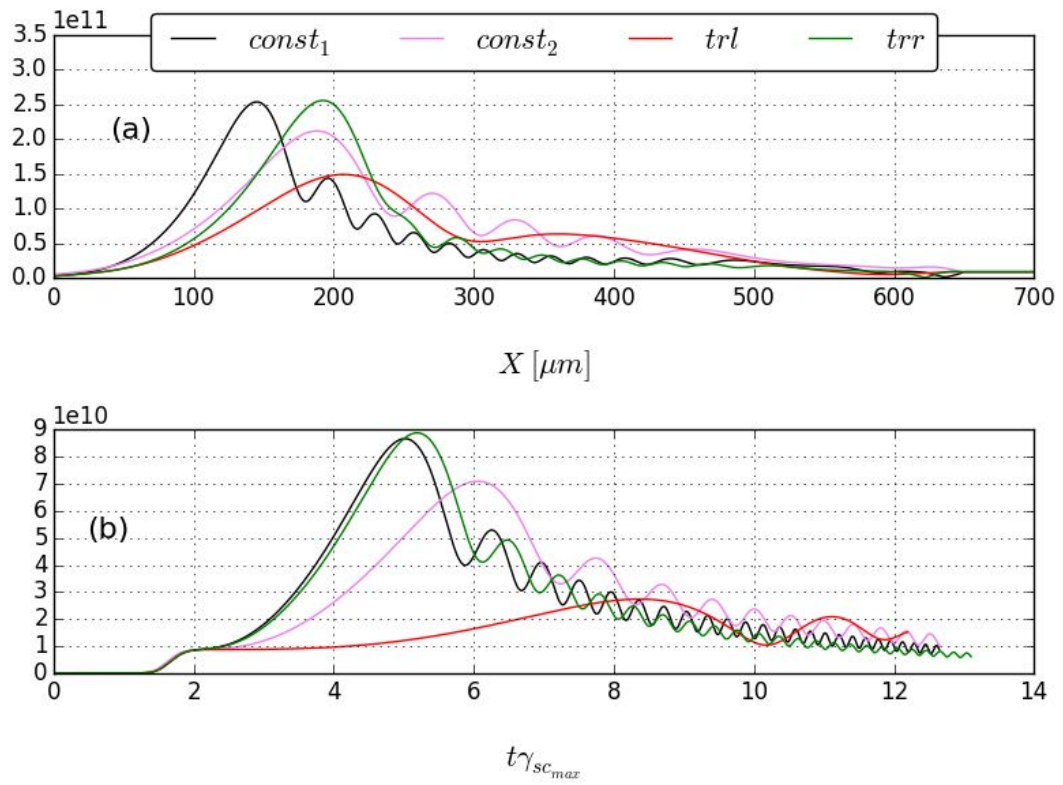


Figure 3.8: Electric field amplitude of the seed in function of space (a) and time (b) (at $x = 550\mu m$) for the different plasma density shape considered.

this section we make a comparison between the seed phase variation for the cases with an inhomogeneous density profile with a possible value of the chirp parameter α to be imposed to the pump laser in a constant density in order to find the same shapes and values of final electric field amplitude. In previous sections we introduced the chirp phase as:

$$\phi(x, t) = \alpha (k_0(x - x_0) - \omega_0(t - t_0))^2 \quad (3.51)$$

where x_0 and t_0 are the centering of the chirp in space and time, respectively. The frequency of the pump is varying as:

$$\omega(x, t) = \omega_0 + 2\alpha\omega_0 (k_0(x - x_0) - \omega_0(t - t_0)) \quad (3.52)$$

? If, as before, we introduce a new space coordinate centered on the lasers crossing point, $\hat{x} = x - x_{cross}$, for $x_0 = x_{cross}$ and $t_0 = 0$ we can write the pump frequency as:

$$\omega(\hat{x}, t) = \omega_0 + 2\alpha\omega_0 (k_0\hat{x} - \omega_0 t) \quad (3.53)$$

As \hat{x} is defined negative along the plasma profile, we can replace $\hat{x} = -v_g t$:

$$\omega(\hat{x}, t) = \omega_0 + 2\alpha\omega_0 (k_0(-v_g t) - \omega_0 t) \approx \omega_0 - 4\alpha\omega_0^2 t = \omega_0 - 4\alpha\omega_0^2 \frac{|\hat{x}|}{v_g} \quad (3.54)$$

Notice that in Eq.(3.54) we made the approximation that $k_0 v_g \approx \omega_0$.

In order to estimate an effective chirp associated to the profile, we consider the local value of the strong coupling growth rate. For a triangular profile with the maximum shifted towards right (case *trr*) the local value of the growth rate $\gamma_{sc}(x)$ is varying linearly from its maximum value as:

$$\gamma_{sc}(\hat{x}) \approx \gamma_{scmax} \left(1 + \frac{\hat{x}}{L}\right)^{1/3} \quad (3.55)$$

The corresponding value of downshift is then:

$$\Delta\omega_{sc}(\hat{x}) = \frac{1}{\sqrt{3}}\gamma_{sc}(\hat{x}) \approx \frac{\gamma_{scmax}}{\sqrt{3}} \left(1 + \frac{\hat{x}}{L}\right)^{1/3} \quad (3.56)$$

If now we compare Eq.(3.55) and Eq.(3.54) we can have an estimation of the value of the chirp parameter to be imposed to the pump in a constant density profile:

$$\alpha^{trr} = -\frac{\gamma_{scmax} v_g}{4\sqrt{3}\omega_0^2 |\hat{x}|} \left(1 + \frac{\hat{x}}{L}\right)^{1/3} \quad (3.57)$$

Notice that α^{trr} is negative and that Eq.(3.57) is valid for $x < 0$. If now we estimate

α^{trr} in the middle of the box, at $|\hat{x}| = L/2$, we find:

$$\alpha^{trr} \left(\hat{x} = \frac{L}{2} \right) = -\frac{\gamma_{sc_{av}} v_g}{2\sqrt{3}\omega_0^2 L} \approx -2.7 \times 10^{-7} \quad (3.58)$$

where $\gamma_{sc_{av}}$ is defined as:

$$\gamma_{sc_{av}} = \gamma_{sc_{max}} \left(1 + \frac{\hat{x}}{L} \right)^{1/3} \quad (3.59)$$

at $\hat{x} = L/2$. This result of Eq.(3.58) is consistent with what found earlier: both a triangular plasma profile with the maximum shifted towards right (*trr*) and a negative chirp contribute to enhancing the maximum of the first probe. For a plasma density profile with the maximum shifted towards left (case *trl*), we have analogously a positive value of α :

$$\alpha^{trl} = -\alpha^{trr} \approx 2.7 \times 10^{-7} \quad (3.60)$$

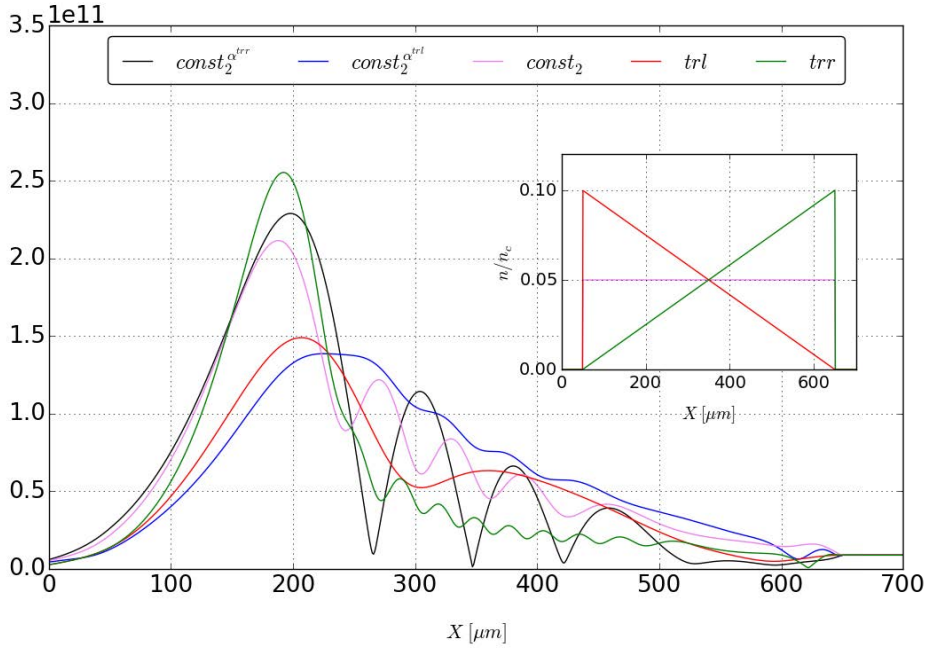


Figure 3.9: Electric field amplitude of the seed in function of space for different plasma shapes and different values of chirp parameter α . The comparison is made among a case in which the plasma density is constant and the pump is chirped with $\alpha = \alpha^{trr} \approx -2.7 \times 10^{-7}$, ($const_2^{\alpha^{trr}}$), a case in which the plasma density is constant and $\alpha = \alpha^{trl} \approx 2.7 \times 10^{-7}$ ($const_2^{\alpha^{trl}}$), a case in which the plasma density is constant and the pump is not chirped ($const_2$) and the cases with a triangular plasma density profile (*trl* and *trr*). The inset shows the plasma density profiles considered.

In Fig.(3.9) we show the electric field amplitude of the seed in function of space at the end of the simulation and for different plasma density shape: $const_2^{trr}$ is a simulation with a constant plasma with $n/n_c = 0.05$ and $\alpha = \alpha^{trr}$ (black line), $const_2^{trl}$ is a simulation with a constant plasma with $n/n_c = 0.05$ and $\alpha = \alpha^{trl}$ (blue line), $const_2$ is a simulation with a constant plasma with $n/n_c = 0.05$ and $\alpha = 0$ (violet line), and trl (red line) and trr (green line) are the results for the triangular shapes proposed in the previous subsection. For these simulations, when the pump is chirped (cases $const_2^{trr}$ and $const_2^{trl}$) the chirp is centered at the initial lasers crossing point. The peak of the amplified seed for the case $const_2^{trr}$ is now closer to the case trr , compared to the case where the pump is not chirped ($const_2$): this means that a triangular density profile with the maximum shifted towards right is affecting the phases evolution similarly to a case in which the pump is upshifted compared to seed. The same behavior is reproduced if we compare the cases $const_2^{trl}$ and trl : the peak of the amplified seed for a constant density profile and a pump with a positive value of the chirp parameter is closer to the case where the pump is not chirped and the plasma density is triangular with the maximum shifted towards left. Notice however that this is true only for the first peak of the amplified seed, since the constant case $const_2^{trr}$ and the triangular one trr behave quite differently in the trailing part, as shown in Fig.(3.9): the π -pulse behavior is very clear with the $const_2^{trr}$ case, while the triangular shape enhances the first peak with a very little coupling in the subsequent peaks. This can be an interesting feature of a decreasing profile as favoring the energy exchange mainly in the first peak.

All these results are confirmed in Table 3.2, where we resume the results in terms of final electric field amplitude, final duration and energy exchange. As before, $E_{in}^{seed} = 8.67 \times 10^9$ and E_{out}^{seed} are the electric field amplitude before and at the end of the amplification, $FWHM_{out}$ is the final duration of the higher peak of the amplified seed, $n_{max}/n_c = 0.05$ is the maximum value of the plasma density, $Q_{in}^{pump} = 4666 J/cm^2$ is the available pump energy Q_{gain} is the energy gain of the amplified seed evaluated on the entire simulation box subtracted of the initial seed energy $Q_{in}^{seed} = 23 J/cm^2$. The simulations $const_2^{trr}$ and trr are very similar in terms of final electric field amplitude of the seed, final duration and energy transfer. This is true also if we make the comparison between the cases $const_2^{trr}$ and trl : for these simulations the energy transfer is sensibly reduced and the duration of the amplified seed is very large. Notice that, compared to the values shown in Table 3.1, the energy transferred in the simulations of Table 3.2 is smaller even if the seed propagates in a longer plasma. This is because here the average density is $n/n_c = 0.05$.

Table 3.2: Overview of the results of the numerical simulations for the different run of Sec. 3.2.5. The initial value of the electric field for the seed is $E_{in}^{seed} = 8.67 \times 10^9$ V/m; the available pump energy is $Q_{in}^{pump} = 4666$ J/cm². E_{out}^{seed} is expressed in V/m, $FWHM_{out}$ in unit of fs and Q_{gain} in J/cm²

<i>run</i>	α	E_{out}^{seed}	$FWHM_{out}$	Q_{gain}	$\%pump$
$const_2^{trr}$	$-2.7 \cdot 10^{-7}$	$2.27 \cdot 10^{11}$	383	2280	48
$const_2^{trl}$	$2.7 \cdot 10^{-7}$	$1.37 \cdot 10^{11}$	843	1573	34
$const_2$	0.0	$2.1 \cdot 10^{11}$	360	2139	46
<i>trr</i>	0.0	$2.53 \cdot 10^{11}$	330	2200	47
<i>trl</i>	0.0	$1.48 \cdot 10^{11}$	506	1303	28

3.2.6 Influence of realistic plasma density profile and laser shape on the SBS amplification

In this section we show the results of the SBS amplification in the case of realistic plasma and laser configurations. In a first series of simulations we consider a gaussian plasma density profile with $n_{max}/n_c = 0.1$ and a plasma length of $L = 600\mu m$. As before, the pump and seed lasers are kept constant and at $t = 0$ they are crossing on the right side plasma, at $x = 650\mu m$, in a way to let the seed pulse to interact with the whole plasma length (Fig. (3.10)). In Fig.(3.11) we show the evolution of the seed electric field amplitude in function of time and in coincidence of the maximum of the plasma density, at $x = 350$, for different values of positive (Fig.(3.11)(a)) and negative (Fig.(3.11)(b)) values of the chirp parameter α . As in the simulations presented in the previous sections, the highest intensity amplification is reached for negative values of α . The best amplification for $\alpha = -2 \cdot 10^{-7}$, comparable with the optimal value found in Sec. 3.1, even if a bit smaller. For positive values of α the amplification is strongly quenched. This is true even if α is negative but large ($|\alpha| > 6.5 \times 10^{-7}$). Notice that compared to the results found in Sec. 3.1 the seed amplification is now more sensitive to the chirp parameter values, even if this is small: the amplification of the seed in a gaussian shaped plasma with a chirped pump is now the results of the sum of these two effects. Fig. (3.12) show the shapes of the pump and seed at the end of the amplification in function of space and for $\alpha = 0$ (solid lines) and $\alpha = -2 \cdot 10^{-7}$: with a negative chirped pump the seed is slightly better amplified.

To go further we show the results of simulations in which the pump and seed lasers have a temporal shape: in particular, the duration at Full Width at Half Maximum in intensity of the pump is $FWHM_p = 4.2 ps$ and for the seed we have $FWHM_s = 500 fs$. This allows one to study a situation closer to nowadays experiments [34] [35]. As the lasers pulse have a finite duration, we introduce the concept of relative delay between seed and pump lasers: this relative delay is defined as the time before the seed starts to enter the simulation box since the beginning of the simulation. For different values of relative delay, the maxima of the lasers pulses are crossing in different regions of the plasma. In Fig.(3.13) we show where the maxima of the pump and seed lasers are crossing for the simulations considered in this section. For $t_{delay} = 4.22 ps$ the lasers maxima are crossing at $x_{cross} = 500\mu m$ as shown in Fig.(3.13)(a); for $t_{delay} = 3.7 ps$ the crossing point is at $x_{cross} = 350\mu m$, exactly in the middle of the plasma where the maximum value of density is located (Fig.(3.13)(b)). For $t_{delay} = 3.18 ps$ the maxima of lasers are crossing at $x_{cross} = 200\mu m$ (Fig.(3.13)(c)). An optimal delay corresponds to the possibility of reaching higher growth rates, larger frequency spread and downshift of the backscattered wave. According to the linear analysis shown in

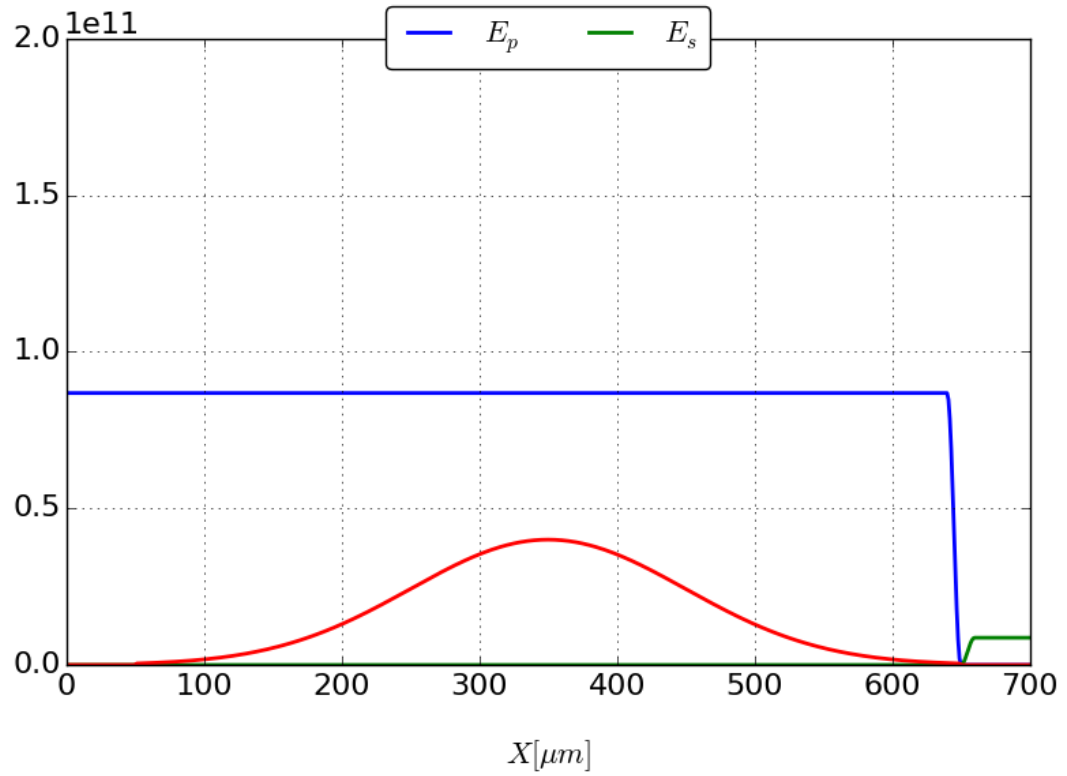


Figure 3.10: Initial configuration of the lasers pulses (pump in blue, seed in green) for the simulations with constant lasers and a gaussian plasma profile (red line). The electric field amplitudes are shown in units of V/m and the density is arbitrary units.

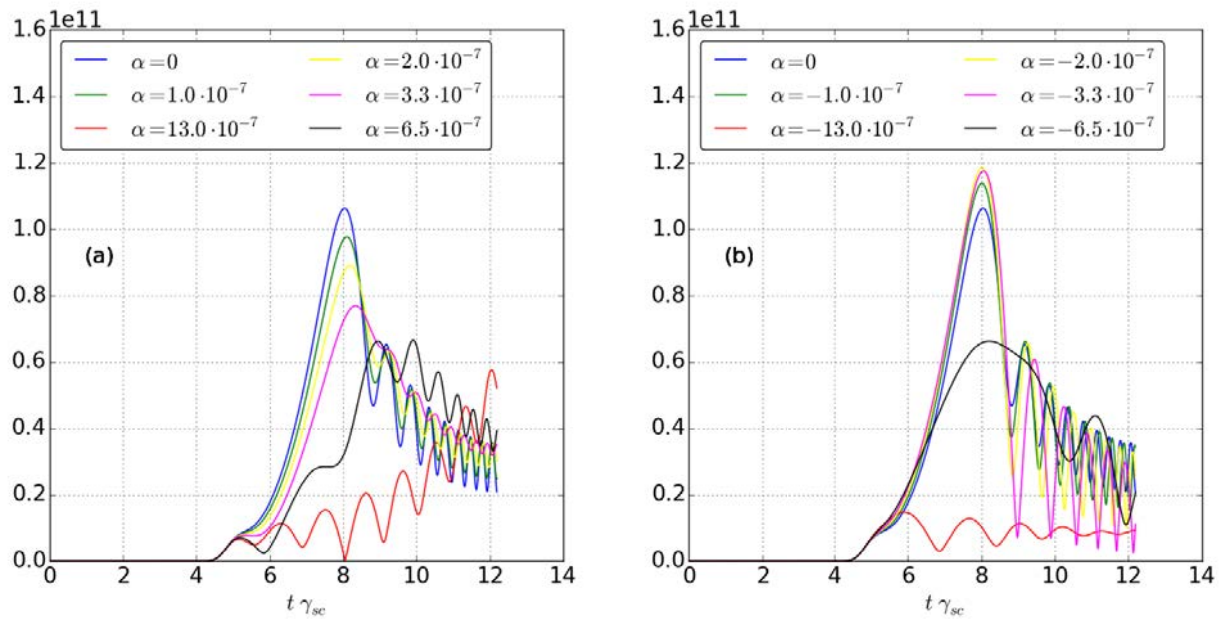


Figure 3.11: Evolution of the electric field amplitude of the seed in function of time at $x = 350\mu m$ for positive (a) and negative (b) values of α . In this series of simulations, both pump and seed laser are kept constant.

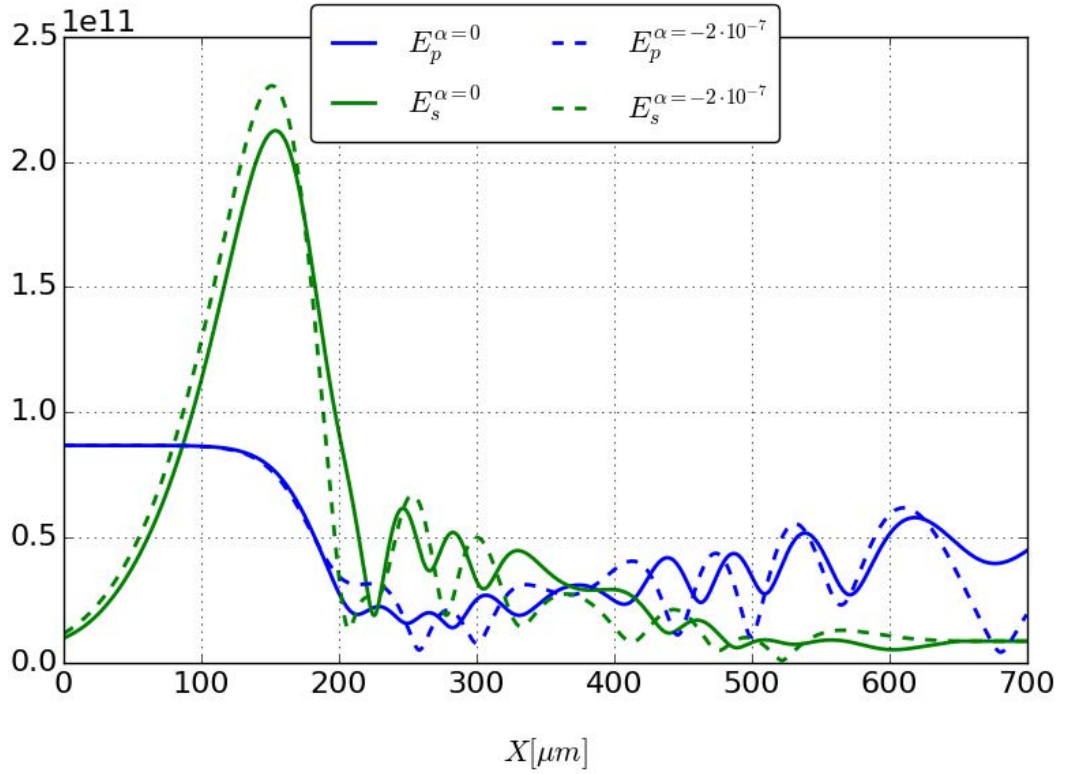


Figure 3.12: Electric fields amplitudes, in V/m , of the pump (blue lines) and of the seed (green lines) in function space, at $t = 2.6$ ps. The solid lines indicate the simulation results for $\alpha = 0$, the dashed ones are for $\alpha = -2 \cdot 10^{-7}$

Sec. 1.4.1 to maximize the sc-SBS coupling effect pump and seed lasers should cross at the center of the plasma density because, in the definition of γ_{sc} , the pump intensity and the plasma density appear as $\gamma_{sc} \propto (I_p n/n_c)^{1/3}$. In the case of a gaussian plasma density profile, one would then expect a symmetry in the amplification efficiency if the lasers cross on the right or on the left of the plasma maximum. In the following we will show this is not true; in Fig.(3.14) we show the final seed electric field amplitudes for the cases introduced. The highest values of amplification are obtained for the case where the maxima are crossing at $x_{cross} = 200 \mu m$, that means on the left of the plasma maximum. Consistently with previous results, a decreasing ramp as seen from the seed is more favorable, explaining why crossing in the first half of the plasma leads to larger final electric field amplitude. Moreover, we find the crossing more towards the border is slightly more favorable as in the zone of efficient growth more energy from the pump is available. We point out that the pump intensity intervenes on one side in the local value of the growth rate and on the other side as an energy "reservoir". In the considered simulation we find that, with respect to variations in the growth rate, the dominant effect is the variation of the density ramp: an optimal growth is when pump and seed cross an the first half of the plasma (as seen by the pump) and part of the decrease of the growth rate due to plasma density profile is compensated by the pump increasing.

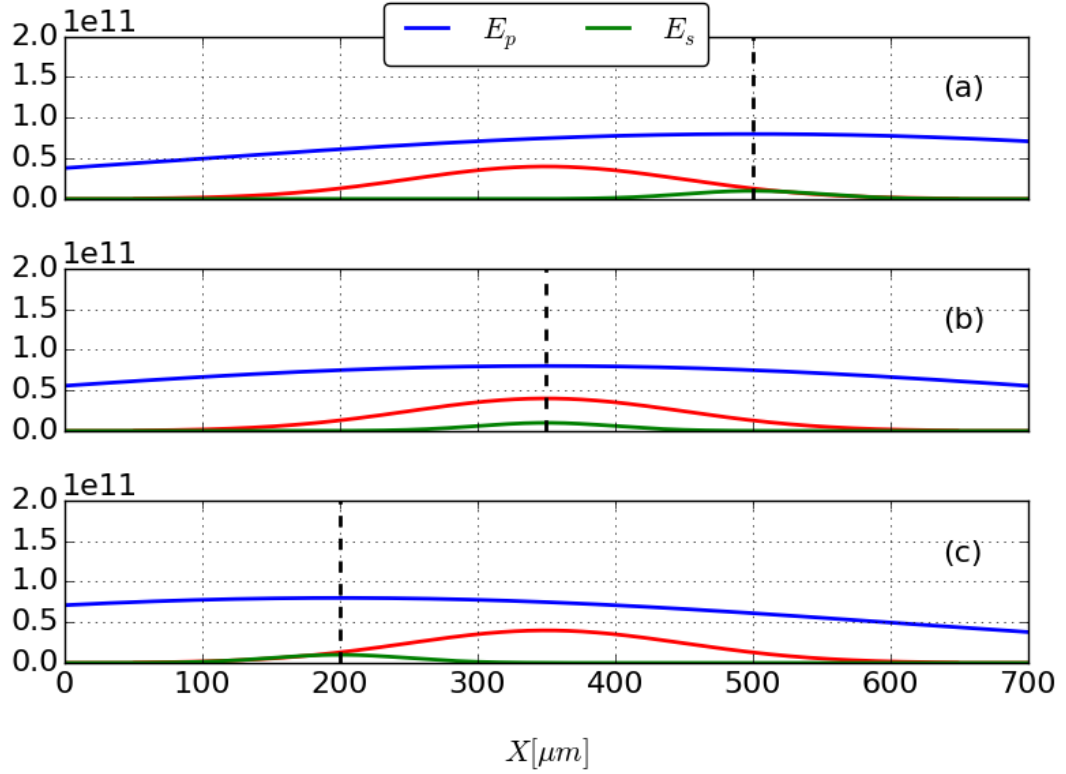


Figure 3.13: Initial configuration of the lasers pulses (pump in blue, seed in green) for the simulations with gaussian lasers and a gaussian plasma profile (red line). The electric field amplitudes are shown in units of V/m and the density is arbitrary units. The black dashed lines indicate the different crossing point considered. a) $x_{cross} = 500 \mu m$. b) $x_{cross} = 350 \mu m$. c) $x_{cross} = 200 \mu m$.

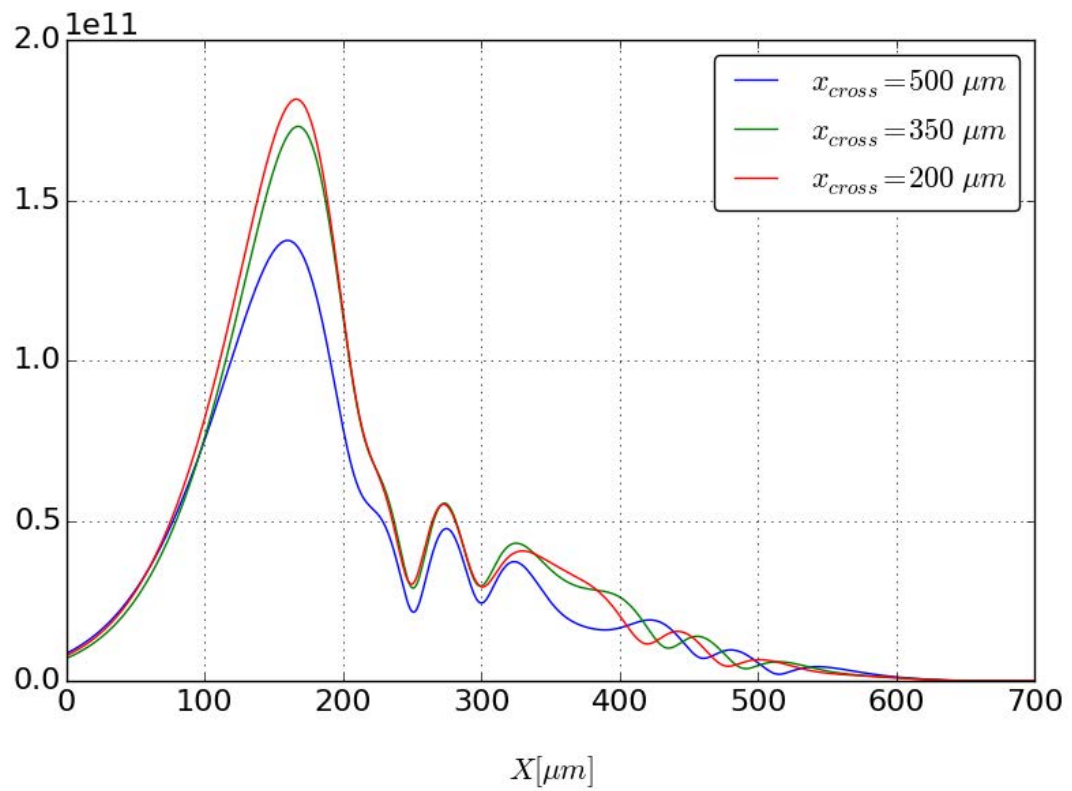


Figure 3.14: Final seed electric field amplitude (in V/m) as function of space for different crossing points of the pump and seed lasers.

3.3 Conclusions

In this chapter we showed how the sc-SBS coupling and then the efficiency of the seed amplification are affected by the presence of a frequency chirped pump. In chapter 2 we explained that, in the strong coupling regime, the total phase is continuously varying with time. The presence of a chirp can modify the time evolution of the total phase. Following the different stages of the amplification, we can define different values of the chirp parameter α that compensate the total phase variation. In correspondence of pump depletion, we have large energy transfer which is affecting the downshift of the seed frequency. Optimal coupling would then be achieved if the chirp phase compensates the seed phase at the moment pump depletion sets in. Imposing this condition, we find that *the amplification is improved* in terms of electric field amplitude and time definition of the width of the first peak *when α is negative and of the order of $\alpha_{tot} \approx -10^{-7}$* . If instead we impose a value of α for which the variation of the phase due to the laser chirp at the beginning of the interaction is of the same order of the seed phase φ_s , the seed phase doesn't evolve anymore and the seed amplification is quenched. This situation corresponds to positive and large values of $\alpha_i \approx 10^{-6}$. The energy transfer is strongly reduced if the chirp parameter is large (of the order of $|\alpha| \approx 10^{-6}$).

We then showed that *the seed amplification can be slightly improved (or reduced) if the chirp parameter is negative (positive) and small. Large values of α affect in a negative way the amplification reducing sensibly the energy transfer, no matter the sign of α* . In the second part of this chapter, we studied how the presence of an inhomogeneous plasma density profile affects the evolution of the seed phase and then of the total phase. We then showed that, contrary to SRS-based amplification, *sc-SBS requires a preferential gradient of the plasma profile with respect to the seed propagation. When the amplification happens along a plasma density linearly decreasing (case *trr* in the chapter) as seen by the seed during its propagation, the seed enters earlier the exponential regime and the self-similar regime and it attains the highest amplification. In this case the seed amplification is even better compared to a simulation with a constant plasma with density equal to the average of the density ramp*. In a decreasing density (with respect to the seed direction of propagation) the difference between the pump frequency and the seed frequency downshifted in the exponential regime decreases. *This is similar to the case of the seed amplification with a negatively chirped pump*. An effective chirp can then be defined at the average value of plasma density: for the parameters considered in this chapter we have

$\alpha_{trr} \approx -2.7 \times 10^{-7}$. Analogously, for a plasma density increasing along the seed propagation direction (case *trl* in the chapter), the amplification efficiency is reduced and the equivalent value of chirp is positive, $\alpha_{trl} = -\alpha_{trr} \approx 2.7 \times 10^{-7}$. Simulations of amplification in an homogeneous profile with the effective chirps shown confirm the validity of the estimation of α_{trr} and α_{trl} as the amplified values become very close to the values found with the inhomogeneous profiles. Notice however that an inhomogeneous density profile acts differently than the chirp in the trailing pulses. In particular, for a plasma profile as in the case *trr* the trailing peaks are very weak and the seed amplitude does not go to zero. This can be an interesting feature of a decreasing profile as favoring the energy exchange mainly in the first peak. All these results are confirmed in the cases of simulations in which the plasma density and laser shapes are closer to the experimental conditions. In the following chapter, we will show (using PIC simulations that allows one to take into account the complete dynamics of the coupling including the competition with other instabilities) that a decreasing profile as seen by the seed leads to larger amplification and allows to control unwanted spontaneous SRS backscattering of the pump.

Chapter 4

Parametric studies of sc-SBS optimal coupling via one-dimensional PIC simulations

In chapters 2 and 3 we described the sc-SBS amplification in terms of phases evolution and energy transfer directionality. In particular we approached the problem making appearing explicitly the amplitudes and the phases in the three equation system describing the sc-SBS amplification. In the present chapter we perform a set of one-dimensional (1D) PIC simulations performed with the code SMILEI [44](Chapter 6). This 1D approach has the advantage of allowing a parametric study and also it allows to focus on physical effects not dependent on the dimensionality. Two dimensional effects, such as filamentation and self focusing should not play a role in the range of parameters we explore [28][33]. The goal of the chapter is to optimize the plasma and laser parameters involved in the SBS amplification mechanism in realistic configurations, taking into account the competing phenomena (such as the spontaneous Raman backscattering of the pump) that can affect the amplification. The chapter is organized as following: in Sec.4.1 we show the set-up and the parameters chosen in the particle in cell (PIC) simulations. In Sec.4.2, we discuss the role of the shape of the plasma density in limiting SRS parasitic effects on the SBS amplification: we find that plasma shaping allows to partially control SRS affecting also the energy transfer. Typical experimental profiles of plasma produced from gas jet have gaussian shape and already help reducing significantly the spontaneous SRS. In Sec.4.3 we show the importance of the choice of the relative delay of interaction between pump and seed pulses: this is an important parameter as proved by simulations and experiments [34] [36] and the exact optimal delay has to be experimentally assessed for each particular configuration with a systematic scan of pump-seed synchronization. In Sec.4.4 we present how the initial

duration of the seed plays a role in the SBS amplification. In particular, we show that, if the initial seed duration is a fraction of γ_{sc} , the seed stretches before entering in the self-similar regime [30]. In Sec.4.5, we summarize, in terms of energy exchange between pump and seed lasers, the results of the simulations shown in Secs.4.2, 4.3, and 4.4.

4.1 Simulations set-up

The choice of the simulation parameters have been strongly motivated by recent experiments carried out at LULI in 2013 [34]. We consider an intensity of the pump and of the seed equal to $I_{pump} = 10^{15}\text{W/cm}^2$ and $I_{seed} = 3 \times 10^{13}\text{W/cm}^2$, respectively. The same wavelength $\lambda_0 = 1\mu\text{m}$ has been used for both laser beams, corresponding to a frequency $\omega_0 = 1.9 \times 10^{15}\text{rad/s}$. Both lasers have a gaussian temporal profile, where FWHM is the full-width-at-half-maximum in intensity and a cut-off at $\approx 3\sigma$ with $\sigma \approx FWHM/2.3548$. For the pump and seed, $FWHM_{pump} = 4.2\text{ ps}$ and $FWHM_{seed} = 500\text{ fs}$, respectively. The corresponding energy fluence for the pump and seed are $Q_p \approx 2.9\text{ kJ/cm}^2$ and $Q_s \approx 6.3\text{ J/cm}^2$, respectively. As in the experiments, the plasma (hydrogen gas, $Z = 1$) has a $0.5 - 1\text{mm}$ length, with the same ion and electron temperatures of $T_e = T_i = 300\text{eV}$ and a maximum density of $n/n_c = 0.05 - 0.1$. In the following sections, we show the results of simulations obtained when varying some of these physical parameters.

If not otherwise specified, the resolution in the x -direction is $\Delta x = \lambda_0/60$, with 750 particles per cell per species (ions and electrons), and the time resolution is around $\Delta t \approx 1/70 \times 1/\omega_0$. The standard interaction configuration in the figures of the simulations is that the pump comes from the left and the seed from the right. The field boundary conditions are open (Silver-Muller type) and the boundary conditions for the particles are reflective; during simulation the particles don't reach the simulation boundaries; $50 - 100\ \mu\text{m}$ of vacuum are left on both sides of the plasma.

4.2 Shape of the density profile

The presence of Raman backscattering during the propagation of the pump signal in the plasma reduces the available energy for SBS. In particular, the Raman backscattering growth rate [24], in practical units, is:

$$\gamma_{SRS} = 4.27 \cdot 10^{-3} \left(\frac{n}{n_c} \right)^{1/4} (I_{14} \lambda_{0p}^2)^{1/2} \omega_{0p}. \quad (4.1)$$

For typical parameters that we use in this chapter ($n/n_c = 0.05 - 0.1$, $I_p = 10^{15}\text{W/cm}^2$) $\gamma_{SRS}^{-1} \approx 78 - 66\text{ fs}$ that is much shorter than the time taken by the pump

to fill the whole plasma (half duration ≈ 2.1 ps). Thus we expect Raman to develop significantly before an efficient sc-SBS energy exchange can take place. A natural way to limit the spontaneous Raman backscattering of the pump laser would be to increase the temperature of the plasma or the particle density above $0.25 n_c$ [27][32][37][38], but this would bring the discussion far from the experimental plasma parameters we refer to. Another option to avoid the early Raman backscattering energy depletion is to choose a non-constant plasma density profile. To describe the convective Raman backscattering of the pump in the case of a plasma with a linear slope density shape, we follow the approach given by Rosenbluth [39]; the expression of the amplification factor in this case is:

$$A_{Ros} = \frac{\pi \gamma_{SRS}^2}{|V_1 V_2 \chi'_0|}, \quad (4.2)$$

where $V_{1,2}$ are the group velocities of the counter-propagating lasers and χ'_0 is:

$$\chi'_0 = \left(\frac{\partial \Delta k}{\partial x} \right)_{x=0}. \quad (4.3)$$

where χ'_0 is the dephasing due to the plasma density shape at the beginning of the density slope and Δk is the variation in k due to the density profile. If $A_{Ros} \lesssim \pi$, SRS is quenched. In this section we examine the effect of different shapes of plasma density on SRS of the pump. The pump laser propagates in a $500 \mu\text{m}$ fully ionized plasma without seed, we compare the case of constant, triangular and gaussian density profiles. In 1D simulations it is possible to easily distinguish the left propagating fields by simply taking in account the sign of the phase speed of the electromagnetic wave. The left propagating field is calculated as:

$$E_{\text{left}} = E_z - \frac{k(x)cB_y}{\omega_{0p}}, \quad (4.4)$$

with

$$k(x) = \omega_{0p}/c\sqrt{1 - n(x)/n_c}. \quad (4.5)$$

In Eq.(4.4), E_z and B_y are the electric and magnetic field of a laser beam linearly polarized along z . In Fig. 4.1 we show the electron density in green and the ion densities normalized to $n/n_c = 0.05$ and the pump laser intensity (in red) normalized to $I_p^{max} = 10^{15}\text{W}/\text{cm}^2$, at $t \approx 3.5$ ps after the pump starts to enter the simulation box, in the case of a constant plasma density profile. For reference, the time at which the maximum of the pump enters the left side of the box ($x = 0$) is $t_0 \approx 3.8$ ps. In the following sections, we refer to this case as **constant**. The blue signal represents the Raman backscattering of the pump, that can be identified also in the electron density

perturbations.

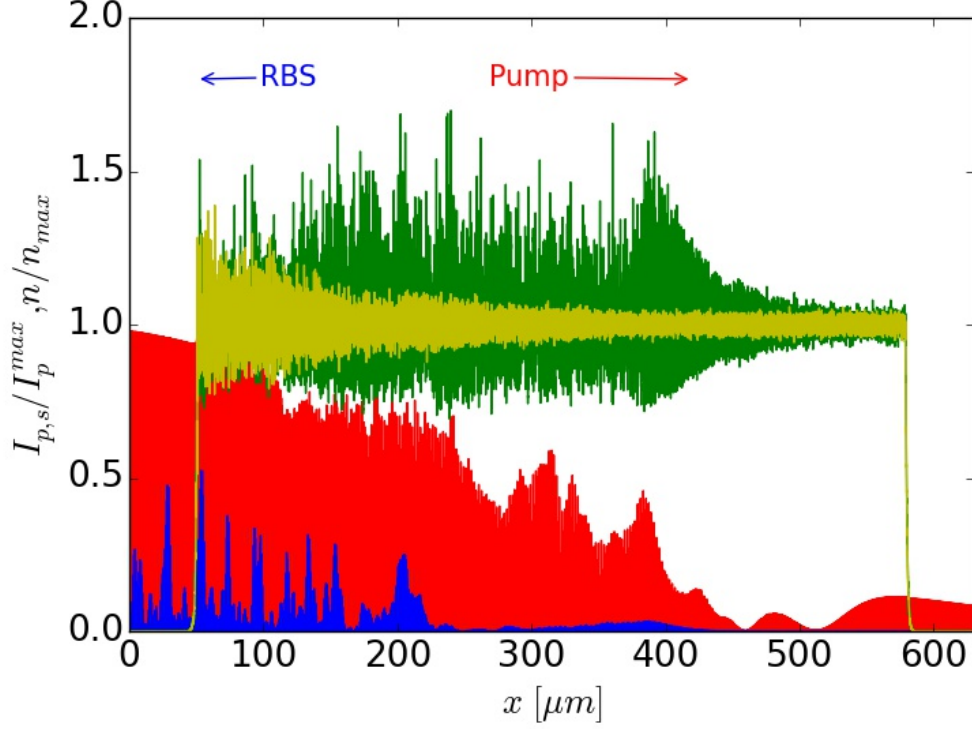


Figure 4.1: Pump laser propagating through a constant plasma at $t \approx 3.5$ ps since the beginning of the simulation (case **constant**). The red arrow indicates the direction of propagation of the laser. The backscattered light (RBS, in blue) propagates in the opposite direction. The green and yellow lines are the electrons and ions densities, respectively, normalized to $n/n_c = 0.05$.

The Raman Backscattering signal is easily identified in the frequency spectra presented in Fig. 4.2(a), integrated over 3.5 ps since the beginning of the simulation. The electric field has been recorded every time step on the left edge of the simulation box (in vacuum, $x = 0$, Fig. 4.1), so that the signal of the pump (incoming from left to right) and the backscattered pump and signals are registered; the spectra are normalized to the nominal laser frequency ω_0 . In Fig. 4.2(a) the peak at around $\omega_R/\omega_0 = 1 - \sqrt{n/n_c} = 0.77$ is the expected frequency for the Raman for the backscattered wave in vacuum. In Fig. 4.2(b) we show the temporal evolution of the spectra in k/k_0 , integrated over the entire simulation box. The expected value of k_R/k_0 for backscattered Raman laser is given by:

$$\frac{k_R}{k_0} = \sqrt{1 - n/n_c} + \sqrt{1 - 2\sqrt{n/n_c}} - 1. \quad (4.6)$$

In Eq.(4.6), for a plasma with $n/n_c = 0.05$, $k_R/k_0 \approx 0.72$. The peak at the value expected for the Raman instability (black dashed line on Fig. 4.2(b)) starts to grow ≈ 2.5 ps after the beginning of the simulation. At that time, no evidence of spontaneous SRS is present around $k/k_0 \sim 1$ (not shown in the figure). The Raman signals that start to develop at $t \approx 3.5$ ps and $k/k_0 > 0.75$ are due to the fact that the plasma density is not anymore homogeneous at that time.

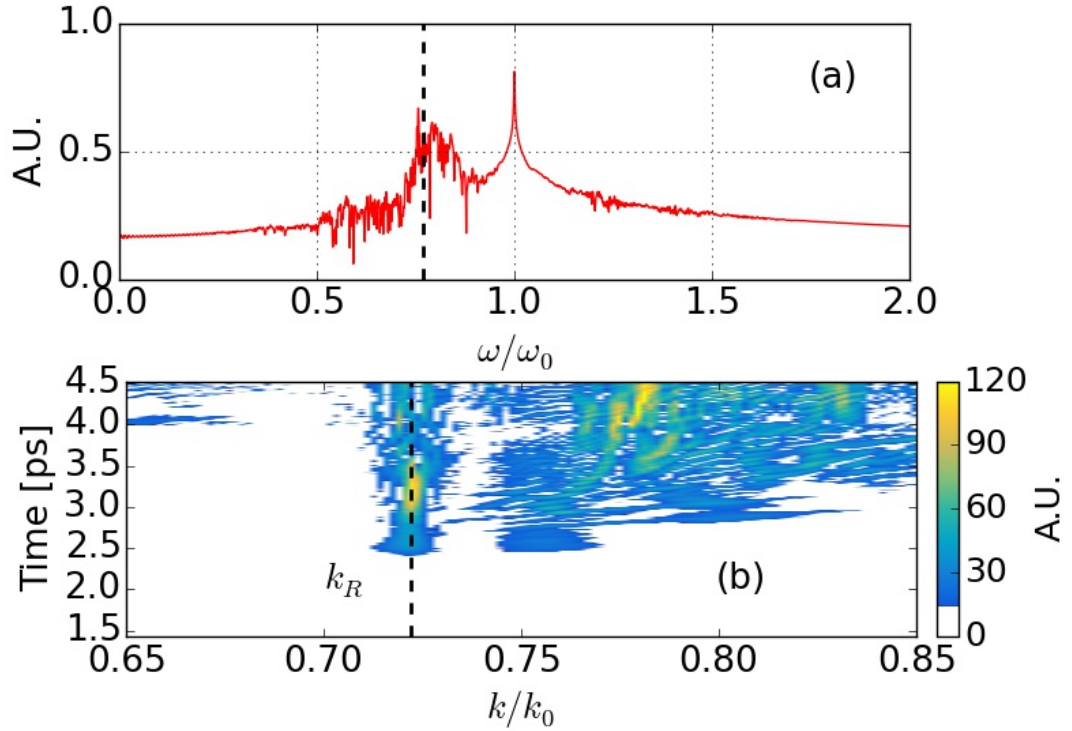


Figure 4.2: Spectrum in ω/ω_0 (a) and in k/k_0 (b) of electric field E_z , for a **constant** density profile. a) The frequency spectrum is integrated over 3.5 ps from the beginning of the simulation. The peak at $\omega/\omega_0 = 1$ corresponds to the nominal frequency of the pump laser. The black dashed line at $\omega/\omega_0 \approx 0.77$ indicates the Raman frequency in vacuum. b) The wavenumber spectrum is integrated over the entire simulation box size. The black dashed line at $k/k_0 \approx 0.72$ indicates the wavenumber of the Raman backscattered light in the plasma at a plasma density $n/n_c = 0.05$.

In Fig. 4.3(a) we consider a triangular density profile (case **triangular**), with the maximum density on the right of the box. In this case the Rosenbluth amplification factor is $A_{Ros} \approx 3.58$ (the Raman backscattered intensity of the pump will grow as $\approx e^{2A_{Ros}}$) and thus slightly above threshold ($A_{Ros,tr} \approx \pi$): we expect SRS to be significantly reduced. Fig. 4.3(a) shows the normalized intensity of the pump and

the normalized density at $t \approx 3.5$ ps (the pump maximum enters the simulation box at $t_0 \approx 3.8$ ps), at the same time as in Fig. 4.1 for the constant case. The plasma density is normalized to $n_{max}/n_c = 0.05$. No backscattering of the pump signal occurs. Similarly, a $500 \mu\text{m}$ gaussian plasma density profile with $n_{max}/n_c = 0.05$, closer to the experiments configuration, shows no pump backscatter at $t \approx 3.5$ ps, as shown in Fig. 4.3(b) (case **gaussian**). In Fig. 4.4 (a,b) we show the frequency spectrum integrated over $t \approx 3.5$ ps and the k-spectrum of the electric field E_z integrated on the simulation box and as function of time for the triangular case. The frequency spectrum confirms that there is no SRS as the pump enters, while the wave vector spectrum shows that some Raman activity develops but much weaker and later in time.

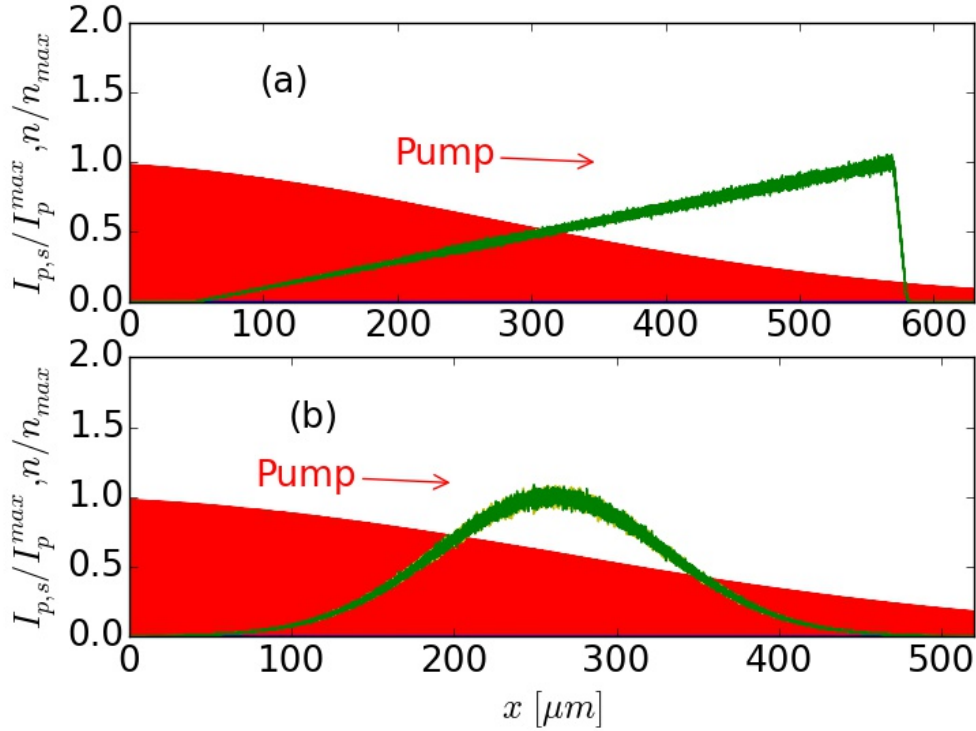


Figure 4.3: Pump intensity profile after 3.5 ps, in a **triangular** (a) and **gaussian** (b) plasma density configuration. The pump intensity, normalized to its maximum value $I_p^{max} = 10^{15} \text{W}/\text{cm}^2$ is shown in red; the green lines indicate the normalized electron density. The yellow lines (partially hidden by the green ones) are the normalized ion density. At this time the pump signal is not yet backscattered.

These simulations demonstrate that a more realistic configuration, such as a gaussian density profile or a linear ramp as could be obtained by tilted gas jets, significantly limits the Raman backscattering of the pump. This is consistent with what we found in

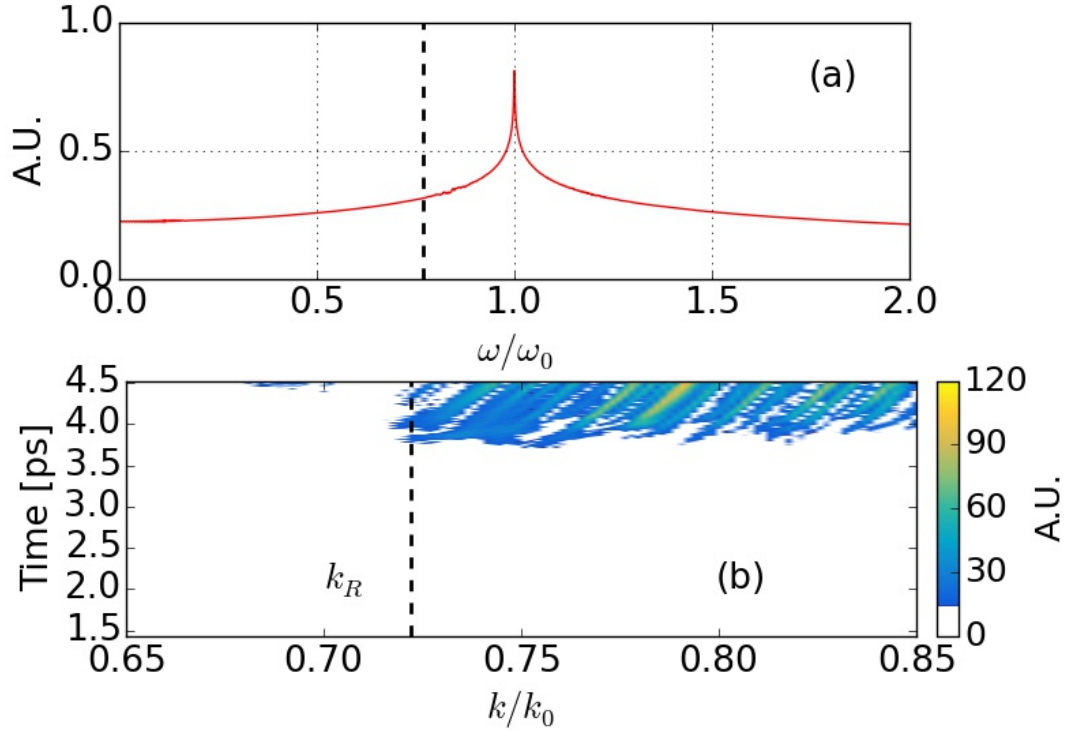


Figure 4.4: Spectrum in ω/ω_0 (a) and in k/k_0 (b) of electric field E_z , for a **triangular** density profile. a) The spectrum is integrated over 3.5 ps since the beginning of the simulation. The peak on $\omega/\omega_0 = 1$ corresponds to the nominal frequency of the pump laser. There is no signature of Raman backscattering of the pump at $\omega/\omega_0 \approx 0.77$. b) The spectrum is integrated on the entire simulation box size. The black dashed line at $k/k_0 \approx 0.72$ indicates the wavenumber of the Raman backscattered light in the plasma at a plasma density $n/n_c = 0.05$.

The Raman signal at $k/k_0 > 0.75$ is due the plasma density perturbation.

chapter 3: a decreasing profile as seen by the seed leads to a larger amplification and at the same time allows to control unwanted spontaneous instabilities (e.g. SRS). Thus even if some Raman losses are expected, they should not affect significantly the energy balance. This also suggests that an optimal delay between pump and seed should be chosen in order to minimize unwanted spontaneous backscattering. The delay of the seed with respect pump peak should not be too long so that spontaneous losses are still negligible, but short enough that it can interact a significant amount of time with the peak of the pump. Moreover it has been observed in simulations and experiments [34] that when amplification is started it quenches spontaneous Raman, thus reducing the losses, as we will discuss in Sec. 5.1.2. Finally we should point out that the Raman backscattering of the pump laser in a PIC code is often over-estimated, as it is driven by the noise of macro-particles which is proportional to $1/\sqrt{N}$ with N the number of macro particles per cell, thus the optimal delay found is likely to be shorter in simulations than in experiments.

4.3 Relative delay between the pump and seed laser pulses

As discussed in Sec.4.2, correctly choosing the relative delay between pump and seed limits the pump energy loss by SRS backscattering. This relative delay is defined as the time before the seed starts to enter the simulation box since the beginning of the simulation. The growth rate of the instability $\gamma_{sc} = \Im(\omega_{sc})$ and the downshift $\Delta\omega = Re(\omega_{sc}) = \gamma_{sc}/\sqrt{3}$ (Eq.(1.51)) depend on the local values of intensity and plasma density. In Fig. 4.5 we show the result of Eq.(1.51) for a gaussian pump of intensity $I_p = 10^{15} \text{W/cm}^2$ and duration $\text{FWHM}_p = 4.2 \text{ ps}$, and for a 1 mm gaussian plasma density profile ($\text{FWHM}_{\text{plasma}} \approx 392 \mu\text{m}$) with $n_{max}/n_c = 0.1$. The red and black lines in Fig. 4.5 (a) represent the normalized pump intensity at two different times, when the maximum of the pump reaches the left boundary and when the pump is in the middle of the simulation box, respectively; the green line is the plasma density. In Fig. 4.5(b) we show the values of growth rates $\gamma_{sc}/\omega_0 = \Im(\omega_s)/\omega_0$ for the SRS instability, as a function of the position in the plasma and for two arrival times (delay) of the pump (red and black lines respectively). When the peak of the pump is on the left side of the simulation box, $\gamma_{sc}/\omega_0 \approx 0.0025$ (red dashed line in Fig. 4.5(b)) and $\Delta\omega/\omega_0 \approx 0.0014$; when the peak of the pump is in the middle of the plasma, $\gamma_{sc}/\omega_0 \approx 0.0028$ (black dashed line in Fig. 4.5(b)) and $\Delta\omega/\omega_0 \approx 0.0017$. An optimal delay corresponds to the possibility of reaching higher growth rates, larger frequency spread and downshift of the backscattered wave . According to this linear analysis to maximize the sc-SBS coupling effect pump and seed lasers should cross at the center of the plasma density (black line in Fig. 4.5). However, the linear analysis does not take into account spontaneous

losses. In simulations we find an optimal situation when the seed crosses the peak of the pump in the first half of the plasma, in a situation that is intermediate between the two examples of Fig. 4.5, as it will be discussed. In particular, when seed and pump cross in the middle of the plasma, the effective local intensity of the pump has already been reduced by the spontaneous backscattering and results in less efficient coupling. This effect is seen as well in experiments [34][36] but the actual optimal delay is reduced with respect to simulations because the noise is artificially increased in the latter.

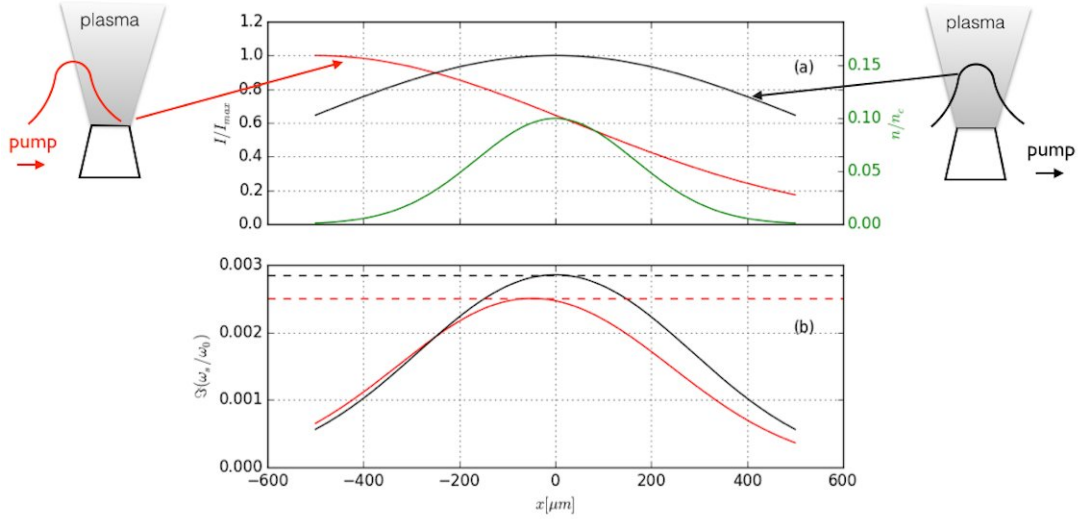


Figure 4.5: Analytical solution of Eq.(1.51) for local values of the intensity of the pump laser and of the plasma density. Fig. 4.5(a): local normalized values of the pump intensity in function of space, at two different times: when the maximum of the pump reaches the left boundary (red line) and when the pump is in the middle of the simulation box (black line). Fig. 4.5(b): values of growth rate $\gamma_{sc}/\omega_0 = \Im(\omega_s)/\omega_0$, versus the positions in the plasma and depending on the different position of the pump (red and black dashed lines correspond to $\gamma_{sc}^{-1} \approx 200$ fs and $\gamma_{sc}^{-1} \approx 178$ fs, respectively).

In Fig. 4.6(b) we schematically show this situation (case **delay 1** in following sections), where we wait $t_{delay} \approx 4$ ps before starting to launch the seed laser on the right side of the box so that the pump and seed are crossing in the middle of the plasma. The results of the corresponding PIC simulation, at the time when the amplification

of the seed has already happened ($t \approx 7.6$ ps since the beginning of the simulation), are shown in Fig. 4.6(a): the red line is the intensity of the pump normalized to its maximum, the blue line is the light traveling towards left (that includes the seed signal and spontaneous backscattering of the pump) normalized to the maximum value in intensity of the pump. The green and yellow lines are the electrons and ions density distribution normalized to $n/n_c = 0.1$.

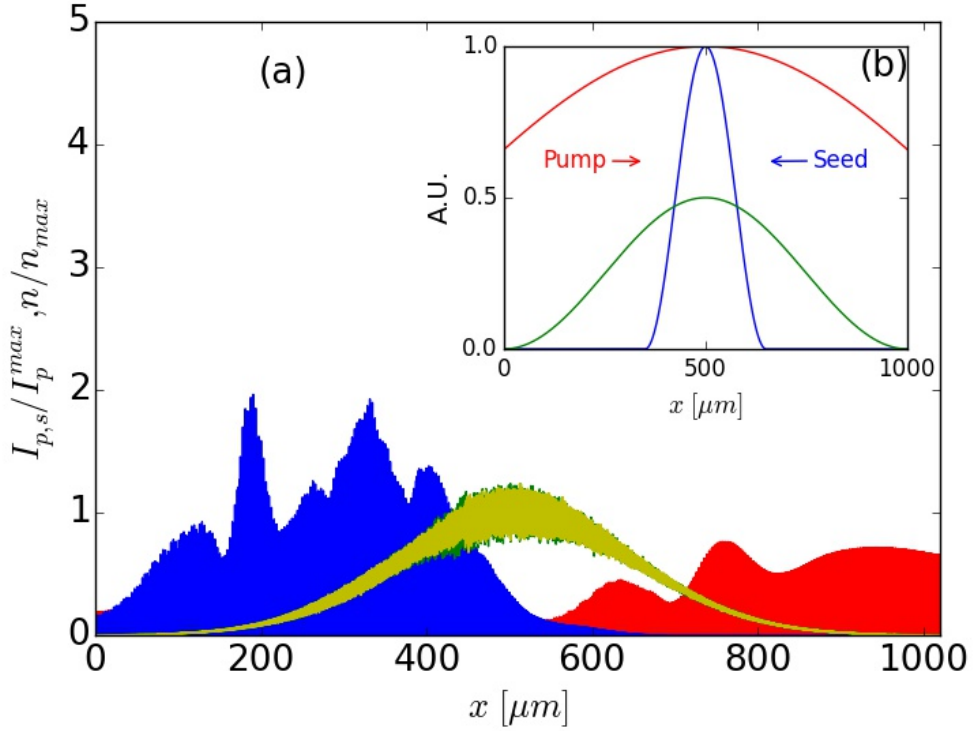


Figure 4.6: a) The red line is the intensity of the pump normalized to its maximum, the blue line is the light traveling towards left (that includes the seed signal and backscattering of the pump) normalized to the maximum value in intensity of the pump ($I_p = 10^{15} \text{W/cm}^2$). The green and yellow lines are the electron and ion density distributions normalized to $n/n_c = 0.1$. b) Intensity of the pump signal (red), of the seed signal (blue) and plasma density profile (green) in arbitrary units, in the case in which the maxima of the pulses meet in the middle of the plasma, case **delay 1**.

The gain in intensity of the seed, defined as the ratio between the maximum intensity of the seed at the exit of the simulation box (left side of Fig. 4.6(a)) and the maximum intensity at the entrance (right side of Fig. 4.6(a)), is around $I_s^{out}/I_s^{in} \approx (2 \times 10^{15} \text{W/cm}^2)/(3 \times 10^{13} \text{W/cm}^2) \approx 67$.

In the E_z frequency spectrum recorded at $x = 0 \mu m$ outside the plasma, in Fig.

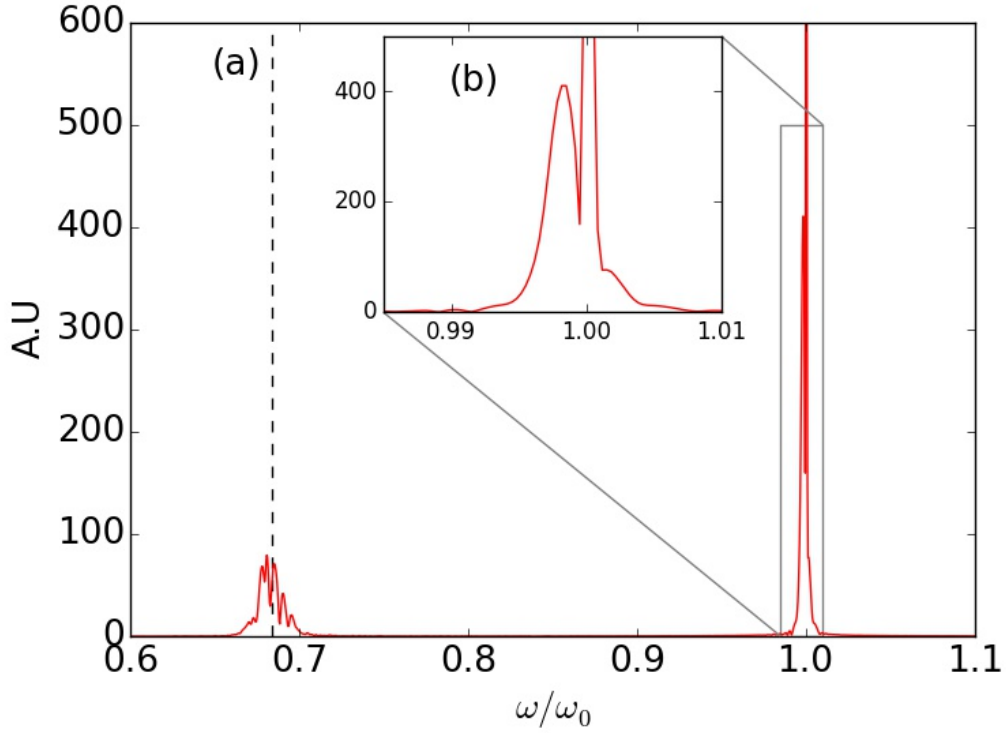


Figure 4.7: a) Spectra of electric field E_z integrated over the simulation time, for the case in which the two maxima of lasers cross in the middle of the plasma, case **delay 1**. The peak on $\omega/\omega_0 = 1$ corresponds to the nominal frequency of the pump laser. The black dashed line indicates the expected frequency values for Raman, $\omega/\omega_0 \approx 0.68$ (normalized frequency in the vacuum of the Raman backscattered light for $n/n_c = 0.1$). b) Zoom of the spectra of electric field E_z integrated over $\omega/\omega_0 = [0.985, 1.01]$. The downshift in frequency corresponding to the SBS amplification of the seed is $\Delta\omega/\omega_0 \approx 0.002$)

4.7(a), we can see that a peak in the Raman backscattered light (at $\omega/\omega_0 \approx 0.68$) is still present (black dashed line) and shows a relative large spectrum indicating that some backscattering comes not only from the peak density, but also from lower density areas. The zoom around $\omega/\omega_0 = 1$ (nominal frequency of the lasers, Fig. 4.7(b)), we show that the seed is amplified also at the strongly coupled SBS frequency ($\omega/\omega_0 \approx 0.998$); this means that the light propagating towards left (in blue in Fig. 4.6) is a mix of SBS amplified seed and Raman backscattering of the pump.

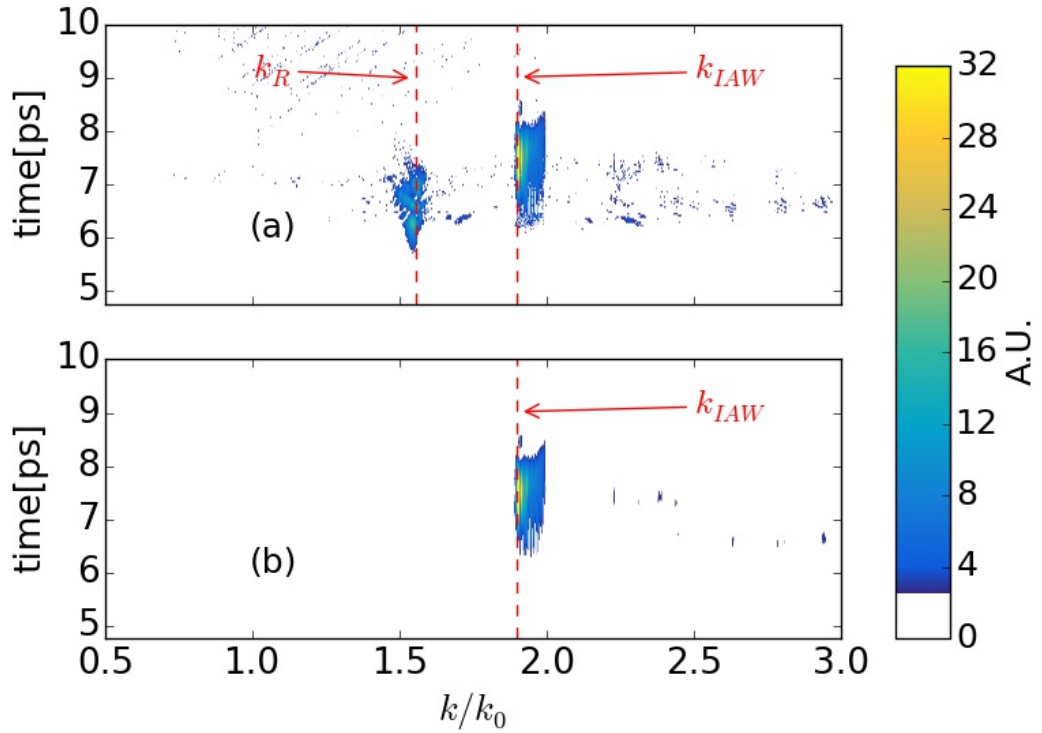


Figure 4.8: Evolution of the spectra in k/k_0 of the electron (a) and ion (b) densities for the case **delay 1**: k_R and k_{IAW} indicate the expected frequency shifts induced by the Raman and Brillouin instability, respectively (red dashed lines). The Raman backscattering starts at $t \approx 5.8$ ps, the SBS amplification after $t \approx 6.1$ ps.

In Fig. 4.8(a) and Fig. 4.8(b) we show the temporal evolution of the spectra of the electron and ion densities, respectively. The dashed red lines indicate the values of k expected for Raman (k_R) and Brillouin (k_{IAW}) backscattered light, for the maximum plasma density $n_{max}/n_c = 0.1$, defined as $k_R/k_0 \approx 1.55$ (Eq.(4.6)) and $k_{IAW}/k_0 = 2\sqrt{1 - n/n_c} \approx 1.89$. In Fig. 4.8(a) we can see that the Raman signal starts to grow around $t \approx 5.8$ ps slightly before SBS amplification takes place. This means that still part of the energy available in the pump goes in Raman backscattering, however once

the ion signal becomes strong ($t \approx 7.2$ ps) Raman is saturated.

The situation can be improved making the pulses crossing just before the Raman backscattering starts to take energy from the pump signal (case **delay 2** in following sections). To do so, the same case has been run making the seed enter the simulation box after $t_{delay} \approx 3.17$ ps from the begin of the simulation. This way the maxima of the two laser cross in the left part of the plasma density profile, at $x_{cross} \approx 320\mu\text{m}$. This situation is schematically shown in Fig. 4.9(b). In Fig. 4.9(a) we show the results from the PIC simulation for this case at $t \approx 7.6$ ps from the beginning of simulation: as before, the red line is the intensity of the pump normalized to its maximum, the blue line is the light traveling towards left (that includes the seed signal and eventual backscattering of the pump) normalized to the maximum value in intensity of the pump and the green and yellow lines are the electron and ion density distributions normalized to $n/n_c = 0.1$.

The relative gain in intensity for the seed is around $I_s^{out}/I_s^{in} \approx (4.5 \times 10^{15} \text{W/cm}^2)/(3 \times 10^{13} \text{W/cm}^2) \approx 150$; the pump pulse is well depleted and the seed conserves its original gaussian shape.

The evolution of the spectra of the electron (Fig. 4.10(a)) and ion (Fig. 4.10(b)) densities shows that the signal at the electron plasma wave frequency is reduced compared to the case of Fig. 4.8(a) and that the clear signature of Brillouin amplification is present, with the ion acoustic wave reaching larger amplitude. The first harmonic of the acoustic wave is also clearly observable (not shown here). The signature ω/ω_0 of the electric field E_z confirms this analysis (Fig. 4.11): SRS is strongly reduced and limited to highest density region (red line) while the SBS signal is larger. Consistent with the linear analysis, considering delays such that the coupling is most efficient results in the simulation in larger seed growth and frequency downshift. A similar behavior and the existence of an optimal delay was already observed in experiments [34][36]. These results confirm what find in chapter 3, where we showed that make crossing the pump and seed maxima in the first half of the plasma (as seen by the pump) leads to higher seed amplification.

4.4 Initial seed duration

The amplification process takes place in two stages: a first linear regime during which pump depletion is negligible, and a second self-similar regime in which the energy transfer becomes important and the seed gets compressed in time. During the linear regime of SBS, for the interaction of the pump with a wave packet, as in the case of the short seed pulse that we consider in this chapter, the linear solution is an integral function of an exponential times a weight function [30]. The Fourier components of

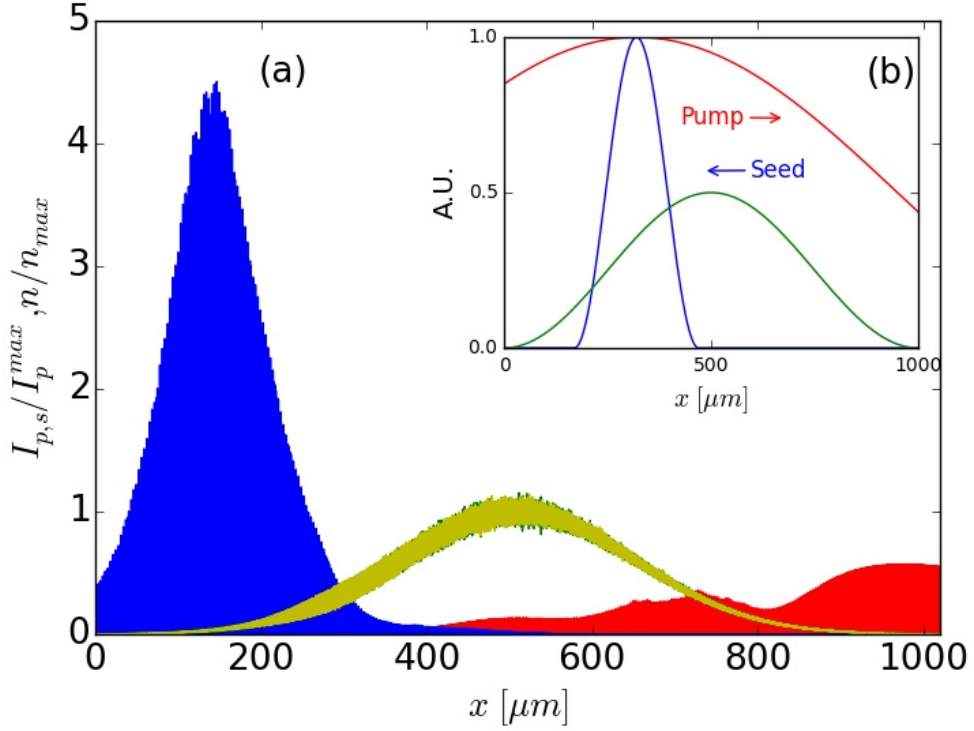


Figure 4.9: a) The red line is the intensity of the pump normalized to its maximum, the blue line amplified seed pulse traveling towards left normalized to the maximum value in intensity of the pump ($I_p = 10^{15} \text{W/cm}^2$). The green and yellow lines are the electron and ion density distributions normalized to $n/n_c = 0.1$. b) Intensity of the pump signal (red), of the pump signal (blue) and plasma density profile (green) in arbitrary units, in the case in which the maxima of the pulses meet at $x \approx 320 \mu m$, case delay 2.

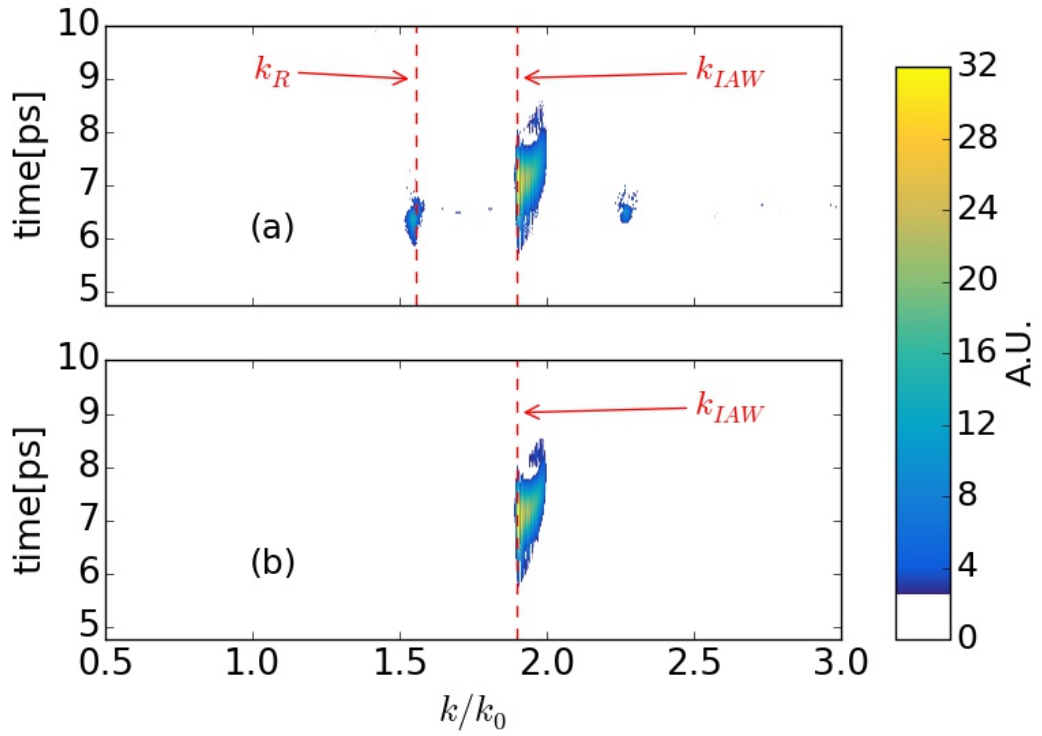


Figure 4.10: Evolution of the spectra in k/k_0 of the electron (a) and ion (b) densities for the case **delay 2**: k_R and k_{IAW} indicate the expected frequency shifts induced by the Raman and Brillouin instability, respectively (red dashed lines). The Raman backscattering starts at $t \approx 5.8$ ps, but it disappears when the Brillouin amplification takes place.

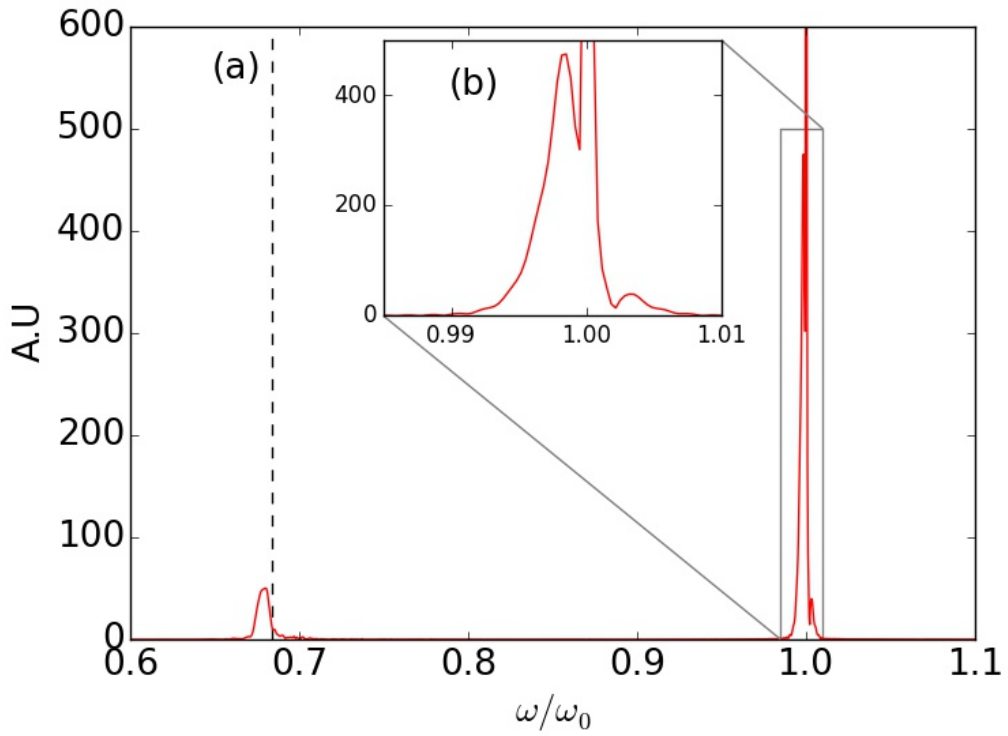


Figure 4.11: Spectra of electric field E_z integrated over the entire simulation time ($t_{sim} \approx 10$ ps, for a relative delay of $t_{delay} \approx 3.17$ ps, case **delay 2**). The peak at $\omega/\omega_0 = 1$ corresponds to the nominal frequency of the pump laser. The zoom box shows the frequency downshift due to the SBS amplification of the seed.

the various wave-vectors grow unevenly, resulting in a longer seed. A short seed has a broad k spectrum and only a narrow portion of this spectrum can be amplified. If the initial seed duration is shorter than the shortest local value of γ_{sc}^{-1} the seed will develop a tail that will be amplified [30][42]. On the other hand, if the initial seed duration is of the order or longer than γ_{sc}^{-1} , then the seed enters directly in the self-similar regime, as shown in Sec. 4.3 (Fig. 4.9). In both cases the final amplification intensity and energy exchange is comparable as the seed duration adapts to the self-similar solution as will be discussed in the following paragraph. We can summarize this by saying that as long as the initial seed intensity is less than the pump intensity, amplification is roughly independent of the initial seed duration.

It is interesting to notice that once the sc-SBS amplification is described by the self-similar solution, the seed dimensionless intensity $a_s^2 \equiv 0.72 \times 10^{-18} I_s [\text{W}/\text{cm}^2] \lambda_0^2 [\mu\text{m}^2]$ and the seed duration τ_s are related. This can be shown by considering for simplicity a case of full pump depletion, for a pump of normalized intensity a_0^2 and duration τ_p . With these units we find $\gamma_{sc} = \sqrt{3}/2 [a_0 \frac{v_g}{c} \omega_{pi} \sqrt{\omega_0}]^{(2/3)}$. A first relation, in the case of full pump depletion, is simply given by the energy balance at the end of the interaction : $a_s^2 \tau_s = a_0^2 \tau_p$. To find another relation, let us now consider the growth of the seed according to the self similar solution [27] : $a_s = \tau^{3/4} A_s(\xi)$, with $\tau = \gamma_{sc} t$ and $\xi = \sqrt{\gamma_{sc} t} \gamma_{sc} x' / v_g$, and $x' = x + v_g t - L_{pl}$ the spatial coordinate in the seed reference frame. According to this solution the seed's typical time scale of growth is γ_{sc}^{-1} and the maximum amplitude grows with time to the power 3/4. The function $A_s(\xi)$ can be found numerically [27] for a given boundary condition, and it is a 'bell'-shaped curve, such that it reaches a maximum amplitude at $\xi_{max} \sim 6 - 7$, with a typical width $\Delta\xi_W \sim 2 - 3$, characteristic of the seed duration in normalized units. The exact values depend on the boundary conditions, and in the following we assume that $\Delta\xi_W$ is a constant of order one. To relate this explicitly to the seed duration we can consider the definition of ξ , and define $\Delta\xi_W = \sqrt{\gamma_{sc} t} \gamma_{sc} \Delta x' / v_g$. According to this $\Delta x'$ is the space occupied by the seed during its propagation, that is related to its finite duration $\Delta x' \approx v_g \tau_s$, so that finally $\Delta\xi_W \approx \sqrt{\gamma_{sc} t} \gamma_{sc} \tau_s$. Since $\Delta\xi_W$ is a constant, this results tell us that the seed duration shrinks as $\propto 1/\sqrt{\gamma_{sc} t}$ (contraction associated to the amplification). At the end of the interaction ($t = \tau_p$ the seed duration will satisfy the condition $\Delta\xi_W = \sqrt{\tau_p} \gamma_{sc}^{3/2} \tau_s$, thus giving a relation between τ_p, τ_s and a_0 . Solving for τ_p and replacing in the energy balance equation, the dependence on a_0 drops out and we find a condition relating a_s and τ_s

$$a_s^2 \tau_s^3 = \Delta\xi_W^2 \left(\frac{2}{\sqrt{3}} \right)^3 \frac{c^2}{v_g^2 \omega_{pi}^2 \omega_0}. \quad (4.7)$$

A similar argument was applied in Ref.s [40][38] at initial or intermediate times, by

considering that only a fraction (η) of the energy has been exchanged between pump and seed. The final result being independent of the energy fraction η the relation Eq. (4.7) was considered valid at any stage of the amplification. However this argument does not apply in the linear phase, thus it cannot be used to deduce the initial seed duration. The initial seed duration, as described earlier, will adapt in the linear stage so that once the depletion regime is reached the growth will be roughly independent of the initial seed value (see also next section, where we explicitly calculate the energy exchange) [30]. This is confirmed by a set of PIC simulations where we varied the initial seed duration, as well as by earlier results [30]. In this section we present a PIC simulation in which the parameters are the same as presented in Sec 4.1, with the optimal relative delay between the pump and seed lasers $t_{delay} \approx 3.17$ ps (as found in Sec. 4.3) but with an initial duration of the seed of $FWHM_{seed} = 100$ fs instead of 500 fs (case **short**). In Fig. 4.12(a) we show the results of the simulation at $t \approx 6.5$ ps from the beginning of the simulation. In the zoom of the intensities at $x = [100,350]$ μm (Fig. 4.12(b)) we see that seed signal itself is not amplified: the amplification happens behind the seed laser, creating a broad secondary pulse. The final duration of the final amplified pulse 4.12(c) is $FWHM_{out}^{seed} \approx 420$ fs $\approx 2 \times \gamma_{sc}^{-1}$ at $t \approx 7.5$ ps from the beginning of the simulation (178 fs $< \gamma_{sc}^{-1} < 200$ fs in Fig. 4.5). As shown in the 4.12(c) the final intensity is comparable but smaller than the **delay 2** case (Fig. 4.9); however with a longer plasma the same intensity and shape of the solution of Fig. 4.9 are expected [30]. In particular a seed duration that initially is a fraction of γ_{sc}^{-1} can lead to slightly higher amplification factors, the only drawback being that since the linear phase lasts a bit longer, as the pulse needs to adapt, if the initial seed has duration much smaller than γ_{sc}^{-1} the plasma interaction length needs to be somewhat longer. Notice that if we apply the analysis of Ref.s [40][38] to our value of seed intensity, $FWHM_{s_{opt}} \approx 1054$ fs; however we showed in previous sections that a seed with an initial $FWHM_s = 500$ fs is very well amplified, confirming that the important parameter in the seed amplification mechanism is the comparison with γ_{sc} , at least in the first part of the amplification. It is interesting to use the estimate above (Eq. (4.7)) to estimate the expected duration in the case where amplification by the self similar model holds. Eq. (1.47)(1.48)(1.49) do not take in account relativistic effects and coupling with electron plasma wave [41]. We consider then the upper limit of validity of these equations when the seed reaches relativistic intensities, $a_s = 1$. If we plug this value in Eq. (4.7), we find the final seed duration when such intensities are reached.

$$\tau_{s,rel}\omega_0 = \frac{2}{\sqrt{3}} \frac{\Delta\xi_W^{2/3}}{(1 - n_e/n_c)^{1/3}(\omega_{pi}/\omega_0)^{2/3}}. \quad (4.8)$$

and $\frac{2}{\sqrt{3}}\Delta\xi_W^{2/3} \approx 2$ for the relevant case.

If we consider hydrogen ($Z = 1$), taking $n_e/n_c = 0.3$ in the formula above, we find that $\tau_{s,rel}\omega_0 \approx 38$, if we consider $n_e/n_c = 0.05$ we find that $\tau_{s,rel}\omega_0 \approx 108$. In all cases, this suggests that seed duration after amplification will be short, from a few to a few tens of laser cycles.

Thus if we consider a multi-stage amplification scheme or simulations where the initial seed intensity is already larger than the pump and close to the relativistic domain (assuming that it has been successfully amplified in the self-similar regime in a previous stage), we have to consider very short pulses. However it has been shown that the electron dynamics becomes dominant when the intensity gets close to the relativistic condition, and the pure sc-SBS self-similar solution does not reproduce anymore the dynamic of the energy exchange [33][41][42][28]. Self focusing effect at this high intensity plays also an important role, so that further two and three dimensional studies are required in order to optimize amplification in this regime.

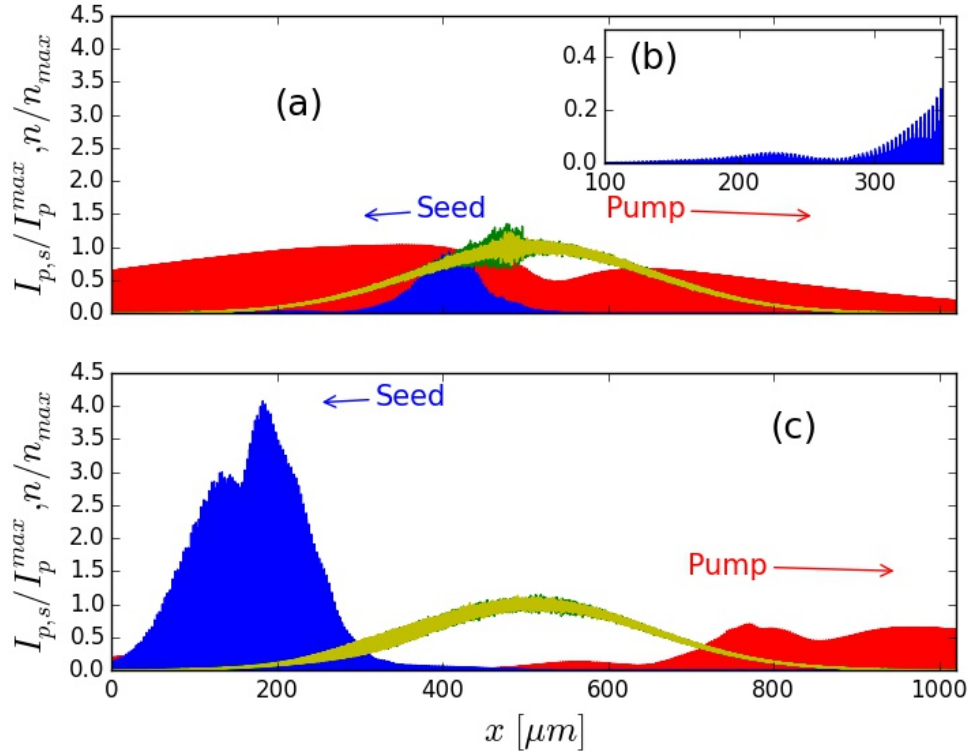


Figure 4.12: The red line is the intensity of the pump normalized to its maximum, the blue line is the amplified seed pulse propagating towards left normalized to the maximum value in intensity of the pump ($I_p = 10^{15} \text{W/cm}^2$), for the case **short** at $t \approx 6.5$ ps (a) and $t \approx 7.5$ ps (c) (the pump maximum enters the box at $t_0 \approx 5.35$ ps). The green and yellow lines are the electron and ion density distributions normalized to $n/n_c = 0.1$. b) Zoom of the seed intensity for $x = [100, 350]$ μm at $t \approx 6.5$ ps.

4.5 Energy transfer and final duration of the seed

In this section we summarize the results of the previous simulations in terms of energy gain and final duration of the seed.

Table 4.1: Overview of the parameters of the numerical simulations discussed in this chapter. $\text{FWHM}_{\text{in}}^{\text{seed}}$ and $\text{FWHM}_{\text{out}}^{\text{seed}}$ are expressed in fs, t_{delay} is in unit of ps. The plasma length and the crossing point are expressed in μm . $Q_{\text{out}}^{\text{tot}}$ and $Q_{\text{out}}^{\text{seed}}$ are in units of J/cm^2 and the intensity I_{out} in units of $10^{15}\text{W}/\text{cm}^2$.

run	density profile	n/n_c	$\text{FWHM}_{\text{in}}^{\text{seed}}$	plasma length	crossing point	t_{delay}	$Q_{\text{out}}^{\text{tot}} / Q_{\text{out}}^{\text{seed}}$	% Q_{pump}	$\text{FWHM}_{\text{out}}^{\text{seed}}$	$I_{\text{out}} \times 10^{15}$
I	constant	0.05	500	500	250	4	2300/1500	50	600	2.5
II	triangular	0.05	500	500	250	4	2480/2320	77	660	3.1
III	gaussian	0.1	500	1000(392)	500	4	2530/2400	80	1330	2.0
IV	gaussian	0.1	500	1000(392)	320	3.17	2882/2882	96	330	4.5
V	gaussian	0.1	100	1000(392)	320	3.17	2088/2088	70	420	4.0

In Table 4.1 *density profile* denotes the shape of the plasma considered in each simulation, n/n_c is the peak value of the density, $\text{FWHM}_{\text{in}}^{\text{seed}}$ and $\text{FWHM}_{\text{out}}^{\text{seed}}$ are the initial and final seed durations at full width half maximum in intensity, respectively. For each *plasma length* (the $\text{FWHM}_{\text{plasma}}$ is indicated in parenthesis for the run with gaussian density profiles), the *crossing point* is the position in the simulation where the pump and seed maxima are meeting. t_{delay} is the time before the seed starts to enter the simulation box since the beginning of the simulation, as defined at the beginning of Sec.4.3. $Q_{\text{out}}^{\text{tot}}$ is the energy fluence of the backscattered electromagnetic wave (that includes the backscattered light of the pump signal and the amplified seed), $Q_{\text{out}}^{\text{seed}}$ is the gain in energy fluence of the seed pulse and $\% Q_{\text{pump}} = 100 \times Q_{\text{out}}^{\text{seed}} / Q_p$ is the percentage of the pump energy fluence backscattered in the seed pulse, where $Q_p \approx 2.9\text{kJ}/\text{cm}^2$ is the initial pump energy fluence. $Q_{\text{out}}^{\text{tot}} - Q_{\text{out}}^{\text{seed}}$ is the energy fluence associated to the spontaneous backscattering. I_{out} is the peak intensity of the amplified seed. In the case of a constant density profile (Sec. 4.2, **constant** case, run I in Table 4.1) the energy fluence of the light traveling towards the left is high, almost 76 % of the initial pump laser energy: the energy fluence transferred to the seed is ≈ 50 % of the pump energy fluence and its final duration $\text{FWHM}_{\text{out}}^{\text{seed}} \approx 1.2 \times \text{FWHM}_{\text{in}}^{\text{seed}}$, as shown in Fig. 4.13. The difference in energy fluence between $Q_{\text{out}}^{\text{tot}}$ and $Q_{\text{out}}^{\text{seed}}$ is due to the Raman backscattering of the pump. In Fig. 4.14 we show the temporal evolution of the Fourier transform in space of the electron density: it is interesting to point out that at $t \approx 6$ ps from the beginning of the simulation there is a signal at $k_{FR}/k_0 = \sqrt{n/n_c}$ that is the corresponding wave-vector for the electron plasma wave due to the Forward Raman scattering of the pump. It was suggested [38] [40] that at values of density of the order of $n/n_c = 0.05 - 0.1$ the Raman competition, and in particular Forward Raman, would be too detrimental to allow sc-SBS amplification. However, as we showed in this chapter and in previous publications [33], if the delay is chosen appropriately

and the plasma is not completely homogeneous, we can have successful SBS amplification. In our simulations we observe Forward Raman scattering only in the homogenous case and quite late in time. This is shown in Fig. 4.15 where we see that this signal starts to be important when the SBS amplification (k_{IAW}) has already occurred. In the case of a triangular density profile (Sec. 4.2, **triangular** case, run I in Table 4.1) the energy fluence transmitted to the seed is $\approx 77\%$. For both the **constant** and **triangular** simulation, the plasma length is $500\ \mu m$ and the pump and seed laser beams are crossing in the middle of the plasma. For the run III in Table 4.1 (case **delay 1** in Sec. 4.3) the pump and seed signals are meeting in the middle of the plasma: the backscattered light takes $\approx 84\%$ of the pump energy fluence. The best case is the run IV in Table 4.1 (case **delay 2** in Sec 4.3): not only $\approx 96\%$ of the pump energy fluence goes into amplifying the seed signal, but the final duration of the seed is shorter than its initial duration: this means that the seed efficiently reaches the non linear amplification phase. The run V in Table 4.1 (case **short** in Sec. 4.4) is particular: the seed triggers amplification on its tail as discussed in the previous section. Almost 70% of the pump energy fluence is going directly to this secondary pulse: its final duration in FWHM is ≈ 420 fs. The seed final peak intensity is comparable with the one of run IV, but its energy fluence is smaller as the final shape is different: the peak intensity is, in this case, the intensity of the secondary pulse. Has shown by Lehmann et al. [30] by studying the self-similar solution, this latter case, for a long interaction time and slightly larger plasmas, is expected to shrink and reach even higher intensities and energy transfer efficiency.

In all the presented simulations, the seed-pump coupling is effective and leads to large amplitude electron and ion density fluctuations. As already pointed out in the past [27][43] and discussed in more detail in recent publications [37][32], the main amplification pulse is not however affected by non-linearity of the ion-acoustic waves as the large density fluctuations grow behind the seed. However, behind the pulse a very regular grating forms so that the coupling leading to SBS amplification has also been suggested as a way to dynamically create plasma gratings [27][43][32]. When the density fluctuations become very large, kinetic and fluid non-linearities appear: as a result quasi-neutrality does not hold anymore and, as we can see in Fig. 4.13 and Fig. 4.15, the ion density fluctuations reach higher level than the electron one. Notice that this is not observed in the other density figures because those images are taken at earlier time, too close to the first peak amplification. This is confirmed by [32], where also electron temperature effects are studied and it is shown that non-linear kinetic effects mainly influence the tail of the amplified pulse.

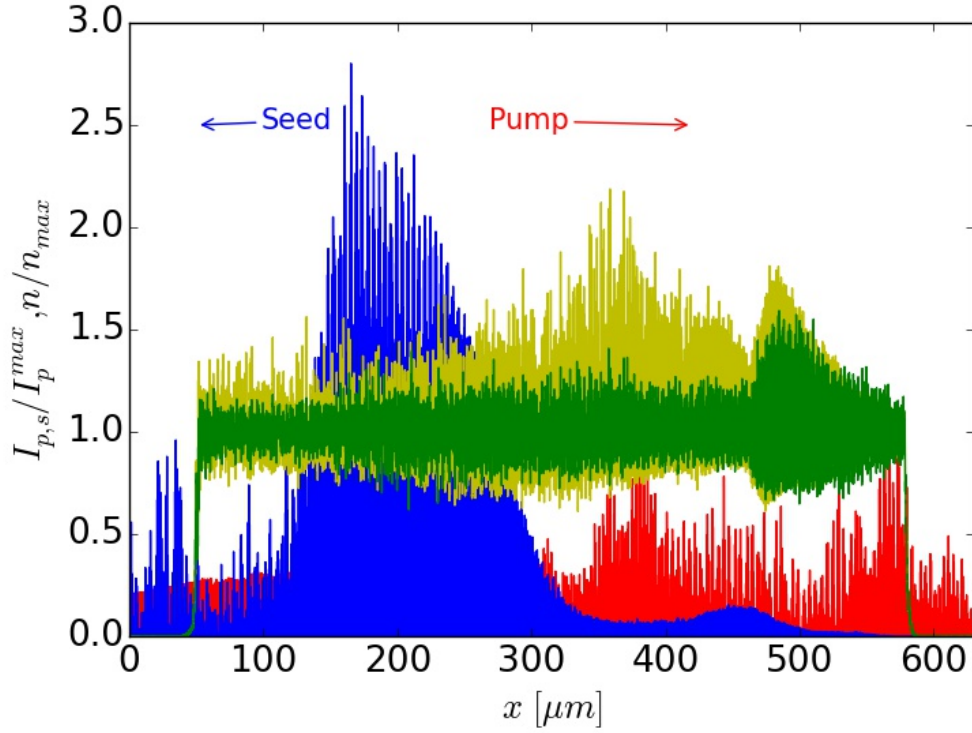


Figure 4.13: Amplified backscattered light at the exit of the plasma, for the **constant** case at $t \approx 6.39$ ps (run I in Table 4.1). The red line is the intensity of the pump normalized to its maximum, the blue line is the amplified light traveling towards left normalized to the maximum value in intensity of the pump ($I_p = 10^{15} \text{W/cm}^2$). The green and yellow lines are the electrons and ions density distribution normalized to $n/n_c = 0.1$.

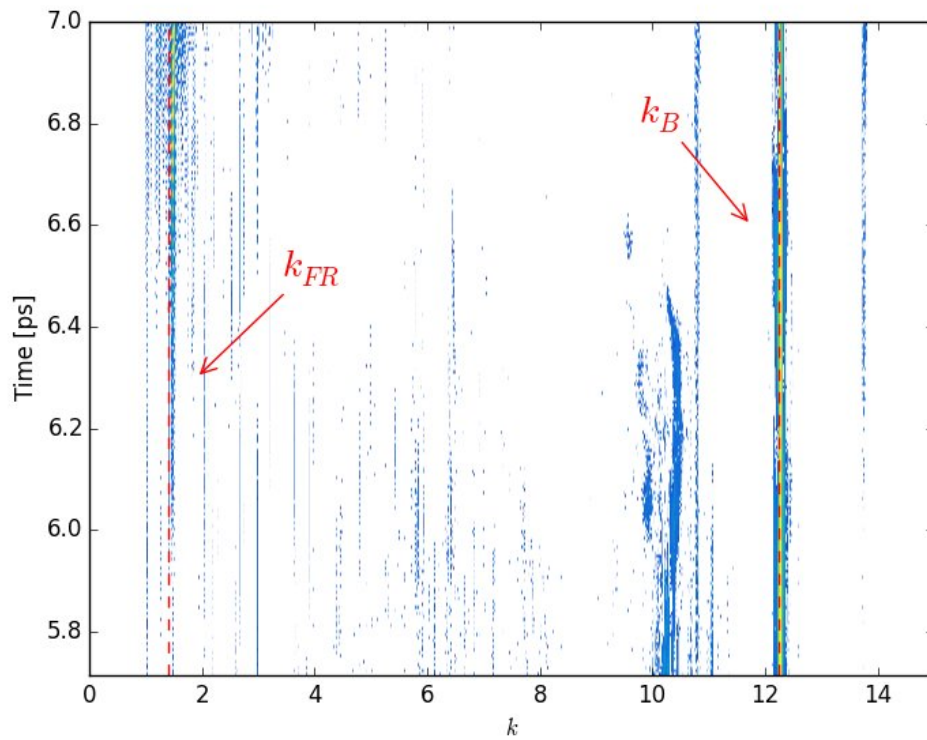


Figure 4.14: Temporal evolution of the spectra of the electron density: k_{FR} and k_{IAW} indicate the expected frequency for the Forward Raman scattering and SBS backscatter instabilities, respectively (red lines). The Forward Raman scattering starts at $t \approx 6$ ps

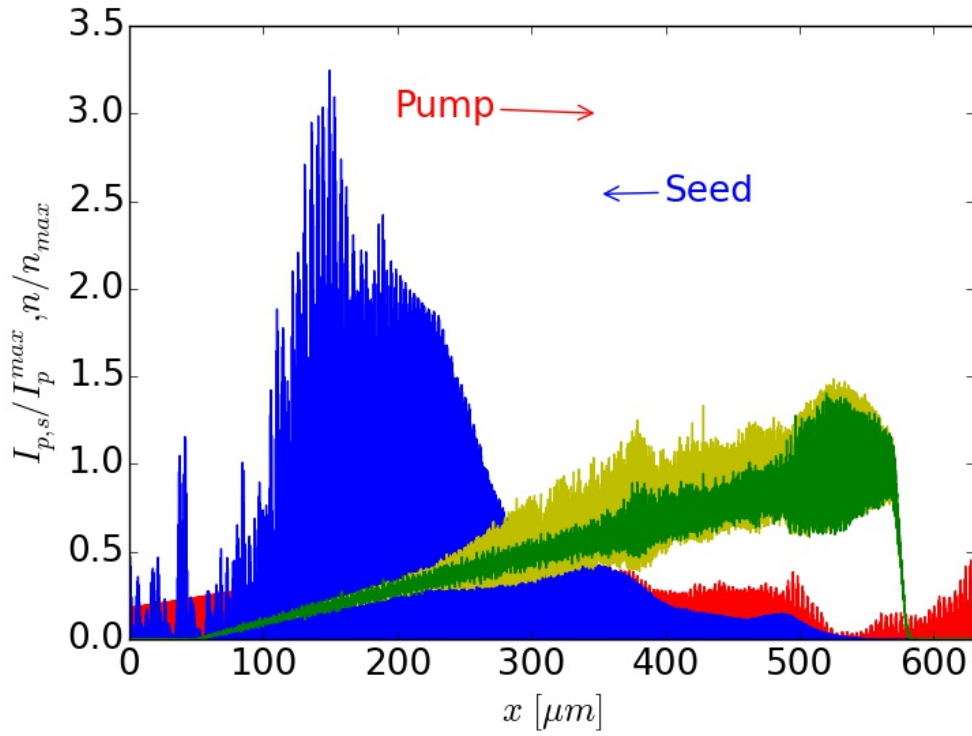


Figure 4.15: Amplified backscattered light at the exit of the plasma, for the **triangular** case at $t \approx 6.5$ ps (run II in Table 4.1). The red line is the intensity of the pump normalized to its maximum, the blue line is the amplified light traveling towards left normalized to the maximum value in intensity of the pump ($I_p = 10^{15} \text{W/cm}^2$). The yellow lines are the electrons and ions density distribution normalized to $n/n_c = 0.1$.

4.6 Conclusions

This chapter presents a systematic parameter study of the effect of plasma density profile, pump and seed time delay and seed temporal shape on sc-SBS amplification of a seed by a pump in a two contra-propagative laser configuration. As a results of our study, one dimensional PIC simulations appear as a necessary tool to describe most of the competing process and non-linearities intervening in the amplification mechanism. In particular, we find that plasma shaping allows to partially control SRS affecting also the energy transfer. Typical experimental profiles of plasma produced from gas jet have gaussian shape and already help reducing significantly the spontaneous SRS. The optimal delay is a trade-off of amplification efficiency and backscattering of the pump. This is an important parameter as proved by simulations and experiments [34][36], and the exact optimal delay has to be experimentally assessed for each particular configuration with a systematic scan of pump-seed synchronization.

Spectral analysis of the seed allows to evaluate the quality of the amplification process. The local linear analysis gives the right order of magnitude for the sc-SBS and SRS spectra. However PIC simulations and experiments [34][36] show larger downshifts and broader spectra than predicted by the linear theory, as well as asymmetric spectra. Amplification of a short seed is possible, however depending if the seed is low or high (relativistic) intensity, the amplification mechanism will be different. In the case of low intensity the seed stretches before entering in the self-similar regime. At high intensities the electron contribution is more important even if the matching condition for SRS is not satisfied [33]. Moreover amplification from low to very high intensities in a single pass is very challenging experimentally and theoretically because of the competing effects discussed in this chapter. A possible solution would be to consider a multi-stage process where the pulse amplified by a pump in a plasma cell interacts with a second pump in a nearby cell. Once the seed is amplified to almost relativistic intensities, issues related to multidimensional effects such as self-focusing and filamentation become important and need to be addressed in more detail in further studies.

Chapter 5

Recent experiments on strong coupling SBS amplification and comparison with one dimensional PIC simulations

In this chapter we shortly resume the results on some of the recent experiment carried out at LULI demonstrating the feasibility of the amplification of short laser pulses using strong coupling Stimulated Brillouin Scattering. We show then the results of some PIC simulations to corroborate the conclusions given on recent SBS amplification experiments.

As anticipated in the introduction of this thesis, because of the faster response of an electron plasma wave, Stimulated Raman Amplification (SRA) has been initially more investigated theoretically and experimentally [13] for amplification of sub-picosecond laser pulses. One of the saturation mechanisms of SRA is the electron plasma wave breaking, limiting the maximum pump intensity [48] [49]. Achieving high energy transfers then requires large transverse beam sizes and thus, because of the required frequency-matching conditions, homogeneous plasmas over a large interaction volume. Therefore, more attention has been recently directed towards Stimulated Brillouin Amplification (SBA), in particular towards its strongly coupled (SC) SBA limit [27][26][36]. The first experimental demonstration of short light pulse amplification using sc-SBS has been given by L.Lancia et al. in [36]. In this experiments relative amplification factors of up to 32 for the transmitted seed pulse were obtained by crossing temporally coincident pulses with identical polarization in an Argon plasma with a density of $0.1 n_c$. The pump laser has been compressed to a pulse duration of $3.5 ps$, leading to a maximum intensity of $I_p = 6.5 \times 10^{16} W/cm^2$: the seed was $400 fs$ long with a peak intensity of

$I_s = 5 \times 10^{15} \text{W/cm}^2$. Fig. (5.1) shows the amplified seed spectra and focal spots from the L.Lancia's et al. work [36]. This first experiment, even in not optimal conditions, was intended as a proof-of-principle demonstration of sc-SBS amplification.

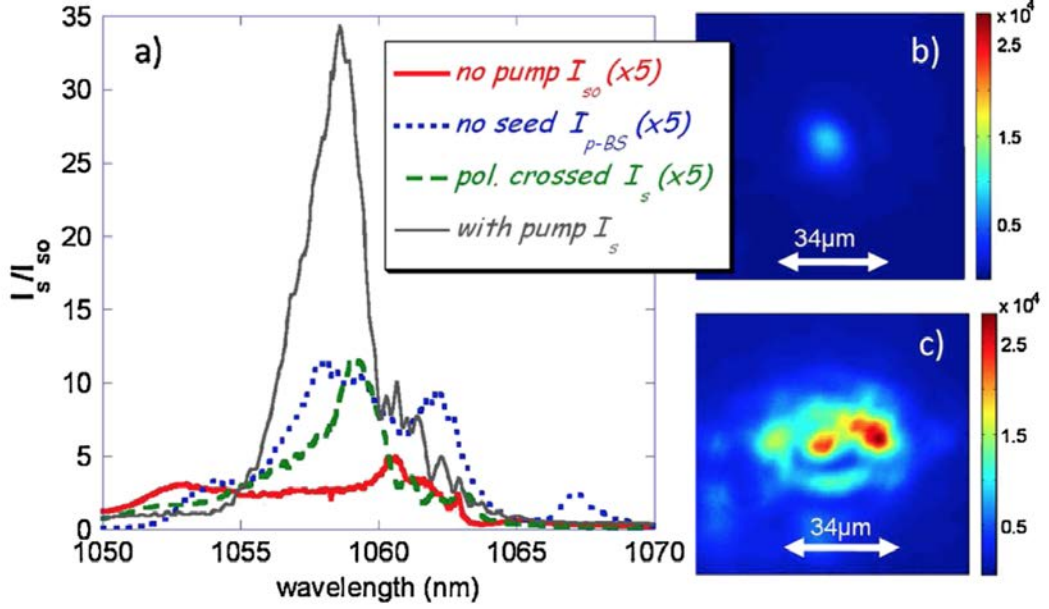


Figure 5.1: From 2010 L.Lancia's paper [36]. (a) Transmitted signal recorder on the seed spectrometer, at the exit of an Ar plasma with density $n_e = 0.1n_c$. Except for the amplified signal, I_s , all spectra have been multiplied by a factor of 5 for visibility. The focal spot of the seed signal transmitted through the plasma without (b) and with (c) the pump beam. Images are displayed with the same color scale.

A second paper from Lancia et al. [34] has been recently published: in this paper they report the first observation of signatures of the transition from linear to self-similar regime of strongly coupled SBS. In the following, we briefly resume the main experimental results obtained in [34] and we make a comparison with the results from some one dimensional Particle-in-Cell simulations that are also presented in [34].

5.1 Experiments and simulations comparison

In [34] three CPA pulses, of wavelength $\lambda_0 = 1058 \text{ nm}$ and 6 nm bandwidth were used: an ionizing beam generating the plasma from a supersonic hydrogen gas jet (orange line in Fig. 5.2), a 6 J pump (blue line in Fig. 5.2) stretched to 4 ps leading to a peak intensity of $I_p = 2 \times 10^{15} \text{W/cm}^2$ and a seed beam (green line in Fig. 5.2) with a 700 fs duration at FWHM and intensity of $I_s = 3 \times 10^{13} \text{W/cm}^2$. The plasma density profile was Gaussian with a $500 \mu\text{m}$ FWHM along the propagation axis and a

maximum value of $n_{max}/n_c = 0.1$. In these experimental conditions, the intensity of the seed pulse were amplified up to a factor of 5. For the one dimensional PIC simulations we have considered the same parameters in terms of lasers intensity, durations and plasma density. In Fig.(5.3) we show the results of the amplification from the PIC simulation: in blue we indicate the intensity of the amplified seed normalized to the pump initial maximum intensity $I_p^{max} = 2 \times 10^{15} W/cm^2$ and in red the pump intensity. As it is possible to see, the pump laser is very well depleted and the seed amplification is up to 283 its initial intensity. As one dimensional PIC simulations account for all possible kinetic and nonlinear effects, discrepancy between experimental values of amplification and the PIC simulations would be attributed, in our understanding, to experimental uncertainties with plasma and lasers characterization (laser beam quality, plasma density value). We focus here on the comparison between the spectra of the amplified seed for the simulations and the experiments is way more important than a direct comparison in terms of energy transfer and final intensities.

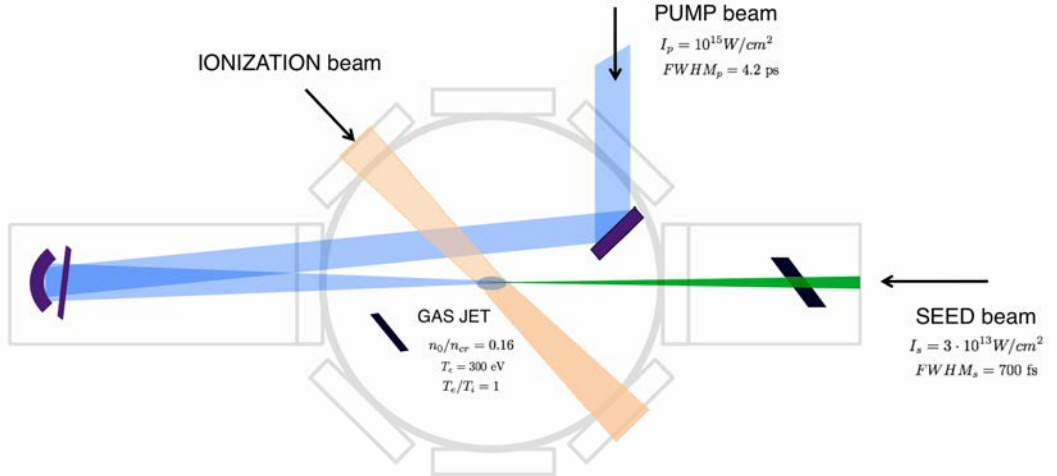


Figure 5.2: Experimental set-up of the experiments presented in [34]

5.1.1 Comparison between spectra of the amplified seed from simulations and experiments

In Chapter 4 we showed how the choice of the relative delay between seed and pump laser is a crucial parameter to control the SBS amplification in competition with the spontaneous Raman backscattering of the pump. In the experiments [34] was ale explored explored the seed amplification in function of the relative delay between the two lasers beams. In [34] the relative delay Δt is defined as following: if $\Delta t = 0$ the pump and seed beams are crossing exactly in the middle of the plasma (purple solid line in

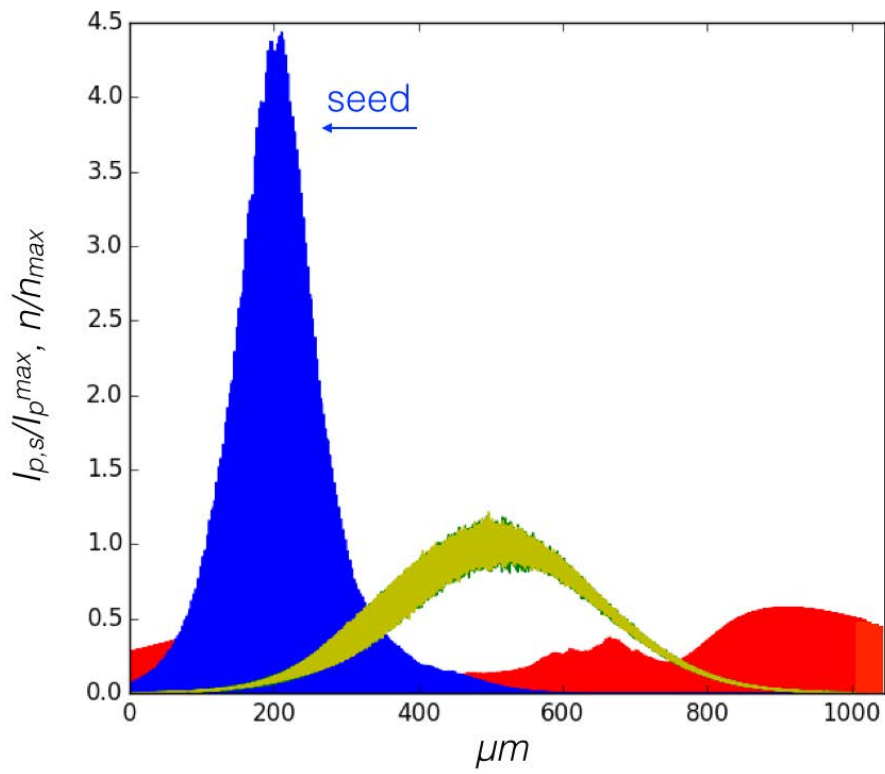


Figure 5.3: The red surface indicates the intensity of the pump normalized to its maximum ($I_p^{max} = 2 \times 10^{15} W/cm^2$), the blue one is the amplified seed pulse propagating towards left normalized to the maximum value in intensity of the pump.

Fig.(5.4)). If $\Delta t < 0$ (for example $\Delta t = -6$ ps, green solid line in Fig.(5.4)) the pump arrives at the plasma center before the seed; the opposite if $\Delta t > 0$ ($\Delta t = +3$ ps, yellow solid line in Fig.(5.4)). Changing the relative delay between pump and seed one can thus explore the pump-seed coupling from linear to self-similar regimes, while keeping the same plasma and laser parameters (focal spot size, laser energy, pulse duration), and avoid triggering or modifying other limiting mechanisms such as beam filamentation or wave breaking. In Fig.(5.7) we show the seed energy gain (blue circles, left scale) and the backscattered Raman energy from the pump into the seed propagation direction (green squares, right scale), as a function of Δt . The energy gain is defined as the ratio between the signal at the seed exit of the plasma, and the signal of the seed propagating in vacuum, both normalized to the seed incident energy. Two types of gain measurement are shown: they are obtained from the integration (i) of the CCD images of the focal spot (2D calorimetry, full circles) and (ii) of the spectrum (1D calorimetry, empty circles). For the 1D calorimetry only a vertical slice of the focal spot is selected through the spectrometer slit. The slightly higher gain, recorded from the 1D calorimetry, suggests that a higher amplification occurs in the central part of the beam. In Fig.(5.5)(a) we show the comparison between the energy spectra of the seed in function on different different delay with the spectra on the seed electric field from the PIC simulations Fig.(5.5)(b). In particular, for the simulations results we show the Fourier transforms of the seed electric field after interaction, for two different pump-seed delays; the spectrum is only shown over the interval of interest. As experimentally observed, at the delay t_{opt} giving the maximum amplification, also correspond the largest redshift and spectral width. Both the amplitude of the redshift and the spectral broadening are in relatively good agreement with the experiment. It is interesting to compare the seed spectrum obtained from PIC simulations of Fig.(5.5)(b) with the values of downshifts given by the sc-SBS linear theory (Fig.(5.6)(b)) for different position of the pump in the plasma (Fig.(5.6)(a)). The broadening and the redshift of the amplified signal is in the same direction than what predicted by linear theory, but, if we compare the values of redshift we find for the linear solution that $\frac{\Delta\omega}{\omega_0} \approx 0.0017 \rightarrow \Delta\lambda_{lin} \approx 1.8$ nm when the pump is in the middle of the plasma and the downshift is maximized (black lines in Fig.(Fig.(5.6)). From the PIC simulations for the best case at t_{opt} we have $\Delta\lambda_{PIC} \approx 2.86$ nm: this means that with the PIC simulations we entered the self-similar regime where the pump is depleted and the linear theory is not valid anymore. Looking at the good agreement between spectra from PIC simulations and experiments (Fig.(5.5)), with can deduce that in the experiments the seed explores both a linear and a self-similar regime. This is confirmed by Fig.(5.8) in which the duration and the energy gain of the amplified seed are shown in function of the relative delay between pump and seed pulses: the best energy gain coincides with the shortest duration of the

amplified seed. To conclude this section, we showed that the relative delay between pump and seed is an important parameter both in simulations and experiments: different delays from the optimal one leads to lower seed amplification and compression. We point out that is difficult to make a direct comparison between the optimal relative delay between pump and seed t_{opt} found in simulations (chapter 4) with the best one found in experiments. This is because in experiments other parameters, such as the quality of seed beam and of the plasma density and the self-focusing of the pump beam [47], can affect the estimation of the optimal relative delay.

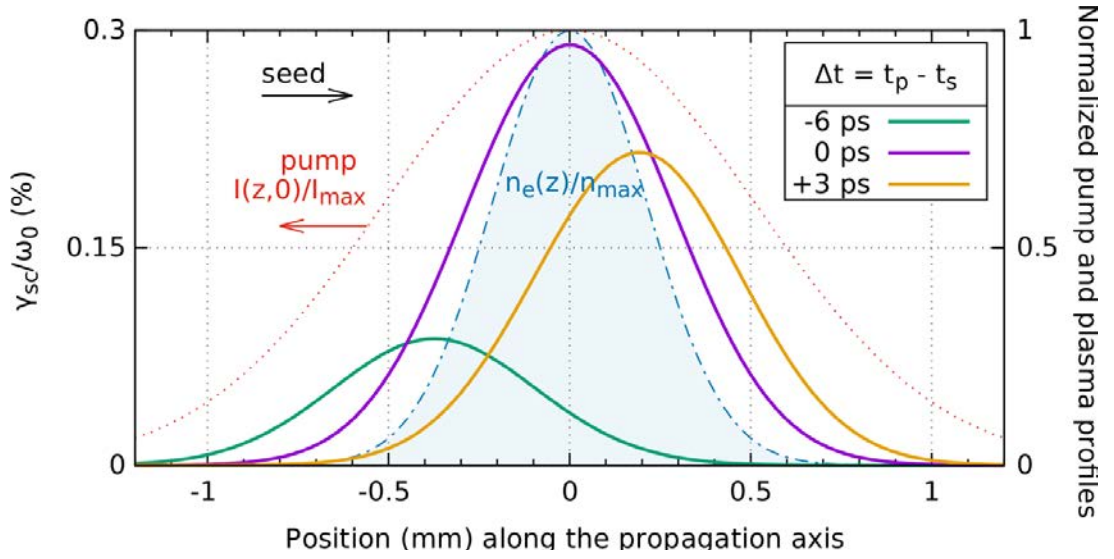


Figure 5.4: Evolution of the growth rate (solid curves, left scale) seen by the seed for different delays Δt with the counter propagating pump (dotted red curve, right scale).

5.1.2 Influence of amplification on SRS spectra

Another important point of interest is the competition between the Raman and Brillouin backscattering instabilities in the seed amplification. Stimulated Raman scattering could reduce the efficiency or quality of the Brillouin amplification process [38][35]. For very short pulses it could also contribute to the seed amplification [28]. In [34] a strong decrease of Raman backscattering has been observed when the SBS amplification of the seed takes place. This is showed in Fig.(5.7) in which the green squares represents the Raman contribution to the amplified seed in function of the relative delay between pump and seed pulses. At higher values of seed energy gain, the SRS signal has a lower amplitude and frequency bandwidth with respect to shots at lower gain.

In this section we present some simulations in which we keep the ions immobile, in

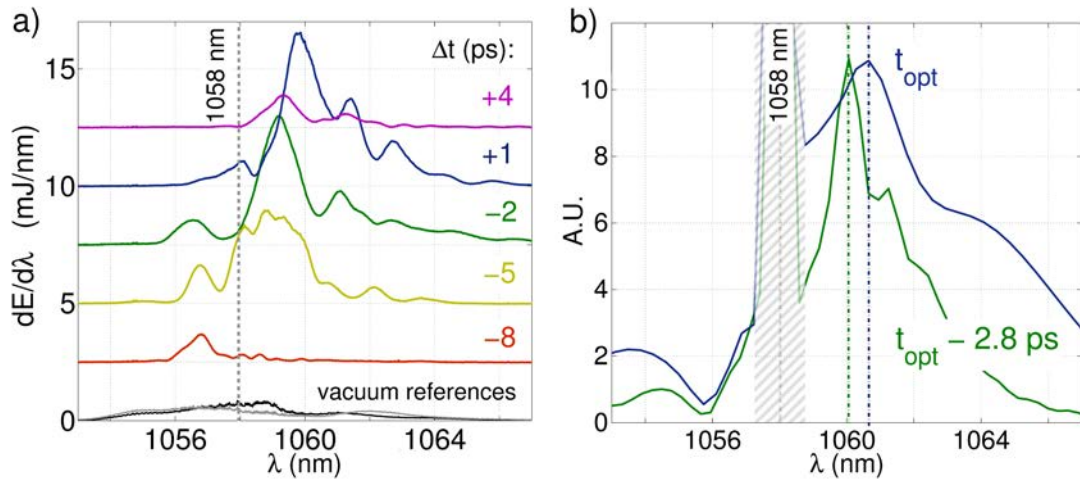


Figure 5.5: a) Transmitted spectra, expressed in mJ=nm, as a function of the delay. Two reference spectra in vacuum propagation are shown. b) 1D-PIC simulated spectra: optimal case (blue solid line) and delayed (green). The peak at the initial pump and seed wavelength (1058 nm) is masked to show only the spectra related to the amplification process.

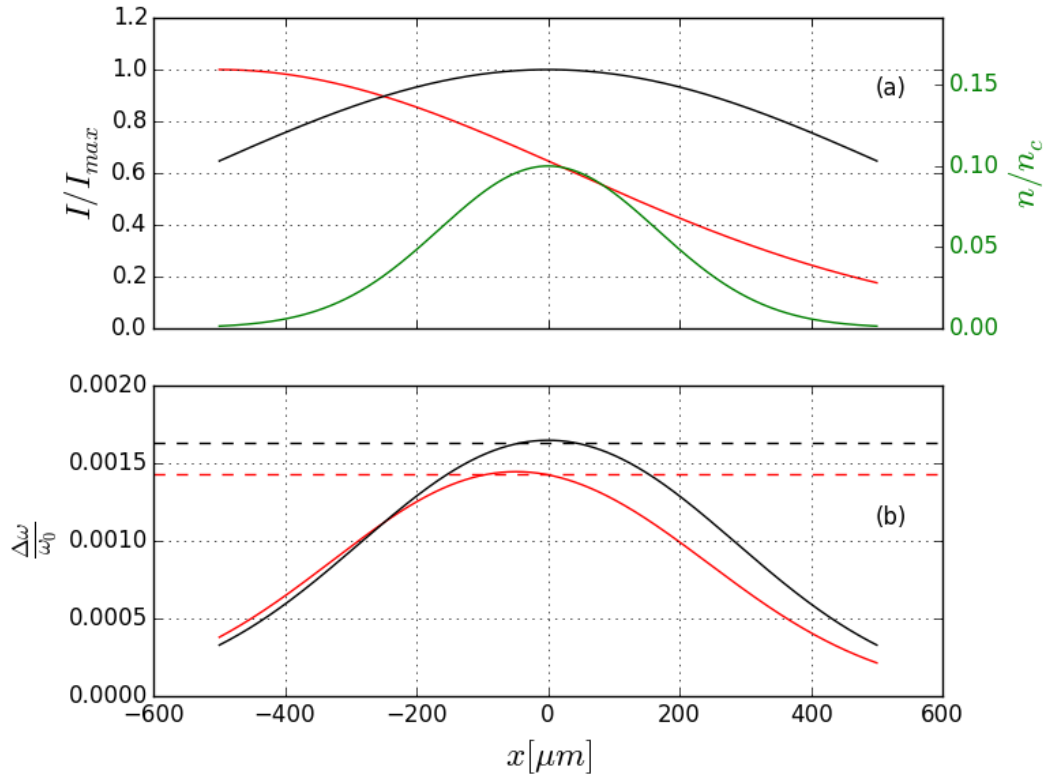


Figure 5.6: a) Local normalized values of the pump intensity at two different times: when the maximum of the pump reaches the left boundary of the box (red line) and when the pump is in the middle of the simulation box (black line). The green line indicates the plasma density profile. b) Values of the redshift $\Delta\omega/\omega_0$ as predicted by the sc-SBS linear theory (Chapter 1) versus the positions in the plasma and depending on the different position of the pump (red and black lines correspond to $\Delta\omega/\omega_0 \approx 0.0015$ and $\Delta\omega/\omega_0 \approx 0.0017$, respectively)

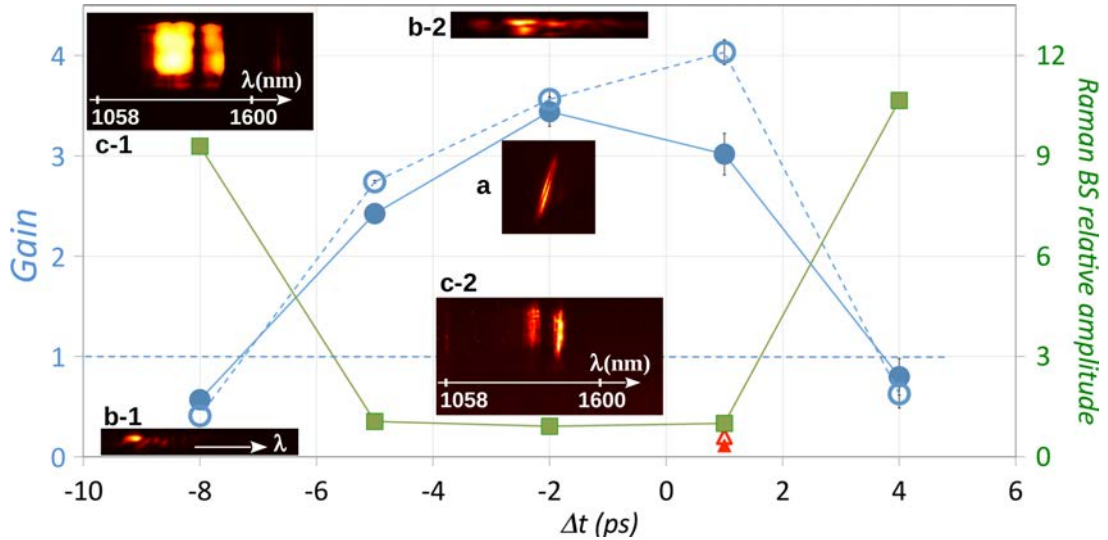


Figure 5.7: Energy gain E_{out}/E_{in} of the seed (left scale, blue circles) and pump Raman backscattered signal (right scale, green squares), as a function of relative delay between pump and seed arrival time at the plasma center. Full (empty) circles are the 2D (1D) calorimetry. Plasma density is $0.1n_c$.

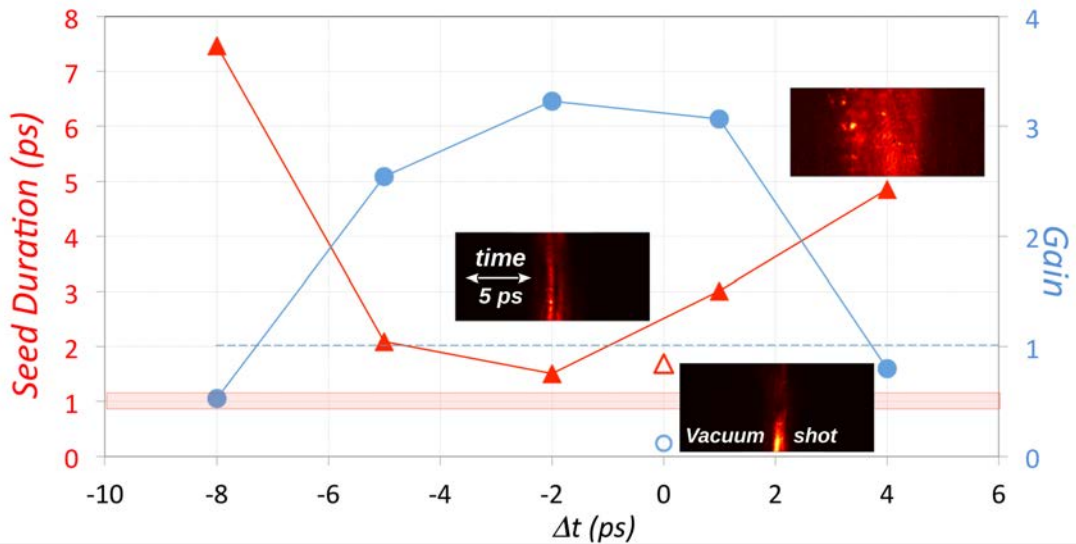


Figure 5.8: Duration (FWHM, left axis, triangles) and energy gain (right axis, circles) of the amplified seed laser as a function of relative delay between pump and seed arrival time at the plasma center.

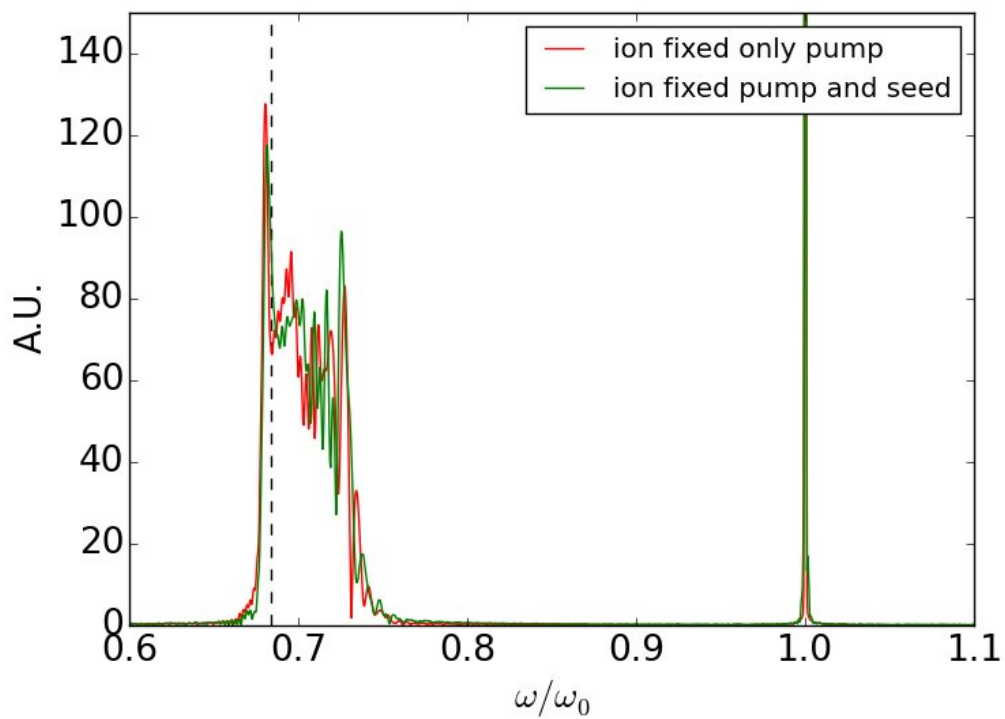


Figure 5.9: Comparison of the spectra for the simulations with ion fixed in the case with only the pump signal going through the plasma (red line) and the case with both pump and seed lasers interacting (green line).

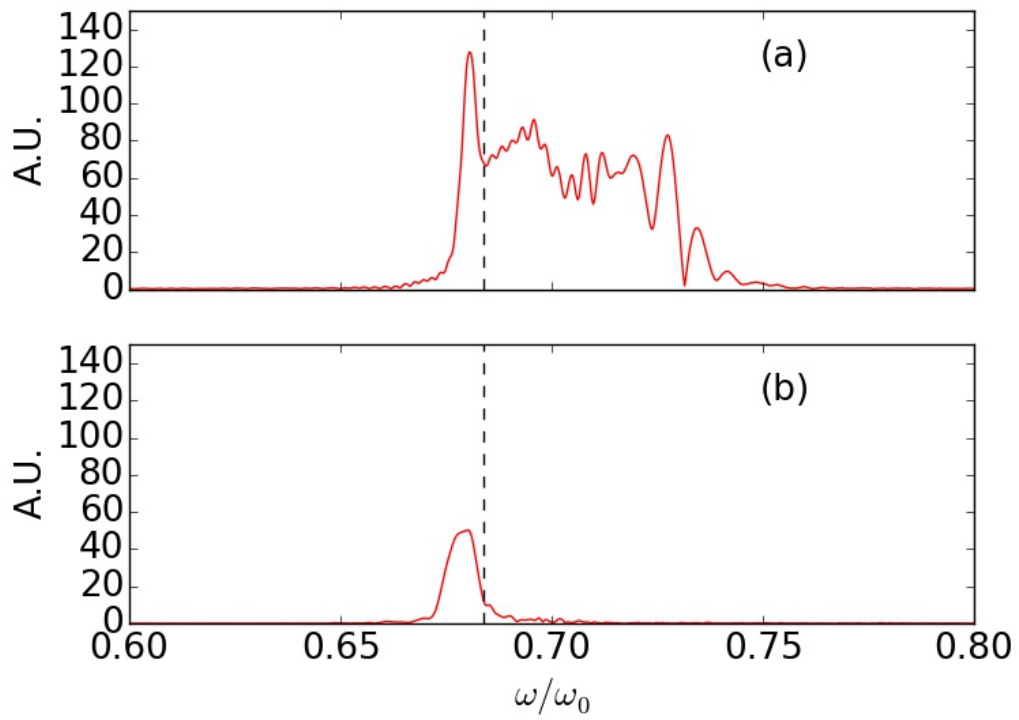


Figure 5.10: Spectra in ω/ω_0 of the electric field E_z . a) Simulation with only the pump laser and the ions immobile. b) Simulation with both pump and seed lasers and the ions mobile.

order to better understand the competition between the SRS and SBS amplification mechanisms [34], present for the cases considered in chapter 4 and in the experiments [34][36]. In particular two identical simulations have been performed, with the same parameters as reported at the beginning of this section, with the immobile ions (SBS suppressed). In the first one only the pump goes throughout the plasma and no seed is sent in the simulation box, in the second, both pump and seed lasers interact. With the immobile ions only the thermal SRS can develop. In Fig. 5.9, we show the frequency spectra integrated over the whole simulation and recorded at the left edge of the simulation box, outside the plasma. At this edge we have: i) the pump signal, incoming from left to right; ii) the seed (when it is present) outgoing from right to left; iii) and the backscattered pump signal. The frequency axis has been normalized to ω_0 , so that $\omega/\omega_0 = 1$ corresponds to nominal frequency of the pump and the seed at the entrance in the simulation box. The red line indicates the SRS frequency ($\omega_R/\omega_0 \approx 0.68$) for the backscattered electric field at the maximum value of the plasma density ($n_{max}/n_c = 0.1$). The important result is that, *when the SBS is suppressed (fixed ions) there is no difference in the spectra whether the seed is present or not and the band width is large showing the presence of SRS from different points along the plasma density profile*. This proves that the SRS signal is only related to the spontaneous backscattering of the pump. There is no coupling between pump and seed if sc-SBS amplification is quenched as the frequency matching condition for SRS is not satisfied. In Fig. 5.10 we compare the spectra of the electric field E_z (around the expected values of the backscattered Raman wave) from the simulation with ion fixed and only the pump (Fig. 5.10(a)) with the spectra from the simulation with both the laser interacting and the ion mobile (Fig. 5.10(b)). When the SBS coupling is suppressed (Fig. 5.10(a)) the signal at Raman frequencies is strong and spread. On the opposite side, *when the SBS can occur (Fig. 5.10(b), mobile ions), the Raman signal is smaller and only the frequency corresponding to the highest density value ($n/n_c = 0.1$) appears*. Notice that the large spread of the spectrum in Fig. 5.10(a) is due to the strong plasma density inhomogeneities (spanning between $\omega/\omega_0 \approx 0.68$ for $n/n_c = 0.1$ and $\omega/\omega_0 \approx 0.74$ for $n/n_c \approx 0.07$) created by the SRS backscattering of the pump. Even if the Raman spectrum is large, it is well separated from the SBS range of frequency. This is more true when SBS amplifications sets in (Fig. 5.10(b)). From those results we can state the presence of an anti-correlation between the SBS and the spontaneous mechanism: all the SRS signals are from backscattering of the pump signal and, *in presence of SBS amplification mechanism, the SRS contribution is limited* [34]. Fig.(5.11) shows the backscattered Raman scattering of the pump in the experiments: it also shows that *the triggering of SBS amplification (maximized in the optimal case, when*

$\Delta t = -2$ ps, *Fig.(5.11)(a)* reduces drastically the spontaneous backscattered Raman of the pump, as also observed in simulations. In correspondence of the delay for which the SBS amplification reaches the highest efficiency ($\Delta t = -2$ ps), the spread of the Raman spectrum is reduced compared to the one in correspondence of other values of relative delays.

5.2 Conclusions

In this chapter we show a comparison between results obtained from PIC simulations and from recent experiments carried out at LULI [34][36]. One dimensional PIC simulations help to describe and interpret the quality of the amplification process obtained in experiments. As a result of our study, we demonstrated and validated the first experimental observation of the signatures of the transition from linear to self-similar regime as we also reported in [34]. The comparison among the spectra from experiments, PIC simulations and the predictions given by the sc-SBS linear theory confirms that in the experiments the seed explores both a linear and self-similar regime of amplification. We also showed how the choice of the relative delay between the pump and seed beams is a crucial parameter not only theoretically [35] but equally in nowadays experiments. In [34] a strong decrease of the Stimulated Raman Amplification occurs has been measured for the first time. These findings are confirmed by PIC simulations that show that the triggering of SBS is responsible for the amplification, strongly limiting the growth of SRS. This is particularly true in simulations, where we show that when the Stimulated Brillouin Amplification is suppressed keeping the ions immobile, there is no difference in the spectra around the Raman frequency, proving that the SRS signal is only related to the spontaneous backscattering of the pump.

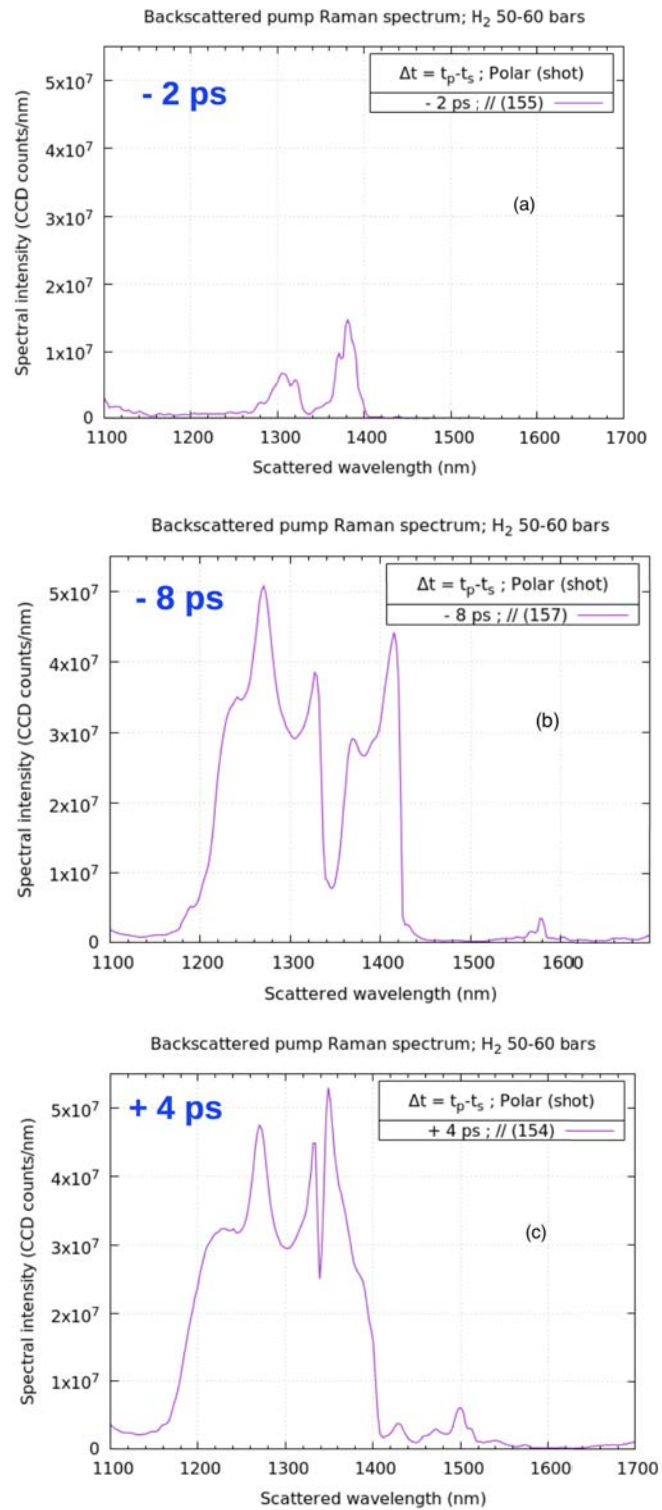


Figure 5.11: Backscattered pump Raman spectrum for a relative pump-seed delay of $\Delta t = -2 ps$ (a), $\Delta t = -8 ps$ (b), $\Delta t = +4 ps$ (c)

Chapter 6

Presentation of the new particle in code SMILEI and results of two dimensional simulations of sc-SBS amplification

In this chapter we present the new particle-in-cell code SMILEI developed during the last three years at LULI: I have participated to the development of SMILEI from the very beginning, focusing on the diagnostic module of the code. This code has been also used to carry out all the results showed in this thesis work. This chapter is organized as following: after a short introduction on the motivation on the development of the SMILEI code, we show the structure of the code and the efforts made on the side of the parallelization and the optimization of the code. In the last part of this chapter we show an application of SMILEI on very large scale two-dimensional simulations on SBS in the strong coupling regime.

The Particle-In-Cell (PIC) approach is a very popular method for solving a wide range of physics problems. Initially developed for fluid dynamics studies [50], its various advantages (conceptual simplicity, efficient implementation on massively parallel computers, etc.) have since established it as a central simulation tool for plasma physics, from semiconductors to cosmology or accelerators.

Today, the kinetic simulation of plasmas in various environments, from the laboratory to astrophysics, strongly relies on PIC codes [51]. In this chapter, we present the new open-source PIC code SMILEI. It has been developed in a collaborative framework including physicists and high-performance computing (HPC) experts to best benefit from the new HPC architectures and paradigms. SMILEI development was initially motivated by recent progresses in ultra-high intensity (UHI) laser technology, and ongoing

projects aiming at building multi-petawatt laser facilities. To support this formidable experimental and technological undertaking, new numerical tools have to be deployed.

In addition, SMILEI development started at a time when a paradigm shift occurred in HPC. In particular, the number of cores exploitable on modern massively parallel supercomputers has skyrocketed. This tendency is progressing quickly but software development lags behind. Today, most of the codes used by the plasma community face difficulties when confronted with these new challenges, and a strong collaboration between physicists and HPC specialists is necessary to overcome these difficulties. Intended as a multi-purpose and collaborative PIC code, SMILEI today addresses a wide range of physics problems, from laser-plasma interaction to astrophysics.

This chapter aims at presenting an overview of some of the code's principles and structure. In the Annexe B we show more in detail the SMILEI's performance and capabilities, as well as benchmarks and examples.

6.1 The Particle-In-Cell (PIC) method for collisionless plasmas

The Maxwell-Vlasov model

The kinetic description of a collisionless plasma¹ relies on the Vlasov-Maxwell system of equations. In this description, the different species of particles constituting the plasma are described by their respective distribution functions $f_s(t, \mathbf{x}, \mathbf{p})$, where s denotes a given species consisting of particles with charge q_s and mass m_s , and \mathbf{x} and \mathbf{p} denote the position and momentum of a phase-space element. The distribution f_s satisfies Vlasov's equation:

$$\left(\partial_t + \frac{\mathbf{p}}{m_s \gamma} \cdot \nabla + \mathbf{F}_L \cdot \nabla_{\mathbf{p}} \right) f_s = 0, \quad (6.1)$$

where $\gamma = \sqrt{1 + \mathbf{p}^2 / (m_s c)^2}$ is the (relativistic) Lorentz factor, c is the speed of light in vacuum, and

$$\mathbf{F}_L = q_s (\mathbf{E} + \mathbf{v} \times \mathbf{B}) \quad (6.2)$$

is the Lorentz force acting on a particle with velocity $\mathbf{v} = \mathbf{p} / (m_s \gamma)$. This force follows from the existence, in the plasma, of collective electric $[\mathbf{E}(t, \mathbf{x})]$ and magnetic $[\mathbf{B}(t, \mathbf{x})]$

¹The PIC method can be applied to (fully or partially ionized) plasmas as well as beams of charged particles. For the sake of simplicity however, we will refer to all these states as plasmas.

fields satisfying Maxwell's equations:

$$\nabla \cdot \mathbf{B} = 0, \quad (6.3a)$$

$$\nabla \cdot \mathbf{E} = \rho/\epsilon_0, \quad (6.3b)$$

$$\nabla \times \mathbf{B} = \mu_0 \mathbf{J} + \mu_0 \epsilon_0 \partial_t \mathbf{E}, \quad (6.3c)$$

$$\nabla \times \mathbf{E} = -\partial_t \mathbf{B}, \quad (6.3d)$$

where ϵ_0 and μ_0 are the vacuum permittivity and permeability, respectively.

The Vlasov-Maxwell system of equations (6.1–6.3) describes the self-consistent dynamics of the plasma which constituents are subject to the Lorentz force, and in turn modify the collective electric and magnetic fields through their charge and current densities:

$$\rho(t, \mathbf{x}) = \sum_s q_s \int d^3p f_s(t, \mathbf{x}, \mathbf{p}), \quad (6.4a)$$

$$\mathbf{J}(t, \mathbf{x}) = \sum_s q_s \int d^3p \mathbf{v} f_s(t, \mathbf{x}, \mathbf{p}). \quad (6.4b)$$

Quasi-particles and the PIC method

The ‘‘Particle-In-Cell’’ method owes its name to the discretization of the distribution function f_s as a sum of N_s ‘‘quasi-particles’’ (also referred to as ‘‘super-particles’’ or ‘‘macro-particles’’):

$$f_s(t, \mathbf{x}, \mathbf{p}) = \sum_{p=1}^{N_s} w_p S(\mathbf{x} - \mathbf{x}_p(t)) \delta(\mathbf{p} - \mathbf{p}_p(t)), \quad (6.5)$$

where w_p is a quasi-particle ‘‘weight’’, \mathbf{x}_p is its position, \mathbf{p}_p is its momentum, S is the shape-function of all quasi-particles and δ is the Dirac distribution.

In PIC codes, Vlasov's equation (6.1) is integrated along the continuous trajectories of these quasi-particles, while Maxwell's equations (6.3) are solved on a discrete spatial grid, the spaces between consecutive grid points being referred to as ‘‘cells’’. Injecting the discrete distribution function of Eq. (6.5) in Vlasov's equation (6.1), multiplying the result by \mathbf{p} and integrating over all \mathbf{p} and over the volume of the quasi-particles, leads to the relativistic equations of motion of individual quasi-particles:

$$\frac{d\mathbf{x}_p}{dt} = \frac{\mathbf{u}_p}{\gamma_p} \quad (6.6)$$

$$\frac{d\mathbf{u}_p}{dt} = r_s \left(\mathbf{E}_p + \frac{\mathbf{u}_p}{\gamma_p} \times \mathbf{B}_p \right), \quad (6.7)$$

where $r_s = q_s/m_s$ is the charge-over-mass ratio (for species s), $\mathbf{u}_p = \mathbf{p}_p/m_s$ is the reduced momentum and $\gamma_p = \sqrt{1 + \mathbf{u}_p^2}$ is the Lorentz factor.

In this Section, we present the general PIC algorithm, starting with the simulation initialization and then going through the PIC loop itself (see Tab.6.1).

Table 6.1: Summary of SMILEI’s PIC algorithm.

Initialization	time step $n = 0$, time $t = 0$
Particle loading	$\forall p$, define $(\mathbf{x}_p)^{n=0}$, $(\mathbf{u}_p)^{n=-\frac{1}{2}}$
Charge projection on grid	$[\forall p, (\mathbf{x}_p)^{n=0}] \rightarrow \rho_{i,j,k}^{(n=0)}$
Compute initial fields	- solve Poisson on grid: $[\rho_{i,j,k}^{(n=0)}] \rightarrow \mathbf{E}_{\text{stat}}^{(n=0)}$ - add external fields: $\mathbf{E}_{i,j,k}^{(n=0)}$, $\mathbf{B}_{i,j,k}^{(n=0)} = \mathbf{B}_{i,j,k}^{(n=\frac{1}{2})}$
PIC loop: from time step n to $n + 1$, time $t = (n + 1) \Delta t$	
Restart charge & current densities	
Save magnetic fields value (used to center magnetic fields)	
Interpolate fields at particle positions	$\forall p$, $[(\mathbf{E})_{i,j,k}^{(n)}, (\mathbf{B})_{i,j,k}^{(n)}] \rightarrow \mathbf{E}_p^{(n)}, \mathbf{B}_p^{(n)}$
Push particles	- compute new velocity $\forall p$, $\mathbf{p}_p^{(n-\frac{1}{2})} \left[\mathbf{E}_p^{(n)}, \mathbf{B}_p^{(n)} \right] \mathbf{p}_p^{(n+\frac{1}{2})}$ - compute new position $\forall p$, $\mathbf{x}_p^{(n)} \left[\mathbf{p}_p^{(n+\frac{1}{2})} \right] \mathbf{x}_p^{(n+1)}$
Project current onto the grid	using a charge-conserving scheme $\left[\forall p \mathbf{x}_p^{(n)}, \mathbf{x}_p^{(n+1)}, \mathbf{p}_p^{(n+\frac{1}{2})} \right] \rightarrow \mathbf{J}_{i,j,k}^{(n+\frac{1}{2})}$
Solve Maxwell’s equations	
	- solve Maxwell-Faraday: $\mathbf{E}_{i,j,k}^{(n)} \left[\mathbf{J}_{i,j,k}^{(n+\frac{1}{2})} \right] \mathbf{E}_{i,j,k}^{(n+1)}$
	- solve Maxwell-Ampere: $\mathbf{B}_{i,j,k}^{(n+\frac{1}{2})} \left[\mathbf{E}_{i,j,k}^{(n+1)} \right] \mathbf{B}_{i,j,k}^{(n+\frac{3}{2})}$
	- center magnetic fields: $\mathbf{B}_{i,j,k}^{(n+1)} = \frac{1}{2} \left(\mathbf{B}_{i,j,k}^{(n+\frac{1}{2})} + \mathbf{B}_{i,j,k}^{(n+\frac{3}{2})} \right)$

Time- and space-centered discretization

As will be discussed in Sec.6.1.1, Maxwell's equations are solved here using the Finite Difference Time Domain (FDTD) approach[52] as well as refined methods based on this algorithm (for a review of these methods see [53]). In these methods, the electromagnetic fields are discretized onto a staggered grid, the Yee-grid, that allows for spatial-centering of the discretized curl operators in Maxwell's equations (6.3c) and (6.3d). Similarly, the time-centering of the time-derivative in Maxwell's equations(6.3c) and (6.3d) is ensured by considering the electric fields as defined at integer time-steps (n) and magnetic fields at half-integer time-steps ($n + \frac{1}{2}$). Time-centering of the magnetic fields is however necessary for diagnostic purposes, and most importantly when computing the Lorentz force acting on the quasi-particles. It should also be noted, as will be discussed in Sec. 6.1.1, that a *leap-frog* scheme is used to advance the particles in time, so that their positions and velocities are defined at integer (n) and half-integer ($n - \frac{1}{2}$) time-steps, respectively.

6.1.1 The PIC loop

At the end of the initialization stage [time-step ($n = 0$)], all quasi-particles in the simulation have been loaded and the electromagnetic fields have been computed over the whole simulation grid. The PIC loop is then started over N time-steps each consisting in (i) interpolating the electromagnetic fields at the particle positions, (ii) computing the new particle velocities and positions, (iii) projecting the new charge and current densities on the grid, and (iv) computing the new electromagnetic fields on the grid. In this section, we describe these four steps taken to advance from time-step (n) to time-step ($n + 1$).

Field interpolation at the particle

At the beginning of time-step (n), the particles velocities and positions are known at time-step $n - \frac{1}{2}$ and n , respectively. For each particle p , the electromagnetic fields [at time-step (n)] are computed at the particle position using a simple interpolation technique:

$$\mathbf{E}_p^{(n)} = V_c^{-1} \int d\mathbf{x} S(\mathbf{x} - \mathbf{x}_p^{(n)}) \mathbf{E}^{(n)}(\mathbf{x}), \quad (6.8)$$

$$\mathbf{B}_p^{(n)} = V_c^{-1} \int d\mathbf{x} S(\mathbf{x} - \mathbf{x}_p^{(n)}) \mathbf{B}^{(n)}(\mathbf{x}), \quad (6.9)$$

where we have used the time-centered magnetic fields $\mathbf{B}^{(n)} = \frac{1}{2}[\mathbf{B}^{(n+1/2)} + \mathbf{B}^{(n-1/2)}]$, and V_c denotes the volume of a cell.

Particle pusher

Knowing, for each quasi-particle, the electromagnetic fields at its position, the new particle momentum and position are computed using a (second order) leap-frog integrator. The new particle momentum is computed according to:

$$\mathbf{u}_p^{n+\frac{1}{2}} = \mathbf{u}_p^{n-\frac{1}{2}} + r_s \Delta t \left[E_p^{(n)} + \frac{\mathbf{v}_p^{(n+\frac{1}{2})} + \mathbf{v}_p^{(n-\frac{1}{2})}}{2} \times B_p^{(n)} \right], \quad (6.10)$$

as well as the new particle position:

$$\mathbf{x}_p^{n+1} = \mathbf{x}_p^n + \Delta t \frac{\mathbf{u}_p^{n+\frac{1}{2}}}{\gamma_p}, \quad (6.11)$$

where Δt denotes the duration of a time-step.

Charge conserving current deposition

Charge deposition (i.e. charge and current density projection onto the grid) is then performed using the charge-conserving algorithm proposed by Esirkepov [56]. The current densities in the dimensions of the grid (i.e., the x -direction for 1D3V simulations, both x - and y -directions for 2D3V simulations, and all three x -, y - and z -directions for 3D3V simulations) are computed from the charge flux through the cell borders (hence ensuring charge conservation) while the current densities along the other dimensions are performed using a simple projection. To illustrate this point, we take the example of current deposition in a 2D3V simulation. The current densities in the x - and y -directions associated to a particle with charge q are computed as:

$$(J_x)_{i+\frac{1}{2},j}^{(n+\frac{1}{2})} = (J_x)_{i-\frac{1}{2},j}^{(n+\frac{1}{2})} + q w_p \frac{\Delta x}{\Delta t} (W_x)_{i+\frac{1}{2},j}^{(n+\frac{1}{2})} \quad (6.12)$$

$$(J_y)_{i,j+\frac{1}{2}}^{(n+\frac{1}{2})} = (J_y)_{i,j-\frac{1}{2}}^{(n+\frac{1}{2})} + q w_p \frac{\Delta y}{\Delta t} (W_y)_{j,i+\frac{1}{2}}^{(n+\frac{1}{2})} \quad (6.13)$$

where $(W_x)^{(n+\frac{1}{2})}$ and $(W_y)^{(n+\frac{1}{2})}$ are computed from the particle present and former positions $x_p^{(n+1)}$ and $x_p^{(n)}$, respectively, using the method developed by Esirkepov. The

particle current in the z -direction (not a dimension of the grid) is, in this geometry, computed using a simple projection:

$$(\mathbf{J}_z)_{i,j} = qw_r \mathbf{v}_p S(\mathbf{x}_{i,j} - \mathbf{x}_p). \quad (6.14)$$

Similarly, the charge density deposited by the particle is obtained using the simple projection:

$$(\rho)_{i,j}^{(n+1)} = q w_p S(\mathbf{x}_{i,j} - \mathbf{x}_p^{(n+1)}). \quad (6.15)$$

The total charge and current densities henceforth gather the contributions of all quasi-particles of all species. It is worth noting that, within a charge-conserving framework, charge densities are only projected on the grid for diagnostics purposes (as we will see in next paragraph, it is not used to advance the electromagnetic fields).

Maxwell solvers

Now that the currents are known at time-step $n + \frac{1}{2}$, the electromagnetic fields can be advanced solving Maxwell's equations (6.3). First, Maxwell-Ampère Eq. (6.3c) is solved, giving the advanced electric fields:

$$\mathbf{E}^{(n+1)} = \mathbf{E}^{(n)} + \Delta t \left[(\nabla \times \mathbf{B})^{(n+\frac{1}{2})} - \mathbf{J}^{(n+\frac{1}{2})} \right]. \quad (6.16)$$

Then, Maxwell-Faraday Eq. (6.3d) is computed, leading to the advanced magnetic fields:

$$\mathbf{B}^{(n+\frac{3}{2})} = \mathbf{B}^{(n+\frac{1}{2})} - \Delta t (\nabla \times \mathbf{E})^{(n+1)}. \quad (6.17)$$

Before discussing the discretization of the curl-operator in more details, it is worth noting that solving Eqs. (6.3c) and (6.3d) is sufficient to get a complete description of the new electromagnetic fields. Indeed, it can be shown that this conserves a divergence-free magnetic field if Gauss' equation (6.3a) is satisfied at time $t = 0$. Similarly, Poisson's equation (6.3b) is verified as long as it is satisfied at time $t = 0$, if the charge deposition algorithm fulfills the charge conservation equation:

$$\partial_t \rho + \nabla \cdot \mathbf{J} = 0 \quad (6.18)$$

This motivated the use of Esirkepov's projection scheme discussed in the previous paragraph. We conclude this Section by discussing in more details the discretization of the curl-operators in Eqs. (6.3c) and (6.3d). To do so, let us focus on the equations

for the electric and magnetic fields E_x and B_x discretized on the (staggered) Yee-grid:

$$\frac{(E_x)^{(n+1)}_{i+\frac{1}{2},j,k} - (E_x)^{(n)}_{i+\frac{1}{2},j,k}}{\Delta t} = (J_x)^{n+\frac{1}{2}}_{i+\frac{1}{2},j,k} + (\partial_y B_z)^{(n+\frac{1}{2})}_{i+\frac{1}{2},j,k} - (\partial_z B_y)^{(n+\frac{1}{2})}_{i+\frac{1}{2},j,k}, \quad (6.19)$$

$$\frac{(B_x)^{(n+\frac{3}{2})}_{i,j+\frac{1}{2},k+\frac{1}{2}} - (B_x)^{(n+\frac{1}{2})}_{i,j+\frac{1}{2},k+\frac{1}{2}}}{\Delta t} = (\partial_z^* E_y)^{(n+1)}_{i,j+\frac{1}{2},k+\frac{1}{2}} - (\partial_y^* B_z)^{(n+\frac{1}{2})}_{i,j+\frac{1}{2},k+\frac{1}{2}}. \quad (6.20)$$

The partial derivatives in space in both equations are discretized as follows. In the Maxwell-Ampere equation, the partial derivative in x (similarly in y and z) reads:

$$(\partial_x F)_{i,j,k} = \frac{F_{i+\frac{1}{2},j,k} - F_{i-\frac{1}{2},j,k}}{\Delta x}, \quad (6.21)$$

and corresponds to the usual curl-operator discretization used in the FDTD method. In the Maxwell-Faraday equation, the partial derivatives are modified as proposed by various authors . The spatial derivative in the x -direction (similarly in the y and z directions) reads:

$$\begin{aligned} (\partial_x^* F)_{i,j,k} = & \alpha_x \frac{F_{i+\frac{1}{2},j,k} - F_{i-\frac{1}{2},j,k}}{\Delta x} + \eta_x \frac{F_{i+\frac{3}{2},j,k} - F_{i-\frac{3}{2},j,k}}{\Delta x} \\ & + \beta_{xy} \left[\frac{F_{i+\frac{1}{2},j+1,k} - F_{i-\frac{1}{2},j+1,k}}{\Delta x} + \frac{F_{i+\frac{1}{2},j-1,k} - F_{i-\frac{1}{2},j-1,k}}{\Delta x} \right] \\ & + \beta_{xz} \left[\frac{F_{i+\frac{1}{2},j,k+1} - F_{i-\frac{1}{2},j,k+1}}{\Delta x} + \frac{F_{i+\frac{1}{2},j,k-1} - F_{i-\frac{1}{2},j,k-1}}{\Delta x} \right] \end{aligned} \quad (6.22)$$

and the parameters α_x , η_x , β_{xy} and β_{xz} satisfy:

$$\alpha_x + 2\beta_{xy} + 2\beta_{xz} + 3\eta_x = 1, \quad (6.23)$$

to ensure second order accuracy [57].

More details on the SMILEI's performances are discussed in the appendix B where we focus on the efforts made on the parallelization. In particular, the optimization on the code allows one to run massively parallel large two dimensional simulations. The next section focuses on the results of two dimensional simulation on the sc-SBS amplification.

6.2 Two dimensional simulation of sc-SBS amplification of a short laser pulse

In this section we show two examples of very large two-dimensional simulations on the amplification of short laser pulses via the SBS instability in the strong coupling regime. The interest of these simulation is not only to test SMILEI on a large scale simulation, but also to propose new experimental configurations to optimize the process. Simulate the sc-SBS amplification of short laser pulses in conditions near to the experimental ones demands a big efforts in terms of calculation time and IT resources. As we showed in previous chapters, the experimental interaction length are typically of the order of millimeters and the lasers spot size is spanning between few tens to hundreds of micrometers: the physics of the system is evolving on the time scale of tens of picoseconds. In order to take in account all the phenomena implied [33] (such as the competition between Raman, Brillouin and the filamentation of the pump), a two dimensional description of the system is needed.

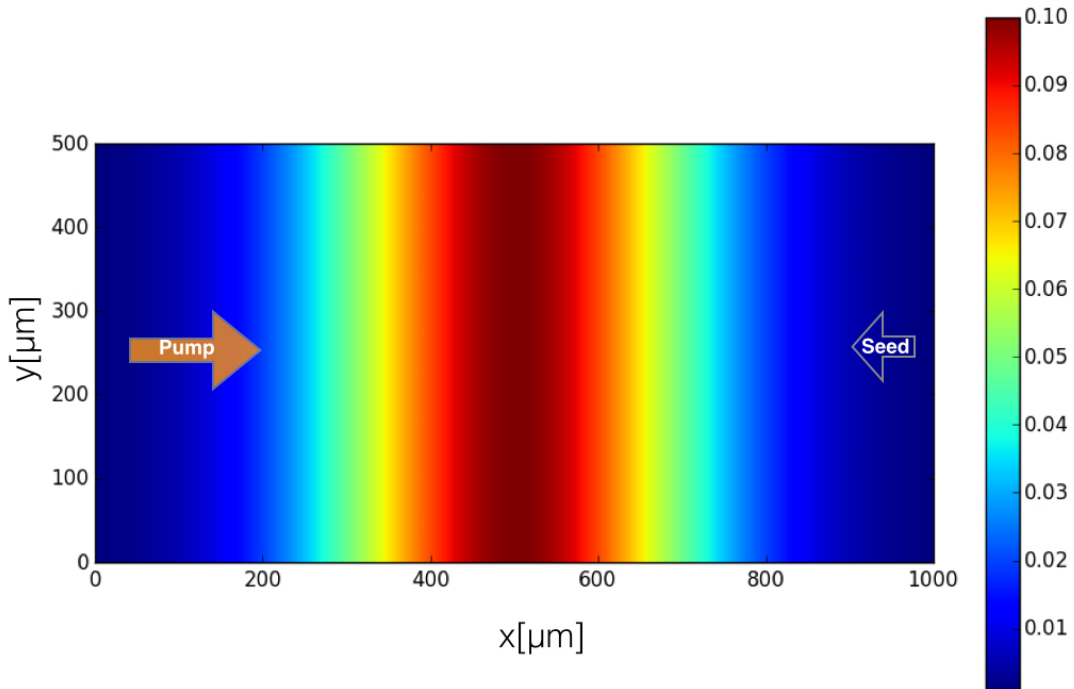


Figure 6.1: Plasma and lasers configuration for the simulation **SIM_A**: the pump and seed lasers are crossing in a gaussian plasma with an head-on geometry

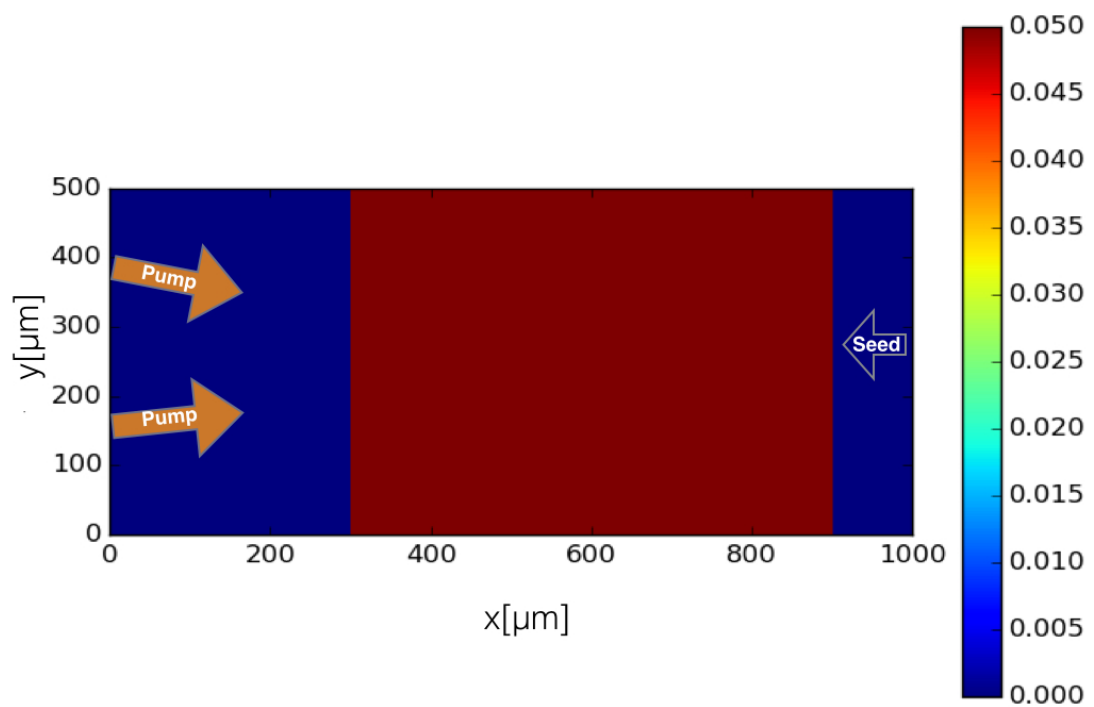


Figure 6.2: Plasma and lasers configuration for the simulation **SIM_B**: the seed lasers is interacting with two pump signals in a constant plasma shifted towards right. The two pump lasers are propagating in the plasma with an angle θ with respect to the seed direction of propagation

6.2.1 Simulations set-up

In this section we show two example of two dimensional simulations. In the first one (called **SIM_A** in the following) the lasers configuration is similar to what showed in the previous chapters: the pump ($\cos^2(t)$ temporal shape with duration of $FWHM_p = 4.2ps$, $I_p = 10^{15}W/cm^2$) and seed ($\cos^2(t)$ temporal shape with duration of $FWHM_s = 0.5ps$, $I_s = 10^{15}W/cm^2$) are crossing in a counter propagative geometry in a gaussian plasma. The plasma is 1 mm x 0.5 mm long and has a maximum value of density of $n/n_c = 0.1$. Both the seed and pump lasers have a transverse $\cos^2(y)$ shape with $FWHM_{y,A}^{tr} = 130 \mu m$. The aim of this simulation is to show that sc-SBS amplification can be an interesting tool to amplify short lasers pulses with an initial very large spot size. *If the phase front of the amplified seed is well conserved, the amplified pulse can be later focused to reach even higher intensities.*

In a second simulation (**SIM_B** in the following) we propose an innovative plasma-lasers configuration to further optimize th sc-SBS seed amplification. The seed ($\cos^2(t)$ temporal shape with duration of $FWHM_s = 0.5ps$, $I_s = 10^{15}W/cm^2$) is interacting with two pump ($\cos^2(t)$ temporal shape with duration of $FWHM_p = 4.2ps$, $I_p = 10^{15}W/cm^2$) that are counter-propagating with an angle of 6° degrees with respect to the seed direction of propagation. For this simulation the plasma is constant with $n/n_c = 0.05$ and it is shifted towards right. In this case the transverse size of the beams is smaller, $FWHM_{y,B}^{tr} = 30 \mu m$. Fig.(6.1) and Fig.(6.2) show the plasma geometry and the pump and seed lasers direction of propagation for the simulations considered. The advantage of the plasma-lasers set-in studied in this simulations is to separate the direction of backscattering of the pump lasers from the direction of propagation of the seed, as we will briefly show in the following. The space resolution for both the simulations is $\Delta x = 33 \text{ nm}$ (30720 x 15360 PIC cells). The total time simulated is $t_{sim} = 10 \text{ ps}$ with a time resolution of $\Delta t = 7.3 \times 10^{-2} \text{ fs}$. For each PIC cell there are 25 particles per specie, for a total number of particles of $pp_{SIM_A} = 23 \times 10^9$ for the simulation **SIM_A** and $pp_{SIM_B} = 16 \times 10^9$ for **SIM_B**. The simulations run on 65536 MPI processors (4096 nodes) involving 262144 threads OpenMP.

6.2.2 Amplification results

In Fig.(6.3) we show the pump and seed intensities at three different stages of the amplification. At $t = 5.8ps$ the seed starts to interact with the pump (Fig.(6.3)(a)). At $t = 7.6ps$ the seed reaches the middle of the simulation box: at that time the seed is still in the exponential regime of amplification, as the pump is not depleted yet. At $t = 9.7ps$ the seed has travelled through the entire simulation box and the pump is depleted: the final intensity of the seed os $I_{seed}^{out} \approx 4.6 \times 10^{15}$ that means $5 \times$ the

initial intensity. The final duration of the amplified seed is $t_{out} = 450$ fs: this confirms that the seed has been partially temporally compressed and that it experienced the self-similar regime of amplification. Notice that this simulation is optimized in terms of relative delay between the two pulse: the seed and pump maxima are crossing at $x \approx 320$ μm (corresponding to a delay of $t_{delay} = 2.5$ ps), that means on the left of the plasma maximum. This value of relative delay is the results of the optimization process made analyzing one dimensional simulations, as showed in chapter 4. The transverse size of the amplified seed at FWHM is of the order of $FWHM_{y,A}^{tr,out} \approx 100$ μm . This simulation demonstrates that sc-SBS is possible in the presence of a pump and an initial seed with very large transverse sections.

Fig.(6.4) shows the amplified seed exiting the simulation box at $t = 10$ ps for the case **SIM_B**: the final seed intensity is $I_{seed}^{out} \approx 3 \times 10^{15}$ ($3 \times$ the initial intensity). Even if the final intensity of the seed is lower than what obtained with the head-on configuration of **SIM_A**, this set-up allows the Raman signal originated by the backscattering of the pump to propagate mostly on the pump direction of propagation and be separated from the seed. The SBS amplification of the seed is confirmed by the spectra showed in Fig.(6.5): Fig.(6.5)(a) is the spectrum (in terms of wave number k/k_0 and frequency ω/ω_0 , where k_0 and ω_0 are the nominal wavenumber and frequency of the pump lasers) of the electric field recorded on the entire length of the left side of the simulation box. Fig.(6.5)(b) shows a zoom of the spectrum for $\omega/\omega_0 = [0.98,1.02]$: the peak in the amplified seed (central spot in the figure) confirms the signature of the sc-SBS amplification of the laser. The other color spots are the signatures of the propagating pump lasers at ω_0 frequency. Looking at the spectrum of Fig.(6.5)(a) , for $\omega/\omega_0 = [0.77,0.88]$, we see the Raman signal originated by the backscattering of the pump: part of this signal is concentrated around $k/k_0 = 0.1$ confirming the preferential direction of the backscattering of the pump. Notice that, at the end of the amplification, the transverse focal spot size of the seed at FWHM in intensity is $FWHM_{y,B}^{tr,out} \approx 28$ μm , that means of the same order of the initial one ($FWHM_{y,B}^{tr} = 30$ μm). Further optimization studies will improve this set-up.

6.3 Conclusions

In this chapter we briefly showed an overview of some of the SMILEI code's principles and structure. The effort made to create a new particle in cell code that responds the nowadays HPC opportunities made possible to carry out two dimensional sc-SBS amplification simulations on a very large scale, comparable to the real experiments one. We showed preliminary results from two examples of these two dimensional simulations: in a first one, we proved that the sc-SBS amplification is possible when the pump and

seed lasers have a large initial spot size. *In this case the seed amplified phase front is well conserved and the seed could be later focused to reach even higher intensities.* Notice that the results presented for this case are obtained making cross the maxima of the pulses on the decreasing portion of the plasma density (as seed by the seed during the propagation), confirming the importance of the relative delay between the pump and seed lasers. In a second simulation we proposed a set-up in which the seed is amplified by two pump propagating with an angle of 6° with respect to the seed direction. We showed that one of the advantages of this plasma-lasers configuration is to separate the Raman backscattering of the pump along the seed propagation. Experimentally, this plasma-lasers set-up will probably reduce the problem of pump and seed alignment typical of an head-on configuration. Further studies will allow a comparison with a simulation with the same set-up but with only pump present, similar to the experimental set-up shown in [36]. Moreover both the configurations shown here will create different plasma density gratings and it will be interesting to make a comparison with recent publications on the subject [45].

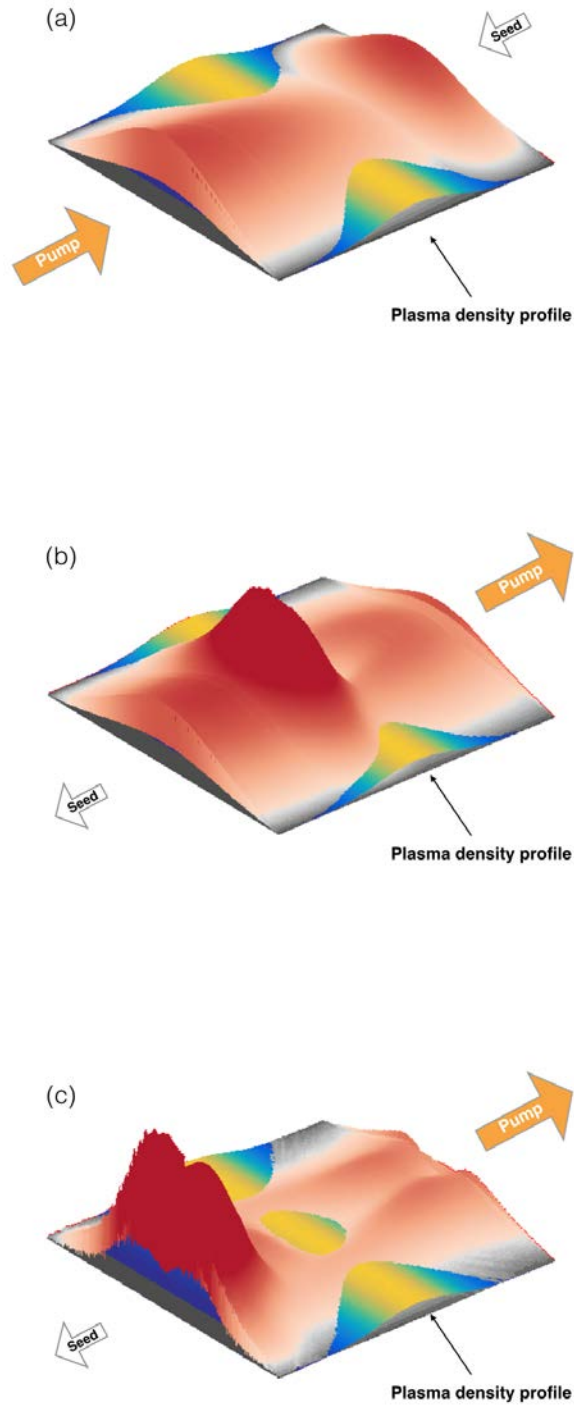


Figure 6.3: **SIM_A**: Evolution of the pump and seed intensities at $t = 5.8 ps$ (a), $t = 7.6 ps$ (b) and $t = 9.6 ps$ (c)

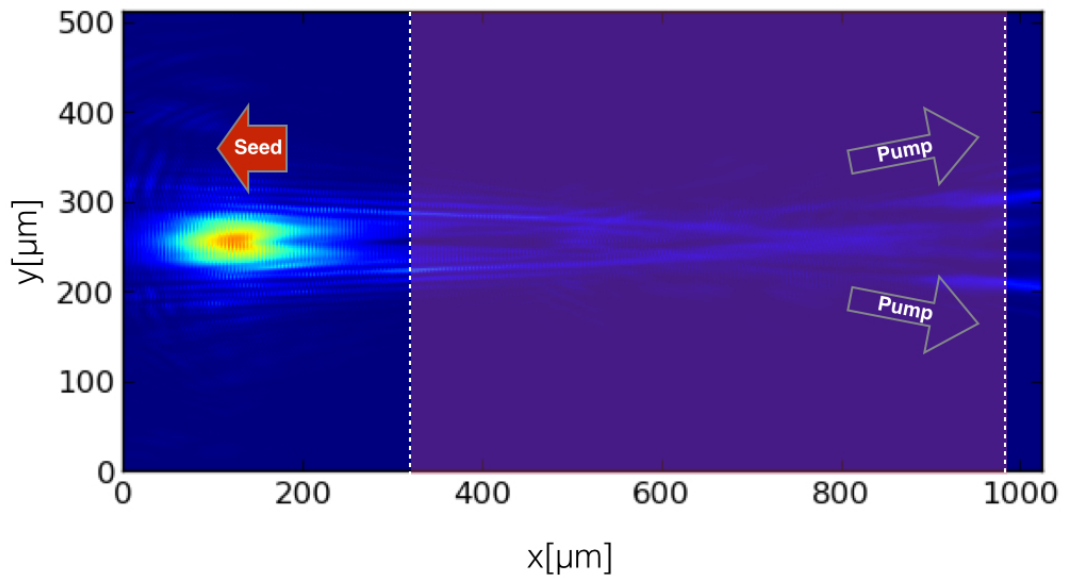


Figure 6.4: Pump and seed intensity at the end of the amplification, at $t = 10$ ps. The final intensity of the seed is $I_{seed}^{out} \approx 3 \times 10^{15}$ ($3 \times$ the initial intensity)

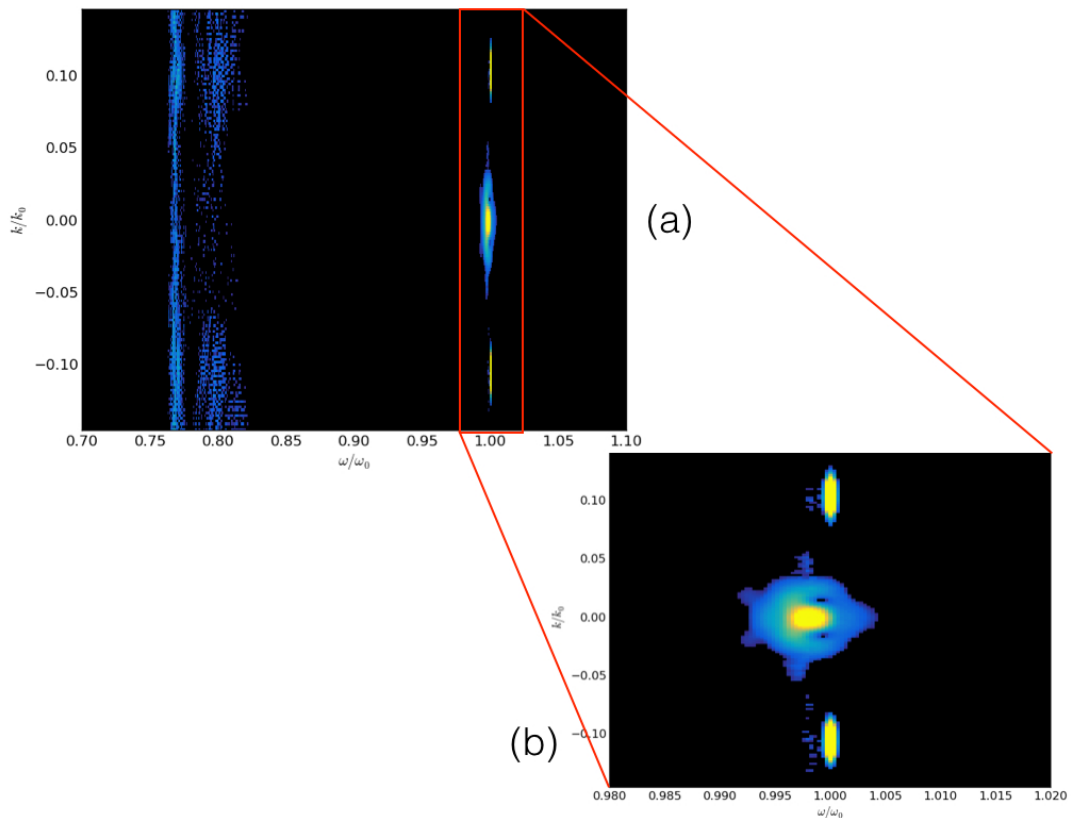


Figure 6.5: a) Spectrum (in terms of wave number k/k_0 and frequency ω/ω_0 , where k_0 and ω_0 are the nominal wavenumber and frequency of the pump lasers) of the electric field recorded on the entire length of the left side of the simulation box. b) Zoom of the spectrum for $\omega/\omega_0 = [0.98, 1.02]$

Conclusions

The problem of the plasma amplification of low energy, short (≈ 100 -500 fs) laser pulse by an energetic long (≈ 10 ps) pulse via strong coupling Stimulated Brillouin Backscattering has been investigated in this work, both analytically and numerically. We found that studying explicitly the amplitudes and the phases in the system of equations describing the SBS amplification, we can make a complete description of the different stages of amplification. In the strong-coupling regime, contrary to the weak coupling regime, the phases of the participating waves are continuously evolving with time. We showed that the initial energy transfer direction is dictated by the evolution of the phases: as long as the electric field amplitude of the pump is more important than the seed one, the pump gives energy to the seed. Concerning the evolution of the different stages of the amplification, we found that at the beginning of the of the coupling, the total phase ϑ (defined as a combination of the phase of the pump, of the seed and of the density perturbations) is determined by the seed phase. When later in time the seed enters the exponential regime of amplification, known as "linear regime", the seed and density perturbation phases start to compensate each other (letting the pump phase unchanged and equal to zero), resulting in a constant value of the total phase. The system will stay in this regime as long as the pump depletion is negligible. When the amplitude of the amplified seed and of the pump are comparable, the total phase starts evolving again driven by the variation of the pump phase: at that moment the electric field of the amplified seed reaches its maximum and the pump no longer provides energy to the seed. The energy flow is then reversed (the seed starts to give energy to the pump) and the total phase is oscillating around $\vartheta = -\pi$ (value at which the coupling stops) , leading to the oscillations behind the first peak of the seed that are analogous of the π -pulse for the weak coupling regime. It was highlighted shown that the global phase is the relevant quantity that describes the efficiency of the coupling.

In many experimental situation of interest the pump laser is chirped: the dephasing originating from the chirped-pulse-generated lasers can affect the efficiency of the amplification. In particular if the dephasing is too large the coupling will be quenched, while an optimal condition can be found if the chirp can be used to maintain a favorable

coupling in the maximum seed growth, and pump depletion phase. In order to fulfill this condition, the parameter that needs to be taken into account is the sign of the chirp parameter α . Following the different stages of the amplification, we can define different values of the chirp parameter α that compensate the total phase variation. In correspondence of pump depletion, we have large energy transfer which is affecting the downshift of the seed frequency. Optimal coupling would then be achieved if the chirp phase compensates the seed phase at the moment pump depletion sets in. Imposing this condition, we find that the amplification is improved in terms of electric field amplitude and time definition of the width of the first peak when α is negative and of the order of $\alpha \approx -10^{-7}$. If the chirp parameter α is positive or too large the energy transfer is strongly reduced and the amplification quenched. We found that large values of α (of the order of $|\alpha| > 10^{-6}$ affect in a negative way the seed amplification, no matter the sign of α . A definite relation was established between the maximum growth rate γ_{sc} and the condition for the laser chirp to allow optimal amplification or to quench the process. We found that the sc-SBS amplification requires a preferential gradient of the plasma profile with respect to the seed propagation. When the amplification happens along a plasma density linearly decreasing as seen by the seed during its propagation, the seed enters earlier the exponential regime and the self-similar regime and it attains the highest amplification. In this case the seed amplification is even better compared to a simulation with a constant plasma with density equal to the average of the density ramp. This is similar to the case of the seed amplification with a negatively chirped pump. We defined an effective chirp associated to the density profile: for the case with a favorable density profile, the associated value is negative and the order of $\alpha_{trr} \approx -2.7 \times 10^{-7}$ confirming the previous finding about the relation between the sign of α and the increasing in the coupling efficiency. A definite relation was then established between the maximum growth rate γ_{sc} and the condition for the laser chirp to allow optimal amplification or to quench the process.

To further optimize and study the sc-SBS in more realistic configuration we carried out a series of one-dimensional particle in cell (PIC) simulations. As a result of our study, one dimensional PIC simulations appear as a necessary tool to describe most of the competing process (such as the SRS backscattering of the pump) and non-linearities intervening in the amplification mechanism. PIC simulations show larger downshifts and broader spectra than predicted by the linear theory, as well as asymmetric spectra, allowing the study of the coupling also in self-similar regime. In addition to the results obtained through the envelope simulations, we find that plasma shaping allows to partially control SRS affecting also the energy transfer. Typical experimental profiles of plasma produced from gas jet have gaussian shape and already help reducing significantly the spontaneous SRS. We found that the time synchronization between pump

and seed is a crucial parameter to enhance the coupling. In particular, we show that most of the energy transfer happens in the decreasing portion of the plasma density (as seen by the seed during its propagation), confirming the results obtained simply solving the sc-SBS system of equations. Amplification of a short seed is possible, however depending if the seed is low or high (relativistic) intensity, the amplification mechanism will be different. In the case of low intensity the seed stretches before entering in the self-similar regime. One dimensional PIC simulations helps to describe and interpret the quality of the amplification process obtained in experiments. As a results of our study, we demonstrated and validated the first experimental observation of the signatures of the transition from linear to self-similar regime as we also reported in [34]. The comparison among the spectra from experiments, PIC simulations and the previsions given by the sc-SBS linear theory confirms that the in the experiments the seed explores both a linear and self-similar regime of amplification. The importance of the relative delay between pump and seed pulses is confirmed also in experiment, in particular regarding the competition between SBS and SRS. The PIC simulations results demonstrate that, when the SBS amplification of the seed sets in, the growth of SRS is strongly limited.

In the last part of this work we presented the efforts made to develop and optimize the new particle in cell code SMILEI. This efforts made possible to carry out two dimensional sc-SBS amplification simulations on a very large scale, comparable to the real experiments one. We showed that, in an head-on configuration, the relative delay of interaction between pump and seed is an important parameter that allows to reach important seed intensity also in a two dimensional simulation. We then proposed a new possible set-up, in which a seed is amplified by two pump lasers counter-propagating with an angle of 6° with respect to the seed direction of propagation. This configuration allows one to limit the Raman backscattering of the pump along the seed propagation and reduces the deterioration of the initial focal spot of the seed.

To conclude, we showed the SBS amplification of short laser pulses in the strong coupling regime can be one of the opportunity to overcome present day limitations in terms of damage threshold of solid optics materials. It was shown that a detailed analysis of the combined temporal evolution of amplitude and phase in the strong coupling regime allows to clarify several issues in plasma amplification: the directionality of the energy flow, and the role of the chirp originating from the laser pulse and the plasma profile. Together with the parameters optimization obtain through PIC simulations, these results possibly allow a better interpretation and an improvement of nowadays experiments on SBS amplification. This analysis is also of importance to inertial confinement fusion (ICF) in the context of cross-energy beam transfer as the interaction conditions can be in strong-coupling.

Communications related to this thesis

Several parts of this work have been communicated to the scientific community. We give here a list of publications in peer-reviewed journals and a list of presentations in conferences and seminars.

List of publications:

1. M. Chiaramello, C. Riconda, F. Amiranoff, J. Fuchs, M. Grech, L. Lancia, J.-R. Marquès, T. Vinci, and S. Weber. "Optimization of interaction conditions for efficient short laser pulse amplification by stimulated Brillouin scattering in the strongly coupled regime". In: *Physics of plasmas*, **23**, 072103, 2016. doi: 10.1063/1.4955322.
2. M. Chiaramello, F. Amiranoff, C. Riconda, and S. Weber. "Role of frequency chirp and energy flow directionality in the strong coupling regime of Brillouin-based plasma amplification". In: *submitted to Physical Review Letters*
3. L. Lancia, A. Giribono, L. Vassura, M. Chiaramello, C. Riconda, S. Weber, A. Castan, A. Chatelain, A. Frank, T. Gangolf, M.N. Quinn, J. Fuchs, and J.-R. Marquès. "Signatures of the Self-Similar Regime of Strongly Coupled Stimulated Brillouin Scattering for Efficient Short Laser Pulse Amplification". In: *Physical Review Letters*, **116**, 075001, 2016. doi:10.1103/PhysRevLett.116.075001.
4. M. Chiaramello, J. Dérouillat, M. Flé, C. Riconda and M. Grech. "SMILEI - Amplification Brillouin de faisceaux laser ultra-courts". In: *La Lettre de l'IDRIS*, 2016.
5. J. Dérouillat, A. Beck, F. Pérez, T. Vinci, M. Chiaramello, A. Grassi, G. Bouchard, J. Dargent, N. Aunais, M. Flé, I. Plotnikov, C. Riconda and M. Grech. "Smilei:

a collaborative, open-source, multi-purpose particle-in-cell code for plasma simulation". *In preparation*

List of first author presentations at conferences:

Oral presentations

1. *Novel Light Sources from Laser-Plasma Interactions Workshop 2015*, Dresden. "Studies of stimulated Brillouin amplification of short laser pulse in the strong coupling regime".
2. *American Physical Society Plasma Conference 2015*, Savannah GA. "Plasma-based laser-pulse amplification via strongly coupled Brillouin scattering".
3. *Invited seminar at Los Alamos National Laboratory, 2015*, Los Alamos NM. "Plasma-based laser-pulse amplification via strongly coupled Brillouin scattering".
4. *European Physical Society Conference on Plasma Physics 2016*, Leuven. "Efficient laser pulse amplification by stimulated Brillouin scattering in strongly coupled regime"

Poster presentations

1. *European Physical Society Conference on Plasma Physics 2014*, Berlin. "Presentation of the SMILEI code and studies of amplification parametric instabilities"
2. *Forum Institut Laser Plasma 2015*, Porquerolles. "Plasma-based laser-pulse amplification via strongly coupled Brillouin scattering"

Appendices

Appendix A

Relation between the chirp parameter α and the duration of a gaussian laser beam

In this appendix we explicitly derive the relation between the chirp parameter α and the duration of gaussian laser beam finite in time. To do so, we first write the expression of the temporal evolution of the intensity in the case of a gaussian laser beam in a given point in the space, making the hypothesis that is centered around ω_0 :

$$I(t) = I_{max} e^{-t^2 / (\tau_{FWHM} / (2\sqrt{\ln 2}))^2} = I_{max} e^{-t^2 / \tau^2} \quad (\text{A.1})$$

In Eq.(A.1), I_{max} is the maximum value of intensity and the peak of the gaussian, τ_{FWHM} is the minimal duration of the pulse at the Full Width Half Maximum and τ is the minimal pulse duration (corresponding to a given spectral spread) defined as:

$$\tau = \frac{\tau_{FWHM}}{2\sqrt{\ln 2}} \quad (\text{A.2})$$

In the same way, the electric field can be written as:

$$E(t) = E_{max} e^{-t^2 / 2\tau^2} e^{-i\omega_0 t} \quad (\text{A.3})$$

where E_{max} is the electric field peak amplitude and ω_0 is the nominal frequency at E_{max} . If we make the Fourier transform of Eq.(A.3) we obtain:

$$E(\omega) \propto \tau e^{-(\omega - \omega_0)^2 \tau^2 / 2} \quad (\text{A.4})$$

The spectral width of the electric field is then:

$$\Delta\omega = \frac{\sqrt{2}}{\tau} \quad (\text{A.5})$$

The spectral width at FWHM in intensity is:

$$\Delta\omega_{FWHM} = \frac{4\ln 2}{\tau_{FWHM}} \quad (\text{A.6})$$

In the introduction we showed that the effect of a chirp, in terms of phase, can be expressed, in a given point as:

$$\phi(t) = \alpha\omega_0^2(t - t_0)^2 \quad (\text{A.7})$$

where α is the chirp parameter and t_0 is the time centering of the pump. For $t_0 = 0$ the chirp modify the spectral form of the electric field as:

$$E(\omega) \propto \tau e^{-(\omega - \omega_0)^2 \tau^2 / 2} e^{i\beta(\omega - \omega_0)^2} \quad (\text{A.8})$$

where $\beta(\omega - \omega_0)^2$ is the spectral contribution of the chirp to the electric field. Eq.(A.8), in terms of temporal dependance, reads now:

$$E(t) \propto e^{-t^2 / (2\tau^2 + 8\beta^2 / \tau^2)} e^{i \frac{\beta}{\tau^4 + 4\beta^2} t^2} = e^{-t^2 / 2T^2} e^{i\alpha\omega_0^2 t^2} \quad (\text{A.9})$$

with T defined as the duration of the chirped pulse

$$T = \sqrt{\tau^2 + 4\beta^2 / \tau^2} \quad (\text{A.10})$$

and

$$\alpha\omega_0^2 = \frac{\beta}{\tau^4 + 4\beta^2} \quad (\text{A.11})$$

Combining Eq.(A.10) and Eq.(A.11) we find a relation between the chirp parameter α and the durations T and τ :

$$\alpha\omega_0^2 \tau^2 = \frac{1}{2} \frac{\tau}{T} \sqrt{1 - \frac{\tau^2}{T^2}} \quad (\text{A.12})$$

In Fig.(A.1) we show the numerical solution of Eq.(A.12): notice that Eq.(A.12) dictates that a chirped laser beam has a longer duration compared to a not-chirped one and that for each value α there are two possible solution of τ/T . The chirp parameter is limited to:

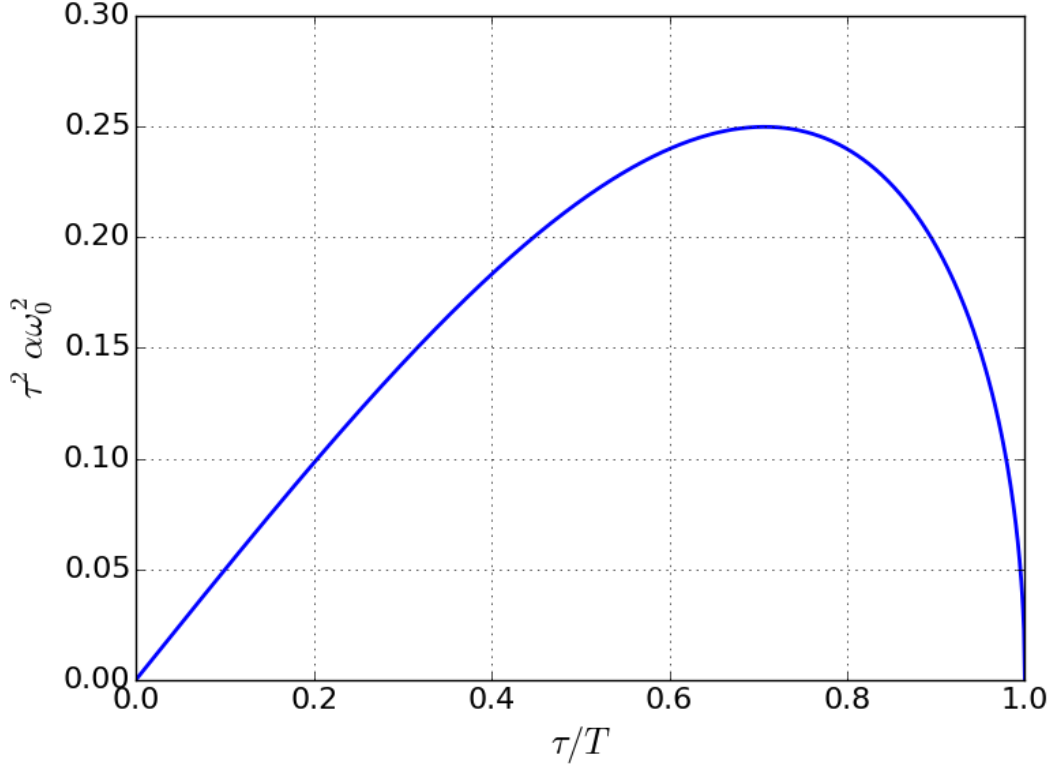


Figure A.1: Numerical solution of Eq.(A.12)

$$|\alpha| < \frac{1}{4\omega_0^2\tau^2} \quad (\text{A.13})$$

For each value of α there are then two solutions that are:

$$\frac{T^2}{\tau^2} = \begin{cases} \frac{2}{1+\sqrt{1-16\alpha^2\omega_0^4\tau^4}} & \text{if } \frac{\tau}{T} \geq \frac{1}{\sqrt{2}} \\ \frac{2}{1+\sqrt{1+16\alpha^2\omega_0^4\tau^4}} & \text{if } \frac{\tau}{T} \leq \frac{1}{\sqrt{2}} \end{cases} \quad (\text{A.14})$$

Eq.(A.14) can now be written in terms of minimal duration at FWHM:

$$\frac{T_{FWHM}^2}{\tau_{FWHM}^2} = \begin{cases} \frac{2}{1+\sqrt{1-\frac{\alpha^2\omega_0^4\tau_{FWHM}^4}{(\ln 2)^2}}} & \text{if } \frac{\tau_{FWHM}}{T_{FWHM}} \geq \frac{1}{\sqrt{2}} \\ \frac{2}{1+\sqrt{1+\frac{\alpha^2\omega_0^4\tau_{FWHM}^4}{(\ln 2)^2}}} & \text{if } \frac{\tau_{FWHM}}{T_{FWHM}} \leq \frac{1}{\sqrt{2}} \end{cases} \quad (\text{A.15})$$

In this work we generally consider laser beams much longer than the minimal duration: in that case Eq.(A.12) can be approximated as:

$$|\alpha| \approx \frac{1}{2\omega_0\tau T} \quad (\text{A.16})$$

In terms of durations at FWHM, Eq.(A.16) reads:

$$|\alpha| \approx \frac{2\ln 2}{2\omega_0\tau_{FWHM}T_{FWHM}} \approx \frac{1.38}{2\omega_0\tau_{FWHM}} \quad (\text{A.17})$$

Appendix B

SMILEI’s performance and capabilities

In this annex we briefly show the SMILEI’s structure and performances, focusing on the efforts made on the parallelization. SMILEI’s objectives are high performances, a large user community and support for a variety of applications. Its architecture reflects these goals: a modern C++ approach provides structure to separate physics and computing components, encourage their progress, facilitate their maintainability and ensure a multi-purpose capability.

C++ elements and flow

SMILEI’s core program is written in the C++ language. Its multi-purpose and mature technology ensures great flexibility and strong support for the new HPC machines. Moreover, C++’s object-oriented programming provides an efficient way of structuring the code. Importantly, this eliminates a few bad habits such as passing large lists of parameters through functions, or usage of global variables, inefficient in parallel computing. Components can be constructed almost independently. It offers a good separation between the purely computing or performance aspects and the physics calculations.

Figure B.1 shows the various elements of SMILEI’s main code: C++ classes, data structure, and the program flow. The main classes, namely “Particle species” and “Electro-magnetics”, are the counterparts of *particle* and *cell* in *Particle-in-cell*, respectively. The particle species hold the particles object, which is the data structure for the particles positions and momenta. It also contains operators on the particles: the boundary conditions and the pusher. On the other side, the Electro-magnetics class contains the fields, i.e. the data structure for the electric and magnetic fields. Note that these fields also describe the charge and current densities as projected on the grid.

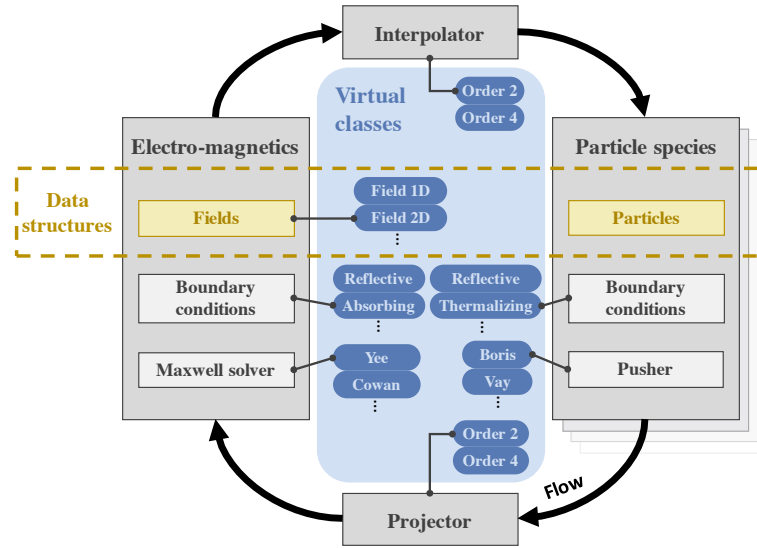


Figure B.1: C++ flow, classes and data structure in SMILEI.

Electro-magnetics also includes operators: boundary conditions for the fields and the Maxwell solver.

Two additional operators are external to those structures because they operate between particles and fields. The interpolator takes the field data and interpolates it at the particles positions. The projector takes the particle data and projects it at the grid points.

Polymorphism

The C++ language supports the definition of *polymorphic* classes. These classes contain functions (or other members), called *virtual functions*, that are selected at runtime among several options. In other words, the content of an object is not decided *a priori*, but may be defined during the simulation by choosing the class from which it is created. SMILEI relies on C++ polymorphism to handle its multi-purpose ambition. All these derived classes inherit their functions from the base class, but they include different data structures. In Fig.B.1, examples of polymorphic (*virtual*) classes are highlighted. Note that, in SMILEI, selecting the class, from which each object will be created, is ensured by a “factory design pattern”. There are several advantages to polymorphism. First, it allows for straightforward inheritance of properties between objects of similar structures. It also improves the readability of the code by removing the complexity of all the multi-purpose capabilities from the program flow. Lastly, it standardizes the form of the objects for easier maintenance. In these conditions, a single executable file can perform simulations in various dimensions, interpolation orders, or physics components,

without the complexity of many code versions. However, an excess of virtualization, or a large number of objects layers could have a significant computational cost. For instance, the use of a virtual method to access a single data element (e.g., a single particle property) would have an unacceptable data access overhead. This pitfall is avoided by passing the whole data structures to computational operators. They are passed in their virtual form, then cast to their particular class.

Uncoupling operators from data

An other fundamental ambition of the project is to provide an efficient tool of simulation on current and future supercomputers whose architectures are in permanent evolution. For instance, they may have complex memory hierarchy, whether distributed or shared between several processors. For ideal performances, the code must be adapted to these specific architectures. This is a major challenge in the context of a multi-purpose code: genericity contradicts the wide range of supercomputing targets.

SMILEI’s solution, based on its object-oriented architecture, consists in uncoupling computing algorithm from data formalism. Operators can thus be defined independently from the chosen data structure, provided the “protocol” for accessing to the data is respected. As a consequence, performances can be optimized separately in operators and in the data structures.

Along the same principle, parallelism management tends to be decoupled from the physics calculations by implementing different levels of parallelism.

HDF5 data management

A significant amount of output data is generated by PIC simulations, as described in Sec. B. We examine here the representation of these data, focusing on (i) the data access convenience and (ii) the performances on a large super-computer.

Classical output management would simply consist in gathering data on a “master” processor which writes everything out, or in generating one file for each processor. The former technique is limited by the cost of communicating data and its memory overhead, while the latter requires heavy post-processing simulations. In both cases, the larger the simulation, the more expensive the overhead.

Modern, parallel libraries for file output have now emerged. They can share and write data in parallel to a single file. Famous examples are *MPI-IO*, *HDF5* (*Hierarchical Data Format*) and *NetCDF* (*Network Common Data Form*).

Although no file-output parallelism matches the performances of the modern computing parallelism techniques, they greatly enhance the simulations efficiency. While *MPI-IO* has the best performances, it generates unformatted data. To analyze it,

dedicated tools must be implemented. *HDF5* and *NetCDF* are similar to each other, as they are also a structured data model, open-source and widely used. Note that *NetCDF* is now based on *HDF5*’s structure. While *HDF5* is fairly generic, *NetCDF* is specialized and wide-spread among the climate-modeling community.

SMILEI uses *HDF5* for its parallel performances and its multi-purpose structured data model. Additionally, this format benefits from a large panel of open-source software for post-processing and visualization.

Parallelization

As high-performance computing (HPC) systems are evolving towards the exascale, there is an admitted risk that today’s algorithms and softwares will be subpar, at best, for the upcoming architectures. Manufacturers have been unable to improve the existing “standard” microprocessor technologies for the last decade. Instead, the trend is oriented towards the multiplication of the number of computing units by several orders of magnitude rather than their improvement. This is achieved either with co-processors, or with massively multi-core processors. In order to face this emerging complexity, modern codes must expose a tremendous amount of parallelism while conserving data locality and minimizing load imbalance. We first present the overall parallelization strategy chosen for SMILEI, and follow with accurate descriptions of its elements.

Strategy

For the sake of generality, all fundamental computing items (cores, MPI processes, openMP threads, cuda threads, openCL work items, etc.) will be referred to as computing elements (CE) in this subsection.

The difficulty in parallelizing a PIC code lies in the coupling between the mesh and particle aspects of the code. In a typical run, most of the load is carried by the particles. It is therefore very tempting to distribute particles equally between CEs: benefits would be huge. First, simplicity. No particle communications are required because particles only interact with fields and are independent from each other. Second, an almost perfect load balance is maintained at all times. The drawback of this approach is that it implies that all CEs have access to a shared global array of grid quantities (fields and currents). These accesses must be synchronized and require frequent global communications which, in practice, prevent any form of scalability above a couple hundreds of CEs.

A purely particle-based decomposition being impossible, we must apply a mesh-based decomposition technique. Domain decomposition is the technique used in all

state-of-the-art PIC codes such as Osiris [61] or Calder-Circ [59] in laser-plasma interaction or Photon-Plasma [60] in astrophysics. It has shown very good scalability but comes with a cost. As most of the computational load is carried by particles, having a mesh-based decomposition is inconvenient. Its implementation is not straightforward and load balance is very difficult to achieve. The biggest issue is that particles are volatile objects traveling throughout the entire domain, forcing (1) communications between CEs when particles cross their local domain boundary, and (2) random access to the grid at every interpolation and projection phases. Communications are limited to neighbor domains and are not a fundamental threat to performances or scalability. The randomness of the particles positions is much more concerning. Random access to the grid arrays breaks the principle of data locality, paramount to the performance via a good cache use. Conversely, a proper access to the data avoids multiple load operations when the same data is used several times. And on top of that, if the access is well organized, SIMD operations can be executed and accelerate the computation by a significant amount.

Most of the time, this issue is addressed by sorting particles. Different kind of algorithms can ensure that particles close to each other in space are also well clustered in memory. Particles can be sorted at the cell level by a full count-sort algorithm every now and then during the simulation, or they can be subject to a more lax but more frequent sorting.

Note that the domain decomposition technique is already a form of sorting. Particles of a given sub-domain are naturally stored in a compact array of memory and attached to the grid portion they can interact with. If each sub-domain is sufficiently small to fit in the cache, very good performances can be achieved. This approach is the one used in SMILEI. It is a very fine-grain domain decomposition referred to as “patch-based” decomposition where patches denote the very small sub-domains. In addition, SMILEI still performs a very lightweight particle sorting within the patches in order to minimize cache misses. It brings a convenient flexibility in patches size without loss of performances because the particles remain well sorted even if the patches are large.

A patch-based MPI + openMP implementation

SMILEI’s implementation follows the so called “patch-based” approach described in [58]. It consists in a very fine grain domain decomposition where each sub-domain is referred to as a patch. It uses an MPI + openMP implementation. The Message Passing Interface (MPI) provides a mean to address a distributed memory system, compulsory in any HPC code. OpenMP is used to share computational load within the shared memory nodes of the system with a reduced programming complexity. Coupling the two standards provides both good scalability and load balancing, as explained in

this section.

Patches organization and distribution

The first layer of parallelism in SMILEI is achieved by an almost standard domain decomposition. The principle is straightforward. The simulation box is divided into sub-domains. These sub-domains are independent of each other and can therefore be treated in parallel. In a standard MPI approach, each MPI process handles one sub-domain. In the “patch-based” approach implemented in SMILEI, the simulation box is divided into many more sub-domains than there are MPI processes. It follows that each MPI process has to handle many patches instead of a single traditional sub-domain. At this point, it is important to understand that patches still have all the characteristics of traditional sub-domains. Each of them owns its own set of particles and its local grid part on which fields and current densities are defined.

The obvious cost of this fine grain domain decomposition is an additional, but necessary, synchronization between patches. Synchronization between patches belonging to the same MPI process is very cheap. It consists in a simple copy of a relatively small amount of ghost cells and exchange of particles in a shared memory system. Synchronization becomes more expensive when it occurs between patches belonging to different MPI processes. In that case, data has to be exchanged through the network between distributed memory systems via costly calls to the MPI library. In order to limit this cost, we need a flexible distribution policy of the patches between the different MPI processes which minimize MPI calls. This is achieved by organizing patches in a compact manner following a space-filling curve, i.e. a curve passing once and only once in each patch. There are many types of space-filling curves; the Hilbert curve was chosen for SMILEI. An example of the Hilbert curve is given in Fig. B.2. This curve is divided into as many segments as MPI processes and each process handles one of these segments. The mathematical properties of the Hilbert curve guarantees that these segments are compact in space (see Fig. B.2).

OpenMP parallelization and load balancing

Patch-based decomposition, in addition to its cache efficiency, is a very convenient way to expose a lot of local (inside MPI sub-domains) parallelism. Each patch being independent, they can be easily treated in parallel by the threads owned by the MPI process. Without this structure, the projection of particles might result in race conditions (threads overwriting each other’s computation) and would require costly atomic operations.

In SMILEI, patches are treated by openMP threads. In practice, this allows the user

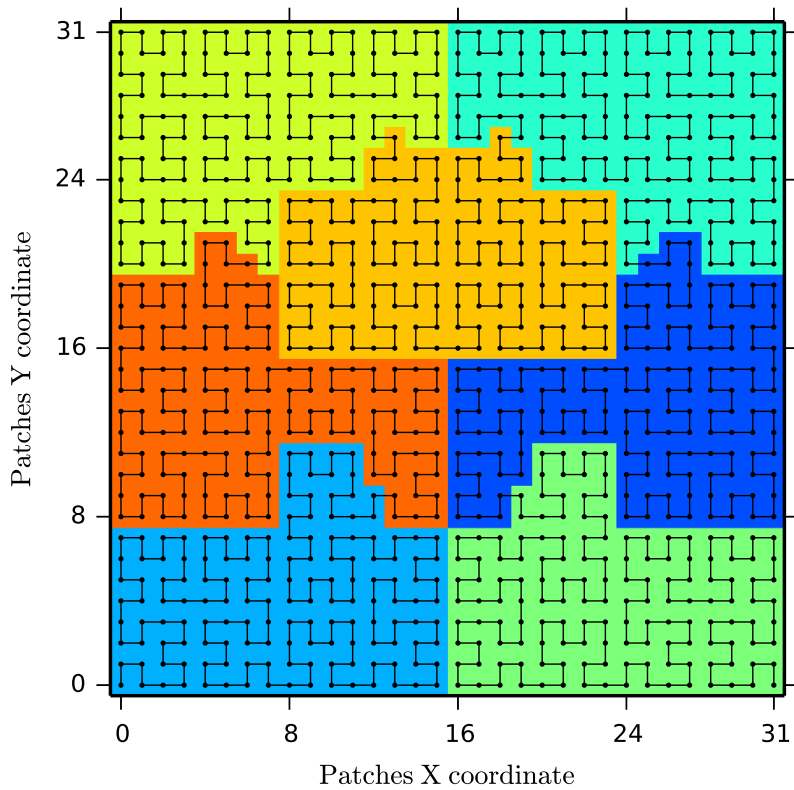


Figure B.2: Example of a 32×32 -patches domain decomposition, shared between 7 MPI processes. MPI domains are delimited by different colors. The Hilbert curve (black line) passes through all the patch centers (black dots). It starts from the patch with coordinates (0,0) and end at patch with coordinates (31,0).

to start the simulation with less but larger MPI domains than in a pure MPI implementation. A similar level of computational performance is retained while decreasing the global amount of communications. The number of macro-particles per patch may differ significantly and so does the associated computational load. The use of the openMP dynamic scheduler therefore provides local load balancing at a reasonable cost. If a thread is busy treating a patch with a lot of macro-particles, other threads will be able to handle the remaining lighter patches thus avoiding idle time. This is well illustrated in figure B.4.

Patches also act as sorting structures because particles of a given patch only interact with this patch's local grid. Small patches therefore provides a finer grain load balancing and optimized cache use at the cost of more inter-patch synchronization.

Load management

The objective of load management is to share the computational workload between the MPI processes as homogeneously as possible, thus to avoid idle, underloaded processes waiting for overloaded processes. In SMILEI, this is achieved by dynamically balancing the load.

We have seen that openMP already provides some amount of load balancing at the node level. But it doesn't help managing the load at the scale of the whole system. In SMILEI, the complete simulation workload is divided into independent and small packages: the patches. Dynamic load balance is achieved by exchanging these portions of workload between MPI processes. This technique is efficient because a single patch workload is much smaller than the total workload of a process. The patch size defines the balance grain and the smaller the patches the smoother the balance.

This is yet another argument in favour of using patches as small as possible. At this point, it becomes interesting to understand what limits the patch size. The minimum size of a patch is dictated by the number of ghost cells used. It sounds reasonable to consider that a patch must have more cells than ghost cells. The number of ghost cells is defined by the Maxwell equations discretization scheme order and shape function of the macro-particles. For a standard second order Yee scheme for instance, 4 ghost cells are used per dimension (2 for each direction). The minimum patch size in that case is therefore 5 cells per dimension. This criteria also guarantees that ghost cells from non neighbour patches do not overlap which is convenient for the synchronization phases.

We have seen that patches are organized along a Hilbert space-filling curve divided into as many segments of similar length as there are MPI processes. Each process handles the patches located in its segment of the Hilbert curve. Dynamically balancing the load simply consists in exchanging patches between neighbour MPI processes along the curve. That is to lengthen or shorten the segments depending on how loaded they

are. When an MPI processes is overloaded, it sends patches to its neighbours along the Hilbert curve; therefore its segment becomes shorter. Inversely, an underloaded process will receive patches from its neighbours; its segment becomes longer. Patches are always exchanged along the Hilbert curve in order to retain its important locality property which is still valid for segments of different lengths.

First, the computational load L_p of each patch p is evaluated as

$$L_p = N_{\text{part}} + C_{\text{cell}} \times N_{\text{cells}} + C_{\text{frozen}} \times N_{\text{frozen}} \quad (\text{B.1})$$

where N_{part} is the number of active particles in the patch, N_{cells} is the number of cells in the patch, N_{frozen} is the number of frozen (immobile) particles in the patch, and C_{cell} and C_{frozen} are user-defined coefficients representing the computational cost of cells (mostly solving Maxwell equation) and frozen particles. In most cases, the active particles are the major source of computational load. By default SMILEI uses $C_{\text{cell}} = 1$ and $C_{\text{frozen}} = 0.1$. The total computational load is $L_{\text{tot}} = \sum_p L_p$ and the optimal computational load per process $L_{\text{opt}} = L_{\text{tot}}/N_{\text{MPI}}$, where N_{MPI} is the number of MPI processes. The balancing algorithm proceeds to a new decomposition of the Hilbert curve so that each segment carries a load as close to L_{opt} as possible. This balancing process is typically done every 20 iterations in order to follow the dynamics of the simulation. Frequent and small corrections give superior performance than rare and dramatic adjustments (see figure ??).

The amplitude of the readjustment is limited in the “movement limitation” phase: each MPI process keeps at least one of its original patches. This reduces the performance impact of strong, high-frequency, oscillatory variations of the load observed in certain cases. Once the segments are defined, the actual exchange of data is done.

Performances and scaling

This section illustrates the efficiency of the chosen parallelization strategy and gives some insight on the optimization of the numerical parameters available to the user.

MPI

Here, the impact of the MPI parallelization is studied. Figure B.3 displays SMILEI’s strong scaling in the case of an homogeneous plasma and a pure MPI parallelization. The same simulation is run on different number of cores and a single MPI process is attached to each core. As the number of cores increases, the size of the data handled by each core, or “domain size”, decreases. The efficiency remains close to 100% as long as the domain size remains larger or equal to the L1 cache size. As the domain size approaches the L1 size, a superlinear effect improves the performances a bit but efficiency

drops as the domain size becomes significantly smaller than the cache. At this point, the system computing units occupation is too small to deliver proper performances. Figure B.3 illustrates the fact that MPI communications perform well in SMILEI: there is no significant overhead, their costs is much smaller than the computation in a standard case.

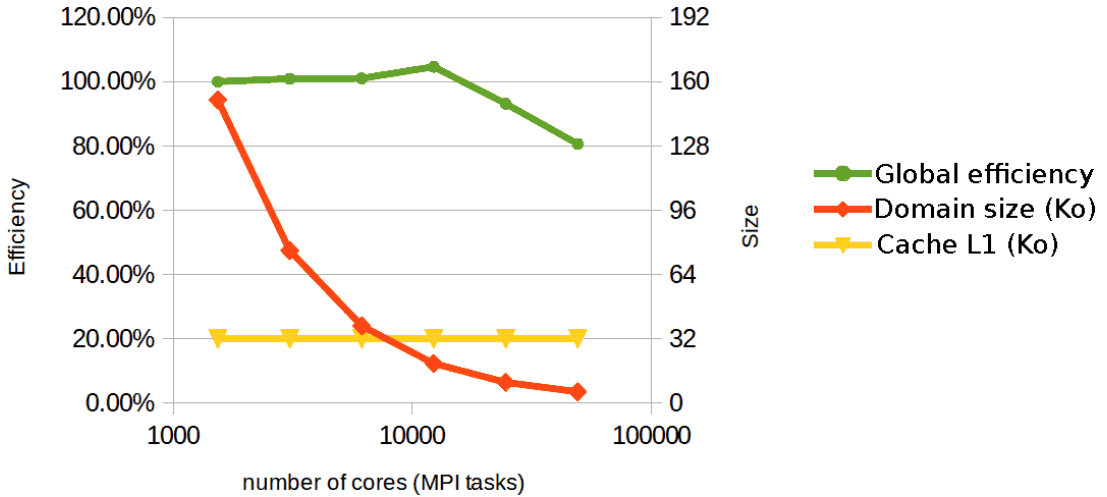


Figure B.3: Pure MPI strong scaling of SMILEI in an homogeneous plasma case on the OCCIGEN system.

MPI + openMP

It came out of the previous section that the MPI parallelization is good at handling homogeneous plasmas as long as the sub-domains sizes are not too small with respect to the L1 cache. In this section we present the performances achieved with the hybrid MPI+openMP parallelization when the plasma does not remain homogeneous.

The case study is now, and until the end of the section, an ultra-high-intensity laser propagating in a plasma. It is a two-dimensional simulation consisting of 1024×128 patches, each having 8×5 cells and 200 particles per cell. Each run ran on 32 nodes of the OCCIGEN system. This represents 64 processors of 12 cores each for a total of 768 cores. The plasma is initially homogeneous but load imbalance builds up at the start and rises quickly after 6000 iterations before stabilizing.

Figure B.4 shows the evolution of the wall-clock time necessary to complete 100 iterations as a function of the number of iterations already completed for different numerical settings. The runs only differ by the number of openMP threads per MPI process and total number of MPI processes. The total number of threads is kept constant and equal to 768 in order to have 1 thread per core. The openMP dynamic scheduler is used in all cases.

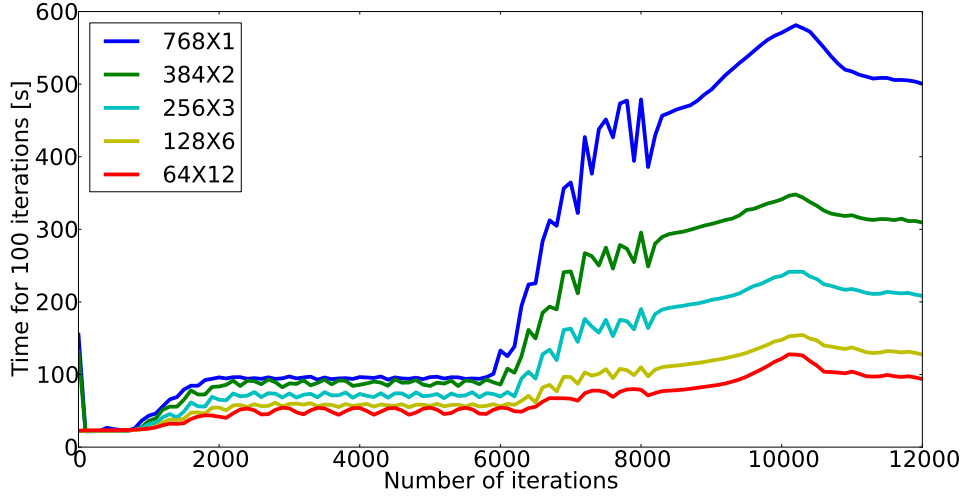


Figure B.4: OpenMP load balancing effect. The plot displays the evolution of the wall-clock time necessary to complete 100 iterations as a function of the number of iterations already completed. The legend shows the total number of MPI processes and number of openMP threads per MPI process in the format MPI \times openMP.

Several interesting features can be noticed on figure B.4. First, as long as the plasma is relatively homogeneous (first 1000 iterations) all runs perform similarly. It means that the overhead for having an hybrid parallelization is negligible in this case. Later in the simulation, the pure-MPI case shows an extreme sensitivity to the load imbalance. The wall-clock time spent to perform 100 iterations is almost multiplied by 20 with respect to the initial homogeneous plasma. Cases using more than one openMP thread per MPI process are much less sensitive to this effect. And the more threads per MPI process, the smoother the performances. This is perfectly in line with the local load balancing analysis given in section B. Nevertheless, even in the best case 64×12 , a performance loss of a factor superior to 4 is still impacting the simulation. This is explained by the fact that openMP can only balance the load within a given MPI domain. Imbalance across MPI domains will keep slowing the simulation down.

Using more openMP threads, or equivalently more cores, per MPI process allows the use of larger MPI domains and therefore provides a better load balancing. But the number of openMP threads is limited to the number of cores accessible on the shared memory system. In our case, this is a single OCCIGEN node made of two processors of 12 cores each so up to 24 openMP threads could be used. But going from 12 to 24 openMP threads per MPI process results in a drop of the performances because of the synchronization required between the two processors of the node. The best performances are achieved when a single MPI process is given to each processor and

when all cores of the processor are managed by the openMP scheduler. The quality of the load balancing via the openMP dynamic scheduler thus directly depends on the size (in number of cores) of the processors composing the nodes.

MPI + openMP + dynamic load balancing

This section presents results obtained with the dynamic load balancing (DLB) algorithm described in section B. Figure B.5 shows a comparison between the two best cases obtained in the previous section (without DLB) and the same cases with DLB activated.

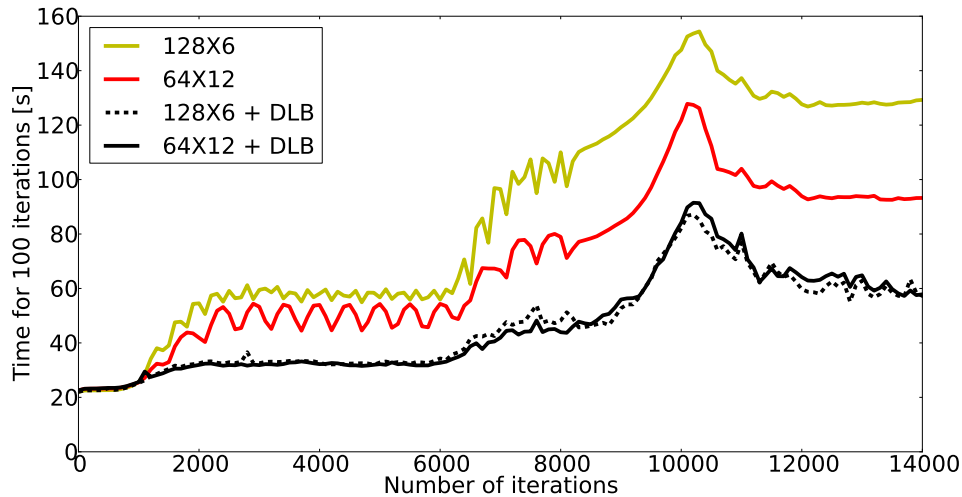


Figure B.5: Dynamic load balancing (DLB) algorithm effect. The plot displays the evolution of the wall-clock time necessary to complete 100 iterations as a function of the number of iterations already completed. The legend shows the total number of MPI processes and number of openMP threads per MPI process in the format MPI \times openMP. The red and yellow curves are replicas of figure B.4.

The balancing here is done every 20 iterations and $C_{\text{cell}} = 2$. No difference is observed during the balanced stage of the run (first 1000 iterations). As expected, the cost of the balancing is negligible when actual balancing is not required. In the imbalanced stage of the run, DLB provides an additional gain of almost 40% with respect to the previous best case “64 \times 12”. A side benefit is also to reduce the dependency on the large number of openMP threads. Indeed, it appears that almost similar results are obtained with only 6 openMP threads when DLB is active. As DLB balances the load between MPI processes, the local balancing via openMP becomes much less critical than before. Note that the openMP parallelization remains necessary for an efficient fine grain balancing but it can be achieved with only a limited number of threads thus

removing the dependency on a large shared memory hardware.

Note also that the cost of the imbalance is still significant in spite of all the efforts to balance the load. The additional cost is mainly due to the imbalance of the particles communication cost which is not as well balanced as the computational cost of particles.

User interface:Python input file

End-users need only know how to write an input file, which we call *namelist*. Although the core of SMILEI is written in C++, the namelist is written in the *python* language. This has many advantages over the typical text-only inputs. Indeed, *python* can process complex operations that may be necessary to initialize the simulation. It can generate arbitrary numbers of simulation elements at run-time, without the help of an external script (which would have to be pre-processed). It supports thousands of additional packages, often helpful for specific physics calculations. It is widely used and becoming a reference for all sorts of applications. Very importantly, *python* functions can be passed as arguments to SMILEI. For instance, a density profile can be directly defined as a function of the coordinates.

When SMILEI is run, it starts a *python* interpreter that parses the namelist line-by-line, and executes all the *python* commands. Throughout the initialization of the simulation elements (particles, fields, diagnostics, etc.) the interpreter stays active. SMILEI gathers required data from it, processes all required initialization steps, and finally closes the interpreter. Note that, if a *python* function needs to be evaluated throughout the simulation, the interpreter is kept active at all times. This happens, for instance, when defining a custom temporal profile for a laser envelope.

Diagnostics

Data collection and analysis are performed by *diagnostics*. They are not post-processing modules, but are part of the main code and executed *in situ*. All of these diagnostics have the capability of being performed only at user-defined times during the simulation.

Scalar diagnostic – The simplest diagnostic is called *scalars*: it processes a large set of field and particle data, and combines the results from all processors before writing out scalar quantities in a dedicated file. Among these quantities, one can find the overall energy balance (with contributions from the different fields, particles, and losses at the boundaries), averaged particle quantities (charge, energy, number of particles), and global field information (minima, maxima and Poynting flux through boundaries).

Fields diagnostic – The diagnostic *fields* provides a direct copy of all the arrays in the code, after concatenating them from all the processors. Note that, in addition of the **E** and **B** fields, the particle densities and currents are also written as they are projected

on arrays at each time-step. Moreover, these data may be temporally averaged over a number of time-steps requested by the user.

Probe diagnostics – The drawback of the diagnostic *fields* is that the whole arrays are written out. To reduce the file space footprint, the *probes* have been implemented: one *probe* corresponds to a series of points at which locations the fields are interpolated and written in a dedicated file. This series of points can be either regularly arranged in a line, in a rectangle (for a two-dimensional simulation), or in a parallelepiped (for a three-dimensional simulation). The spatial separations between consecutive points is defined by the user. Note that several *probes* can be added to a single simulation.

Trajectory diagnostics – Histories of individual particles are stored by the *tracking* diagnostic. Each species of particles may be *tracked* independently, with custom output frequencies. In order to follow individual particles, each tracked particle is assigned a unique number which is transported throughout the simulation with the particle.

Particle distribution diagnostics – Tracking the position of all particles with a high frequency would be time- and memory-consuming. To obtain digested particle data with flexible capabilities, the *particle diagnostic* has been implemented. One diagnostic is defined by an arbitrary number of *axes*, which overall define a grid: all the particles in the selected species deposit their weight in the grid cell they belong to (the cell size is independent of the PIC grid). These *axes* are not necessarily spatial (x , y or z), but can also be one of p_x , p_y , p_z , p , γ , v_x , v_y , v_z , v or the particle charge q . A large number of combinations can thus be designed. For instance, using one axis $[x]$ will provide the density distribution *vs.* x ; using two axes $[x, y]$ will provide the two-dimensional density distribution *vs.* x and y ; using one axis $[p_x]$ will provide the x -momentum distribution; using two axes $[x, p_x]$ provides the phase-space along x ; using three axes $[x, y, \gamma]$ provides density maps at different energies; using one axis $[q]$ provides the charge distribution. Further versatility is possible by choosing the particle quantity deposited, instead of simply the weights w . For instance, depositing $w q v_x$ results in the j_x current density and depositing $w v_x p_x$ results in a component of the pressure tensor. A final feature of these *particle diagnostics* is the capability for temporal averaging over an arbitrary number of time-steps.

Bibliography

- [1] P. Agostini, F. Fabre, G. Mainfray, G. Petite, and N. Rahman, Phys. Rev. Lett. **42**, 1127 (1979).
- [2] M. Ferray et al., Journal of Physics B **21**, L31 (1988).
- [3] M. Perry, A. Szoke, O. Landen, and E. Campbell, Phys. Rev. Lett. **60**, 1270 (1988).
- [4] T. H. Maiman, Nature **187**, 493 (1960).
- [5] J. H. Nuckolls, L. Wood, A. Thiessan, and G. B. Zimmermann, Nature **239**, 129 (1972).
- [6] H. Daido, Rep. Prog. Phys. **65**, 1513-1576 (2002)
- [7] R.W.Hellwarth,ColumbiaUniversityPress,NewYork,1961.
- [8] L. E. Hargrove, R. L. Fork, and M. A. Pollack, J. Appl. Phys. **5**, 4 (1964).
- [9] M. Perry and G. Mourou, Science **264**, 917 (1994).
- [10] M. D. Perry et al., Optics Letters **24**, 160 (1999)
- [11] C. E. Capjack, C. R. James, and J. N. McMullin, J. Appl. Phys. **53**, 4046 (1982)
- [12] M. Maier, W. Kaiser, and J. A. Giordmaine, Phys. Rev. Lett. **17**, 1275 (1966).
- [13] V. M. Malkin, G. Shvets, and N. J. Fisch, Phys. Rev. Lett. **82**, 4448 (1999); V. M. Malkin, G. Shvets, and N. J. Fisch, *ibid.* **84**, 1208 (2000); P. Mardahl, H. J. Lee, G. Penn, J. S. Wurtele, and N. J. Fisch, Phys. Lett. A **296**, 109 (2002); N. J. Fisch and V. M. Malkin, Phys. Plasmas **10**, 2056 (2003); V. M. Malkin and N. J. Fisch, *ibid.* **12**, 044507 (2005).
- [14] B. Ersfeld and D. Jaroszynski, Phys. Rev. Lett. **95**, 165002 (2005).
- [15] Raj, G., Ersfeld, B., Vieux, G., Yoffe, S., Hur, M. S., Cairns, R. A. and Jaroszynski, D.A., New Journal of Physics. **17**, 11 p., 103026 (2015).

- [16] Yang, X., Vieux, G., Brunetti, E., Ersfeld, B., Farmer, J. P., Hur, M. S., Issac, R. C., Raj, G., Wiggins, S. M., Welsh, G. H., Yoffe, S. R. and Jaroszynski, D. A. , Scientific Reports. **5**, 13333, (2015)
- [17] Vieux, G., Ersfeld, B., Farmer, J. P., Hur, M. S., Issac, R. and Jaroszynski, Applied Physics Letters. **103**, 12, 4 p., 121106, (2013)
- [18] Vieux, G., Lyachev, A., Yang, X., Ersfeld, B., Farmer, J. P., Brunetti, E., Issac, R., Raj, G., Welsh, G. H., Wiggins, M. and Jaroszynski, D., New Journal of Physics. **æbf13**, 9 p., 063042 (2011)
- [19] Yang, X., Vieux, G., Brunetti, E., Farmer, J. P., Ersfeld, B., Wiggins, M., Issac, R., Welsh, G. H. and Jaroszynski, D.A., (ed.) Bellingham, p. 80750G (Proceedings of SPIE ; vol. 8075) (2011)
- [20] Farmer, J. P., Ersfeld, B. and Jaroszynski, D.A., (ed.) Bellingham, (Proceedings of SPIE ; vol. 8075) (2011)
- [21] Farmer, J. P., Ersfeld, B. and Jaroszynski, D. A., **17**, 11, p. 113301 6 p. (2010)
- [22] Ersfeld, B., Farmer, J., Raj, G. and Jaroszynski, D. A., **17**, 083301 (2010)
- [23] N.A. Yampolsky et al., Phys. Plasmas **15**, 113104 (2008);
- [24] D. W. Forslund, J. M. Kindel, and E. L. Lindman, Phys. Fluids **18**, 1002 (1975).
- [25] B. Cohen and C. Max, Phys. Fluids **22**, 1115 (1979).
- [26] A. Frank, J.Fuchs, L. Lancia, G. Lehmann, J.-R. Marquès, G.Mourou, C. Riconda, K.H. Spatschek, T. Toncian ,L.Vassura, and S. Weber, Eur. Phys. J. Special Topics **223**, 1153-1156 (2014)
- [27] A.A. Andreev, C. Riconda, V. T. Tikhonchuk and S. Weber, Phys. Plasmas **13**, 053110 (2006).
- [28] C. Riconda, S. Weber, L. Lancia, J.-R. Marquès, G. Mourou, and J. Fuchs, Plasma Phys. Control. Fusion **57** 014002 (2015).
- [29] W. Kruer, *The Physics of Laser-Plasma Interaction* (Addison-Wesley,1988).
- [30] G. Lehmann, and K. H. Spatschek, Phys. Plasmas **20**, 073112 (2013).
- [31] F. Schluck, G. Lehmann and K. H. Spatschek, Phys. Plasmas **22**, 093104 (2015).
- [32] G. Lehmann, and K. H. Spatschek, Phys. Plasmas **23**, 023107 (2016).

- [33] S. Weber, C. Riconda, L. Lancia, J. R. Marquès, G. A.Mourou, and J. Fuchs, Phys. Rev. Lett. **111**, 055004 (2013).
- [34] L. Lancia, A. Giribono, L. Vassura, M. Chiaramello, C. Riconda, S. Weber, A. Castan, A. Chatelain, A. Frank, T. Gangolf, M.N. Quinn, J. Fuchs, and J.-R. Marquès, Phys. Rev. Lett. **116**, 075001 (2016)
- [35] M.Chiamello, C.Riconda, F.Amiranoff, J.Fuchs, M.Grech, L. Lancia, J.-R. Marquès, T. Vinci, and S. Weber, Phys. Plasmas **23**, 072103 (2016).
- [36] L. Lancia, J.-R. Marquès, M. Nakatsutsumi, C. Riconda, S. Weber, S. Hüller, A. Mančić, P. Antici, V. T. Tikhonchuk, A. Hééron, P. Audebert, and J. Fuchs, Phys. Rev. Lett. **104**, 025001 (2010)
- [37] M. Shoucri, J.-P. Matte and F. Vidal, Phys. Plasmas **22**, 053101 (2015).
- [38] R.M.G.M. Trines, E.P. Alves, K.A. Humphrey, R. Bingham, R.A. Cairns, F. Fiúza, R.A. Fonseca, L.O. Silva, and P.A. Norreys, arxiv:1406.5424v1 (2014)
- [39] M.N. Rosenbluth, Phys. Rev. Lett. **20**, 565 (1972)
- [40] E.P. Alves, R.M.G.M. Trines, K.A. Humphrey, R. Bingham, R.A. Cairns, F. Fiúza, R.A. Fonseca, L.O. Silva, and P.A. Norreys, arxiv:1311.2034v3 (2014)
- [41] G. Lehmann, F. Schluck, and K.H. Spatschek, Phys. Plasmas **19**, 093120 (2012).
- [42] C. Riconda, S. Weber, L. Lancia, J.-R. Marquès, G. A.Mourou, and J. Fuchs, Phys. Plasmas **20**, 083115 (2013).
- [43] Z.M. Sheng, J. Zhang, D. Umstadter, Appl. Phys. **77**, 673 (2003).
- [44] <http://www.maisondelasimulation.fr/projects/Smilei/html/index.html>
- [45] G. Lehmann and K.H. Spatschek, Phys. Rev. Lett. **116**, 225002 (2016)
- [46] I.N. Ross, Optical Parametric Amplification Techniques, T. Brabec (ed.), Strong Field Laser Physics, Springer (2008).
- [47] V. Malka, N. Renard-Le Galloudec, S. Hüller , D. Pesme, F. Amiranoff, S. D. Baton, A. Modena, Ph. Mounaix, C. Rousseaux and M. Salvati, Phys. Plasmas **7**, 4259 (2000).
- [48] Z. Toroker, V. M. Malkin, and N. J. Fisch, Phys. Plasmas **21** 113110 (2014)
- [49] M. R. Edwards, Z. Toroker, J. M. Mikhailova, and N. J.Fisch, Phys. Plasmas **22** 074501 (2015)

- [50] F. H. Harlow, *A Machine Calculation for Hydrodynamic Problems*, Los Alamos Scientific Laboratory report LAMS-1956 .
- [51] C. K. Birdsall and A. B. Langdon, *Plasma Physics via computer simulation*, (McGraw-Hill, New York, 1985).
- [52] A. Taflove and S. C. Hagness, *Computation Electrodynamics: The Finite-Difference Time-Domain Method*, 3rd Ed. (Artech House, Norwood, 2005).
- [53] R. Nuter, M. Grech, P. G. de Aleiza Martinez, G. Bonnaud and E. d'Humières, *Eur. Phys. J. D* **68**, 177 (2014).
- [54] J. P. Boris, *Relativistic plasma simulation - optimization of a hybrid code*, Proceeding of the 4th Conference on Numerical Simulation of Plasmas, Naval Res. Lab., Washington DC, pp. 3-67 (1970)
- [55] J.-L. Vay, *Phys. Plasmas* **15**, 056701 (2008).
- [56] T. Zh. Esirkepov, *Comp. Phys. Comm.* **135**, 144 (2001).
- [57] R. Lehe, *Improvement of the quality of laser-wakefield accelerators: towards a compact free-electron laser*, PhD. thesis, Ecole Polytechnique (2014).
- [58] K. Germaschewski, W. Fox, S. Abbott *et al.*, *J. Comput. Phys.* 318 (2016) 305–326.
- [59] A. F. Lifschitz, X. Davoine, E. Lefebvre *et al.*, *J. Comput. Phys.* 228 (2009) 1803–1814.
- [60] T. Haugbølle, J. Trier Frederiksen, Å. Nordlund, *Phys. Plasmas* 20 (2013) 062904.
- [61] R. A. Fonseca, L. O. Silva, V. K. Decyk, W. Lu, C. Ren, W. B. Mori, S. Deng, S. Lee, T. Katsouleas *et al.*, *Computational Science - ICCS 2002*, Springer, pp.342-351.

List of Figures

1.1	Different stages of the seed amplification schematically reproduced. . . .	9
1.2	Chirp phase $\phi_s(t)$ (a), frequency $\omega(t) - \omega_0$ (b) and wavelength $\lambda - \lambda_0$ (c) values in function of time and for $\alpha = 3.3 \times 10^{-7}$ (blue line) and $\alpha = -3.3 \times 10^{-7}$ (green line)	20
2.1	Electric fields amplitudes, in V/m , of the pump (blue line) and of the seed (green line) at the beginning (a) and after $t_{end} = 1.5 ps$ (b). The unperturbed density profile is in red, in arbitrary units.	28
2.2	a) Evolution in time of the phases of the pump (φ_p , blue line), of the seed ($-\varphi_s$, green line) and density perturbation ($-\varphi$, red line) in function of time and in units of π . b) Time evolution of the total phase ϑ as defined in Eq.(2.24), in units of π . The green shadowed regions indicate the values of ϑ for which the pump amplifies the seed; the blue ones corresponds to a reversed flow energy direction (the seed amplifies the pump). c) Electric fields amplitudes, in V/m , of the pump (blue line) and of the seed (green line) in function of time. All these results are evaluated at the initial crossing point of the lasers, $\hat{x} = 0$ ($x = 350\mu m$) .	29
2.3	Seed phase at the lasers crossing point $\hat{x} = 0$ and in function of time ($0 < t\gamma_{sc} < 2$: comparison between the results of φ_s from simulations (green line) and from the expression given in Eq.(2.35) (red line).	33
2.4	Comparison between the simulation results for the evolution of the plasma density perturbation phase (green line, $-\varphi$) and the estimation given by Eq.(2.40) (red line, $\varphi_s/6$), at $\hat{x} = 0$ and for $0 < t\gamma_{sc} < 2$	34

3.1	a) Evolution of seed phase $-\varphi_s$ for $0 < t\gamma_{sc} < t_{tot}\gamma_{sc}$, with $t_i\gamma_{sc} = 2$ and $t_{tot}\gamma_{sc} = 4.3$. b) Comparison among $-\varphi_s$ (green line), $-\varphi_s^{th} = \frac{2}{9\sqrt{3}}\gamma_{sc}^3 t^3$ as calculated in Eq.(2.35) (black line) and the chirp phase $-\phi(\alpha_i)$ calculated in Eq.(3.5) $\alpha_i = 1.28 \times 10^{-6}$ (red line), for $0 < t\gamma_{sc} < t_i\gamma_{sc}$ c) Comparison among $-\varphi_s$ (green line), $-\varphi_s^{th}$ as given by Eq.(3.1) (black line) and the chirp phase $\phi(\alpha_{tot})$ calculated in $\alpha_{tot} = -3.3 \times 10^{-7}$ (blue line), for $t_i\gamma_{sc} < t\gamma_{sc} < t_{tot}\gamma_{sc}$. d) Evolution of the seed frequency $\partial_t(-\varphi_s)$ (green dashed line) compared to the theoretical value $\partial_t^{th}(-\varphi_s) = \gamma_{sc}/\sqrt{3}$ (black dashed line) and the frequency variation due to the chirp $\partial_t\phi(\alpha_{tot})$ (blue dashed line). All the results shown here are calculated at the initial laser crossing point ($x = 350\mu m$).	43
3.2	Evolution in time of the phases of the pump (a) (φ_p), of the seed (b) ($-\varphi_s$), of the density perturbation (c) ($-\varphi$) and of the total phase (d) ϑ in function of time and in units of π , at $x = 350\mu m$. e) Electric fields amplitudes, in V/m , of the pump (blue lines) and of the seed (green lines) in function of time. The solid lines indicate the simulation results for $\alpha = 0$, the dashed ones are for $\alpha = \alpha_{tot}$. The shadowed region indicates the time interval in which the seed is exponentially amplified.	44
3.3	Electric fields amplitudes, in V/m , of the pump (blue lines) and of the seed (green lines) in function space, at $t = 1.5 ps$. The solid lines indicate the simulation results for $\alpha = 0$, the dashed ones are for $\alpha = \alpha_{tot}$	45
3.4	Electric fields amplitudes, in V/m , of the pump (blue lines) and of the seed (green lines) in function space, at $t = 1.5 ps$. The solid lines indicate the simulation results for $\alpha = 0$, the dashed ones are for $\alpha = \alpha_i$: in this case the amplification of the seed with a chirped pump laser is strongly quenched.	46
3.5	Evolution of the electric field amplitude of the seed in function of time at the initial crossing point of the lasers ($x = 350\mu m$) and for positive (a) and negative (b) values of α . The dashed black line indicates the maximum electric field amplitude for $\alpha = 0$	47
3.6	Evolution of the total phase ϑ (in units of π) as function of time at the initial crossing point of the lasers ($x = 350\mu m$) and for positive (a) and negative (b) values of α	47
3.7	Initial configuration of the lasers in function of space for the case $const_1$ (a), $const_2$ (b), trl (c) and trr (d)	58
3.8	Electric field amplitude of the seed in function of space (a) and time (b) (at $x = 550\mu m$) for the different plasma density shape considered.	59

3.9	Electric field amplitude of the seed in function of space for different plasma shapes and different values of chirp parameter α . The comparison is made among a case in which the plasma density is constant and the pump is chirped with $\alpha = \alpha^{trr} \approx -2.7 \times 10^{-7}$, ($const_2^{\alpha^{trr}}$), a case in which the plasma density is constant and $\alpha = \alpha^{trl} \approx 2.7 \times 10^{-7}$ ($const_2^{\alpha^{trl}}$), a case in which the plasma density is constant and the pump is not chirped ($const_2$) and the cases with a triangular plasma density profile (trl and trr). The inset shows the plasma density profiles considered.	61
3.10	Initial configuration of the lasers pulses (pump in blue, seed in green) for the simulations with constant lasers and a gaussian plasma profile (red line). The electric field amplitudes are shown in units of V/m and the density is arbitrary units.	65
3.11	Evolution of the electric field amplitude of the seed in function of time at $x = 350 \mu m$ for positive (a) and negative (b) values of α . In this series of simulations, both pump and seed laser are kept constant.	66
3.12	Electric fields amplitudes, in V/m , of the pump (blue lines) and of the seed (green lines) in function space, at $t = 2.6$ ps. The solid lines indicate the simulation results for $\alpha = 0$, the dashed ones are for $\alpha = -2 \cdot 10^{-7}$.	67
3.13	Initial configuration of the lasers pulses (pump in blue, seed in green) for the simulations with gaussian lasers and a gaussian plasma profile (red line). The electric field amplitudes are shown in units of V/m and the density is arbitrary units. The black dashed lines indicate the different crossing point considered. a) $x_{cross} = 500 \mu m$. b) $x_{cross} = 350 \mu m$. c) $x_{cross} = 200 \mu m$	69
3.14	Final seed electric field amplitude (in V/m) as function of space for different crossing points of the pump and seed lasers.	70
4.1	Pump laser propagating through a constant plasma at $t \approx 3.5$ ps since the beginning of the simulation (case constant). The red arrow indicates the direction of propagation of the laser. The backscattered light (RBS, in blue) propagates in the opposite direction. The green and yellow lines are the electrons and ions densities, respectively, normalized to $n/n_c = 0.05$	76

- 4.2 Spectrum in ω/ω_0 (a) and in k/k_0 (b) of electric field E_z , for a **constant** density profile. a)The frequency spectrum is integrated over 3.5 ps from the beginning of the simulation. The peak at $\omega/\omega_0 = 1$ corresponds to the nominal frequency of the pump laser. The black dashed line at $\omega/\omega_0 \approx 0.77$ indicates the Raman frequency in vacuum. b) The wavenumber spectrum is integrated over the entire simulation box size. The black dashed line at $k/k_0 \approx 0.72$ indicates the wavenumber of the Raman backscattered light in the plasma at a plasma density $n/n_c = 0.05$. 77
- 4.3 Pump intensity profile after 3.5 ps, in a **triangular** (a) and **gaussian** (b) plasma density configuration. The pump intensity, normalized to its maximum value $I_p^{max} = 10^{15} \text{W/cm}^2$ is shown in red; the green lines indicate the normalized electron density. The yellow lines (partially hidden by the green ones) are the normalized ion density. At this time the pump signal is not yet backscattered. 78
- 4.4 Spectrum in ω/ω_0 (a) and in k/k_0 (b) of electric field E_z , for a **triangular** density profile. a) The spectrum is integrated over 3.5 ps since the beginning of the simulation. The peak on $\omega/\omega_0 = 1$ corresponds to the nominal frequency of the pump laser. There is no signature of Raman backscattering of the pump at $\omega/\omega_0 \approx 0.77$. b) The spectrum is integrated on the entire simulation box size. The black dashed line at $k/k_0 \approx 0.72$ indicates the wavenumber of the Raman backscattered light in the plasma at a plasma density $n/n_c = 0.05$ 79
- 4.5 Analytical solution of Eq.(1.51) for local values of the intensity of the pump laser and of the plasma density. Fig. 4.5(a): local normalized values of the pump intensity in function of space, at two different times: when the maximum of the pump reaches the left boundary (red line) and when the pump is in the middle of the simulation box (black line).Fig. 4.5(b):values of growth rate $\gamma_{sc}/\omega_0 = \Im(\omega_s)/\omega_0$, versus the positions in the plasma and depending on the different position of the pump (red and black dashed lines correspond to $\gamma_{sc}^{-1} \approx 200$ fs and $\gamma_{sc}^{-1} \approx 178$ fs, respectively). 81

- 4.6 a) The red line is the intensity of the pump normalized to its maximum, the blue line is the light traveling towards left (that includes the seed signal and backscattering of the pump) normalized to the maximum value in intensity of the pump ($I_p = 10^{15}\text{W}/\text{cm}^2$). The green and yellow lines are the electron and ion density distributions normalized to $n/n_c = 0.1$. b) Intensity of the pump signal (red), of the seed signal (blue) and plasma density profile (green) in arbitrary units, in the case in which the maxima of the pulses meet in the middle of the plasma, case **delay 1**. 82
- 4.7 a) Spectra of electric field E_z integrated over the simulation time, for the case in which the two maxima of lasers cross in the middle of the plasma, case **delay 1**. The peak on $\omega/\omega_0 = 1$ corresponds to the nominal frequency of the pump laser. The black dashed line indicates the expected frequency values for Raman, $\omega/\omega_0 \approx 0.68$ (normalized frequency in the vacuum of the Raman backscattered light for $n/n_c = 0.1$). b) Zoom of the spectra of electric field E_z integrated over $\omega/\omega_0 = [0.985, 1.01]$. The downshift in frequency corresponding to the SBS amplification of the seed is $\Delta\omega/\omega_0 \approx 0.002$) 83
- 4.8 Evolution of the spectra in k/k_0 of the electron (a) and ion (b) densities for the case **delay 1**: k_R and k_{IAW} indicate the expected frequency shifts induced by the Raman and Brillouin instability, respectively (red dashed lines). The Raman backscattering starts at $t \approx 5.8$ ps, the SBS amplification after $t \approx 6.1$ ps. 84
- 4.9 a) The red line is the intensity of the pump normalized to its maximum, the blue line amplified seed pulse traveling towards left normalized to the maximum value in intensity of the pump ($I_p = 10^{15}\text{W}/\text{cm}^2$). The green and yellow lines are the electron and ion density distributions normalized to $n/n_c = 0.1$. b) Intensity of the pump signal (red), of the pump signal (blue) and plasma density profile (green) in arbitrary units, in the case in which the maxima of the pulses meet at $x \approx 320\mu\text{m}$, case **delay 2**. 86
- 4.10 Evolution of the spectra in k/k_0 of the electron (a) and ion (b) densities for the case **delay 2**: k_R and k_{IAW} indicate the expected frequency shifts induced by the Raman and Brillouin instability, respectively (red dashed lines). The Raman backscattering starts at $t \approx 5.8$ ps, but it disappears when the Brillouin amplification takes place. 87

4.11 Spectra of electric field E_z integrated over the entire simulation time ($t_{sim} \approx 10$ ps, for a relative delay of $t_{delay} \approx 3.17$ ps, case delay 2). The peak at $\omega/\omega_0 = 1$ corresponds to the nominal frequency of the pump laser. The zoom box shows the frequency downshift due to the SBS amplification of the seed.	88
4.12 The red line is the intensity of the pump normalized to its maximum, the blue line is the amplified seed pulse propagating towards left normalized to the maximum value in intensity of the pump ($I_p = 10^{15}\text{W/cm}^2$), for the case short at $t \approx 6.5$ ps (a) and $t \approx 7.5$ ps (c) (the pump maximum enters the box at $t_0 \approx 5.35$ ps). The green and yellow lines are the electron and ion density distributions normalized to $n/n_c = 0.1$. b) Zoom of the seed intensity for $x = [100,350]$ μm at $t \approx 6.5$ ps.	91
4.13 Amplified backscattered light at the exit of the plasma, for the constant case at $t \approx 6.39$ ps (run I in Table 4.1). The red line is the intensity of the pump normalized to its maximum, the blue line is the amplified light traveling towards left normalized to the maximum value in intensity of the pump ($I_p = 10^{15}\text{W/cm}^2$). The green and yellow lines are the electrons and ions density distribution normalized to $n/n_c = 0.1$	94
4.14 Temporal evolution of the spectra of the electron density: k_{FR} and k_{IAW} indicate the expected frequency for the Forward Raman scattering and SBS backscatter instabilities, respectively (red lines). The Forward Raman scattering starts at $t \approx 6$ ps	95
4.15 Amplified backscattered light at the exit of the plasma, for the triangular case at $t \approx 6.5$ ps (run II in Table 4.1). The red line is the intensity of the pump normalized to its maximum, the blue line is the amplified light traveling towards left normalized to the maximum value in intensity of the pump ($I_p = 10^{15}\text{W/cm}^2$). The yellow lines are the electrons and ions density distribution normalized to $n/n_c = 0.1$	96
5.1 From 2010 L.Lancia's paper [36]. (a) Transmitted signal recorder on the seed spectrometer, at the exit of an Ar plasma with density $n_e = 0.1n_c$. Except for the amplified signal, I_s , all spectra have been multiplied by a factor of 5 for visibility. The focal spot of the seed signal transmitted through the plasma without (b) and with (c) the pump beam. Images are displayed with the same color scale.	99
5.2 Experimental set-up of the experiments presented in [34]	100

5.3	The red surface indicates the intensity of the pump normalized to its maximum ($I_p^{max} = 2 \times 10^{15} W/cm^2$), the blue one is the amplified seed pulse propagating towards left normalized to the maximum value in intensity of the pump.	101
5.4	Evolution of the growth rate (solid curves, left scale) seen by the seed for different delays Δt with the counter propagating pump (dotted red curve, right scale).	103
5.5	a) Transmitted spectra, expressed in mJ=nm, as a function of the delay. Two reference spectra in vacuum propagation are shown. b) 1D-PIC simulated spectra: optimal case (blue solid line) and delayed(green). The peak at the initial pump and seed wavelength(1058 nm) is masked to show only the spectra related to the amplification process.	104
5.6	a) Local normalized values of the pump intensity at two different times: when the maximum of the pump reaches the left boundary of the box (red line) and when the pump is in the middle of the simulation box (black line). The green line indicates the plasma density profile. b)Values of the redshift $\Delta\omega/\omega_0$ as predicted by the sc-SBS linear theory (Chapter 1) versus the positions in the plasma and depending on the different position of the pump (red and black lines correspond to $\Delta\omega/\omega_0 \approx 0.0015$ and $\Delta\omega/\omega_0 \approx 0.0017$, respectively	105
5.7	Energy gain E_{out}/E_{in} of the seed (left scale, blue circles) and pump Raman backscattered signal (right scale, green squares),as a function of relative delay between pump and seed arrival time at the plasma center. Full (empty) circles are the 2D (1D) calorimetry. Plasma density is $0.1n_c$	106
5.8	Duration (FWHM, left axis, triangles) and energy gain (right axis, circles) of the amplified seed laser as a function of relative delay between pump and seed arrival time at the plasma center.	106
5.9	Comparison of the spectra for the simulations with ion fixed in the case with only the pump signal going through the plasma (red line) and the case with both pump and seed lasers interacting (green line).	107
5.10	Spectra in ω/ω_0 of the electric field E_z . a) Simulation with only the pump laser and the ions immobile. b)Simulation with both pump and seed lasers and the ions mobile.	108
5.11	Backscattered pump Raman spectrum for a relative pump-seed delay of $\Delta t = -2 ps$ (a), $\Delta t = -8 ps$ (b), $\Delta t = +4 ps$ (c)	111
6.1	Plasma and lasers configuration for the simulation SIM_A : the pump and seed lasers are crossing in a gaussian plasma with an head-on geometry	120

6.2	Plasma and lasers configuration for the simulation SIM_B : the seed lasers is interacting with two pump signals in a constant plasma shifted towards right. The two pump lasers are propagating in the plasma with an angle $6\tilde{r}$ with respect to the seed direction of propagation	121
6.3	SIM_A : Evolution of the pump and seed intensities at $t = 5.8 ps$ (a), $t = 7.6 ps$ (b) and $t = 9.6 ps$ (c)	125
6.4	Pump and seed intensity at the end of the amplification, at $t = 10 ps$. The final intensity of the seed is $I_{seed}^{out} \approx 3 \times 10^{15}$ ($3 \times$ the initial intensity)	126
6.5	a) Spectrum (in terms of wave number k/k_0 and frequency ω/ω_0 , where k_0 and ω_0 are the nominal wavenumber and frequency of the pump lasers) of the electric field recorded on the entire length of the left side of the simulation box. b) Zoom of the spectrum for $\omega/\omega_0 = [0.98, 1.02]$	127
A.1	Numerical solution of Eq.(A.12)	136
B.1	C++ flow, classes and data structure in SMILEI.	139
B.2	Example of a 32×32 -patches domain decomposition, shared between 7 MPI processes. MPI domains are delimited by different colors. The Hilbert curve (black line) passes through all the patch centers (black dots). It starts from the patch with coordinates (0,0) and end at patch with coordinates (31,0).	144
B.3	Pure MPI strong scaling of SMILEI in an homogeneous plasma case on the OCCIGEN system.	147
B.4	OpenMP load balancing effect. The plot displays the evolution of the wall-clock time necessary to complete 100 iterations as a function of the number of iterations already completed. The legend shows the total number of MPI processes and number of openMP threads per MPI process in the format MPI \times openMP.	148
B.5	Dynamic load balancing (DLB) algorithm effect. The plot displays the evolution of the wall-clock time necessary to complete 100 iterations as a function of the number of iterations already completed. The legend shows the total number of MPI processes and number of openMP threads per MPI process in the format MPI \times openMP. The red and yellow curves are replicas of figure B.4.	149